

Massive star formation in Wolf-Rayet galaxies

V. Star formation rates, masses and the importance of galaxy interactions

Ángel R. López-Sánchez^{1,2}

¹ CSIRO Astronomy and Space Science / Australia Telescope National Facility, PO-BOX 76, Epping, NSW 1710, Australia

² Instituto de Astrofísica de Canarias, C/ Vía Láctea S/N, E-38200, La Laguna, Tenerife, Spain

Received Feb 20, 2010; Accepted May 3, 2010

ABSTRACT

Aims. We have performed a comprehensive analysis of a sample of 20 starburst galaxies that show the presence of a substantial population of very young massive stars, most of them classified as Wolf-Rayet galaxies.

Methods. In this paper, the last of the series, we analyze the global properties of our galaxy sample using multiwavelength data extracted from our own observations ($H\alpha$ fluxes, B and H -band magnitudes) and from the literature, that include X-ray, FUV , FIR , and radio (both $H\text{I}$ spectral line and 1.4 GHz radio-continuum) measurements.

Results. The agreement between our $H\alpha$ -based star-formation rates (SFR) and those provided by indicators at other wavelengths is remarkable, but we consider that the new $H\alpha$ -based calibration provided by Calzetti et al. (2007) should be preferred over older calibrations. The FUV -based SFR provides a powerful tool to analyze the star-formation activity in both global and local scales independently to the $H\alpha$ emission. We provide empirical relationships between the ionized gas mass, neutral gas mass, dust mass, stellar mass, and dynamical mass with the B -luminosity. Although all mass estimations increase with increasing luminosity, we find important deviations to the general trend in some objects, that seem to be consequence of their particular evolutionary histories. The analysis of the mass-to-light ratios give similar results. We investigate the mass-metallicity relations and conclude that both the nature and the star-formation history are needed to understand the relationships between both properties. The majority of the galaxies follow a Schmidt-Kennicutt scaling law of star-formation that agrees with that reported in individual star-forming regions within M 51 but not with that found in normal spiral galaxies. Dwarf galaxies seem to be forming stars more efficiently than the outskirts of spiral galaxies. We found a relation between the reddening coefficient and the warm dust mass indicating that the extinction is mainly internal to the galaxies. The comparison with the closed-box model also indicates that environment effects play an important role in their evolution.

Conclusions. Considering all multi-wavelength data, we found that 17 up to 20 galaxies are clearly interacting or merging with low-luminosity dwarf objects or $H\text{I}$ clouds. The remaining three galaxies (Mkn 5, SBS 1054+364, and SBS 1415+437) show considerable divergences of some properties when comparing with similar objects. Many of the interacting/merging features are only detected when deep optical spectroscopy and a detailed multi-wavelength analysis, including $H\text{I}$ observations, are obtained. We conclude that interactions do play a fundamental role in the triggering mechanism of the strong star-formation activity observed in dwarf starburst galaxies.

Key words. galaxies: starburst — galaxies: interactions — galaxies: dwarf — galaxies: abundances — galaxies: kinematics and dynamics — stars: Wolf-Rayet

1. Introduction

1.1. Galaxy interactions and starburst activity

Since the discovery of the starburst galaxies (Sargent & Searle 1970), many studies have tried to understand the processes that trigger the strong star-formation activity in these objects. The hypothesis that gravitational interaction (not necessary merging) of galaxies enhances star formation or leads to starburst activity was made soon after the recognition of the starburst phenomenon. Larson & Tinsley (1978) did a study of normal and peculiar (Arp 1966) sample of galaxies and demonstrated that recent ($\leq 10^8$ yr) star-formation is more likely to occur in interacting than in non-interacting galaxies. Since then, numerous studies of individual galax-

ies have revealed the fossil remnants of interaction/merger activity, increasing the evidences that interactions and mergers trigger star-formation phenomena in spiral galaxies (Koribalski 1996; Kennicutt 1998; Nikolic et al. 2004). Infrared observations confirmed the existence of very intense starbursts in major disk-disk mergers (e.g., Joseph & Wright 1985; Solomon & Sage 1988; Sanders & Mirabel 1996; Genzel et al. 1998; Arribas et al. 2004). Actually, almost 100% of galaxies with far-infrared (FIR) luminosities of about $10^{12} L_{\odot}$ are in interacting/merging systems (Sanders 1997). Furthermore, analysis of large galaxy surveys (e.g., CfA2: Barton, Geller & Kenyon 2000; 2dF: Lambas et al. 2003; SDSS: Nikolic et al. 2004) has provided new evidences for interaction-induced starburst activity.

According to hierarchical clustering models of galaxy formation, larger galactic structures build up and grow through the accretion of dwarf galaxies (White & Frenk,

Send offprint requests to: Ángel R. López-Sánchez, e-mail: Angel.Lopez-Sanchez@csiro.au

1991; Kauffman & White 1993; Springer et al. 2005). Observations of local and distant luminous blue galaxies (LBG) and Lyman break galaxies seem to confirm that galaxy interactions are more common at high redshifts. (e.g., Guzman et al. 1997; Hopkins et al. 2002; Erb et al. 2003; Werk, Jangren & Salzer 2004; Colina, Arribas & Monreal-Ibero 2005; Overzier et al. 2009; Cardamone et al. 2009) but many details are still unclear (i.e., Basu-Zych et al. 2009). Indeed, detailed studies of local interacting/merging galaxies provide vital clues to our knowledge in galaxy formation and evolution, as they constrain the properties of the hierarchical formation models.

Recent observations also suggest that interactions and mergers between dwarf galaxies also trigger the star-formation activity and play a fundamental role in the evolution of dwarf galaxies (i.e., Méndez & Esteban, 2000; Östlin et al. 2001, 2004; Bergvall & Östlin 2002; Johnson et al. 2004; Bravo-Alfaro et al. 2004, 2006; Cumming et al. 2008, García-Lorenzo et al. 2008; López-Sánchez & Esteban, 2008, 2009; James et al. 2010). Many of these studies have been done in Blue Compact Dwarf Galaxies (BCDGs), that are low-luminosity, low-metallicity ($\sim 10\%$ solar) galaxies showing compact and irregular morphologies and undergoing an intense and short-lived episode of star formation (i.e., Izotov & Thuan 1999; Cairós et al. 2001a,b; Papaderos et al. 2006), on top of an old underlying population with ages of several Gyrs (Noeske et al. 2003, 2005; Amorín et al. 2007, 2009). Recent numerical simulations (Bekki 2008) satisfactorily explain the physical properties of BCDGs as a consequence of the merging of two dwarf galaxies with larger fraction of gas and extended gas disks.

Actually, much of our knowledge in interacting galaxies has been provided via H I observations. Neutral hydrogen gas is the best tracer for galaxy-galaxy interactions because, such the H I distribution is usually several times larger than the optical extent, it is more easily disrupted by external forces (tidal interactions, gas infall, ram pressure stripping) than the stellar disk (Broeils & van Woerden 1994; Salpeter & Hoffman 1996). The distribution and kinematics of atomic gas within galaxies usually is more or less regular, but in many cases they revealed complex entities between galaxies such as tails, ripples and bridges, arcs, or independent H I clumps that, in many cases, show little disturbance in their corresponding optical images (e.g., Schneider et al. 1989; Yun, Ho & Lo 1994; Hibbard & van Gorkom 1996; Verdes-Montenegro et al. 2001, 2002, 2005; Putman et al. 2003; Koribalski et al. 2003; 2004; 2005; Tempurin et al. 2003, 2005; Emonts et al. 2006; Ekta et al. 2008; Koribalski & López-Sánchez 2009; English et al. 2010; see also *The H I Rogues Gallery*, Hibbard et al. 2001). Several interferometric H I surveys, such as *The H I Nearby Galaxy Survey* (THINGS, Walter et al. 2008), the *Local Volume H I Survey* (LVHIS, Koribalski 2008) or the *Faint Irregular Galaxies GMRT Survey* (FIGGS, Begum et al. 2008), are nowadays providing accurate H I and dynamical masses in hundreds of nearby galaxies, many of them being dwarf objects, as they account for $\sim 85\%$ of the known galaxies in the Local Volume (Karachentsev et al. 2004).

1.2. The interplay between gas and stars in galaxies

However, to understand interaction processes in dwarf galaxies we first have to know how stars and gas inter-

act in low-mass environments. Indeed, feedback from massive stars is the dominant process that affects the interstellar medium (ISM) of these galaxies. Violent star-formation phenomena may disrupt the galaxy's gas and even expel it to the intergalactic medium, as some theoretical models predict (Mac Low & Ferrara 1999). But alternative models (e.g., Silich & Tenorio-Tagle 1998) and the available observations (Bomans 2005) suggest that dwarf galaxies keep their processed material. Furthermore, the links between the observational characteristics (fluxes, colors, morphologies or sizes) and the underlying physical properties of the galaxies (stellar, dust, gas, baryonic, and dark matter content, chemical abundances, star formation rate, star formation history) are still not well known.

For example, there are still many caveats in the understanding of the interplay between the star formation rate (SFR) and the properties of the ISM. A very important step was achieved with the Schmidt-Kennicutt power-law relation (Schmidt 1959, 1963; Kennicutt 1998) that correlates the average SFR per unit area and the mean surface density of the cold gas (atomic plus molecular). But tracers of star-formation, including optical colors and H α flux (e.g., Larson & Tinsley, 1978; Kennicutt 1998; Calzetti et al. 2007), *FIR* flux (Kennicutt 1998; Heckman 1999), radio-continuum flux (Condon 1992), and far-ultraviolet (*FUV*) flux (Kennicutt 1998; Salim et al. 2007), often yield to very different values of the SFR. Although the density of atomic gas is known in some cases, no many direct measurements of the molecular gas are available, being specially rare in dwarf galaxies (i.e., Taylor et al. 1998; Barone et al. 2000; Braine et al. 2000, 2001, 2004).

On the other hand, the physics underlying the relationship between stellar mass (or luminosity) with the metallicity is still far from clear, besides the important observational (e.g., Tremonti et al. 2004; van Zee & Haynes, 2006; Kewley & Ellison 2008) and theoretical (e.g., De Lucia et al. 2004; Tissera et al. 2005; De Rossi et al. 2006; Davé & Oppenheimer 2007) efforts that aimed to explain it. Indeed, one of the main problems is to derive the real metallicity of the ionized gas, as empirical calibrations based on the direct estimation of the electron temperature (T_e) of the ionized gas and theoretical methods based on photoionization models provide very different oxygen abundances (e.g., Yin et al. 2007; Kewley & Ellison 2008; Esteban et al. 2009; López-Sánchez & Esteban, 2010). Finally, the present understanding of correlations between the H I content, stellar populations and star formation in dwarf starburst galaxies is still at a preliminary stage because of the lack of detailed optical/*NIR* images and spectra and/or interferometric H I maps in these systems.

1.3. About this paper series

In our paper series, we have presented a detailed photometric and spectroscopic study of a sample of strong star-forming galaxies, many of them previously classified as dwarf galaxies. The majority of these objects are Wolf-Rayet (WR) galaxies, that are a very inhomogeneous class of star-forming objects which have in common that the ongoing or most recent star formation event has produced stars sufficiently massive to evolve to the WR stage (Schaerer, Contini & Pindao 1999). The presence of WR features in the spectra of a galaxy constrains the properties of the star-formation processes. As the first WR stars typ-

ically appear around 2 – 3 Myr after the starburst is initiated and disappear within some 5 Myr (Meynet & Maeder 2005), their detection informs about both the youth and strength of the burst, offering the opportunity to study an approximately coeval sample of very young starbursts (Schaerer & Vacca 1998).

Our main aim is the study of the formation of massive stars in starburst galaxies and the role that interaction with or between dwarf galaxies and/or low surface brightness objects have in its triggering mechanism. In Paper I (López-Sánchez & Esteban 2008) we exposed the motivation of this work, compiled the list of the analyzed WR galaxies (Table 1 of Paper I) and presented the results of optical/*NIR* broad-band and H α photometry. In Paper II (López-Sánchez & Esteban 2009) we presented the results of the analysis of intermediate-resolution long slit spectroscopy of 16 objects of our sample of WR galaxies –the results for the other 4 objects have been published separately. In Paper II, we also specified the oxygen abundances of the ionized gas (they were computed following the direct T_e method in the majority of the cases) and analyzed the kinematics of the ionized gas. In Paper III (López-Sánchez & Esteban 2010a), we studied the O and WR stellar populations within these galaxies, and compared with theoretical evolutionary synthesis models. In Paper IV (López-Sánchez & Esteban 2010b), we analyzed globally the optical/*NIR* properties of the galaxies, concluding that such detailed analyses are fundamental to understand the star-formation histories of the galaxies. In this paper, the last of the series, we perform a comprehensive multiwavelength analysis considering all the optical and *NIR* data but also including radio, *FIR*, *FUV* and X-ray data available in the literature.

The selection criteria of the galaxy sample were the following. We used the most recent catalogue of Wolf-Rayet galaxies (Schaerer et al. 1999), which contains a very inhomogeneous group of starbursting objects, to make a list of dwarf objects that could be observed from the Northern Hemisphere. Hence, we did not consider either spirals galaxies or giant H II regions within them, and considered only dwarf objects, such as apparently isolated BCDGs and dwarf irregular galaxies that had peculiar morphologies in previous, shallower imaging. We also chose two galaxies belonging to the Schaerer et al. (1999) catalogue that were classified as *suspected* WR galaxies (Mkn 1087 and Tol 9), to confirm the presence of massive stars within them (see Papers II and III). The galaxy IRAS 08339+6517 was also included because previous multiwavelength results suggested that the WR stars could still be present in its youngest star-forming bursts (see López-Sánchez et al. 2006). With this, we got a list of ~ 40 systems to observe and analyze using the telescopes available at Roque de los Muchachos (La Palma, Spain) and Calar Alto (Almería, Spain) observatories. We added the southern galaxy NGC 5253, for which we obtained deep echelle spectrophotometry using 8.2m VLT, because of the very intriguing properties it possesses (see López-Sánchez et al. 2007, 2010). The final sample of 20 galaxies was created considering those galaxies for which we obtained optical/*NIR* broad-band and H α images plus the deep optical spectroscopy during our observation runs. We already have all these data for other ~ 15 galaxies, the analysis of these systems will be presented in the future elsewhere, but its preliminary results seem to agree with the main results re-

ported in this paper. Hence, our galaxy sample is not complete, but we consider it represents quite well dwarf galaxies experiencing a very strong star-formation burst. Indeed, this was the main bias introduced when choosing the galaxy sample, such as we focused only in galaxies in which WR stars are detected. It would be very interesting to extend this analysis to similar star-forming galaxies that do not show WR features, as the sample of BCDGs analyzed by Gil de Paz, Madore & Pevunova (2003).

The structure of this paper is the following. In Sect. 2 we describe the details of the radio, *FIR*, *FUV*, and X-ray data extracted from the literature, providing some very useful relations. Sect. 3 analyzes the star-formation activity in our sample galaxies considering all multi-wavelength calibrators to the SFR. We check if our sample galaxies follow the radio/*FIR* correlation in Sect. 4. Next, Sect. 5 compiles, analyses and compares all mass estimations derived in this work. Several mass-metallicity relations are investigated in Sect. 6. We study whether our galaxies satisfy the Schmidt-Kennicutt relation in Sect. 7. Section 8 analyzes and compares several mass-to-light ratios. The dust properties within our starburst galaxies are investigated in Sect. 9. We compare the predictions of the closed-box model with our observational data in Sect. 10. Finally, Sect 11 compiles a quantitative analysis of the interaction features considering all available multi-wavelength data. The conclusions reached in our analysis are compiled in Sect. 12. The Appendix describes the main results found in each of the analyzed WR galaxies.

Hence, this is essentially an observational work. Each system has been carefully analyzed considering all available data (those specifically obtained for this work and those compiled from literature) with the final aim to understand its chemical and dynamical evolution, its stellar, dust, gas, and dark matter content, the relative importance of its stellar populations (WR, young, intermediate-age and old stars) and its star formation properties. Our data support the hypothesis that interactions between galaxies and dwarf or low surface-brightness objects (that can not be detected using less detailed and less deeper observations) have a considerable importance in the triggering mechanism of massive star formation activity in this kind and young starbursts. We have produced the most complete, detailed, and exhaustive data set of this kind of galaxies, so far, involving multi-wavelength data and a careful analysis of each individual object following the same procedures and equations.

2. Multi-wavelength data completeness

We have performed an exhaustive literature search to complete the optical/*NIR* observations of our WR galaxy sample with data from other wavelengths (radio, far-infrared, far-ultraviolet, and X-ray). Here we describe all these data and the useful properties we derive from them.

2.1. Radio data

2.1.1. HI data at 21 cm

Observations in the hyperfine transition of the neutral hydrogen, H I, with a rest frequency of 1420.405 MHz, have been key to understand the distribution and kinematics of the atomic gas within galaxies, included the Milky Way. Neutral gas observations are very important because they

Table 1. Radio data compiled from the literature for our WR galaxy sample. We include the flux of the 21 cm H I emission line, F_{HI} , its equivalent width, W_{HI} , and the radio-continuum flux at 1.4 GHz, $S_{1.4\text{GHz}}$.

Galaxy	F_{HI} [Jy km s ⁻¹]	W_{HI} [km s ⁻¹]	Ref.	$S_{1.4\text{GHz}}$ [mJy]	Ref.
HCG 31 AC	5.15	169.2A+190.6C	VM05	22±3	VM05
HCG 31 B	2.74	85.8	VM05	2.1±0.3	VM05
HCG 31 F	0.866	74.6	VM05
HCG 31 G	2.74	84.9	VM05	3.3±0.5	VM05
Mkn 1087	5.38	270	GG81	12.1±0.6	Co98
Haro 15	3.11±1.01	220	GG81	17.8±1.0	Co98
Mkn 1199	1.78±0.67	170	DC04	36.2±1.2	Co98
Mkn 5	2.12±0.27	22.4±4.9	Pa03	<2.8	HSLD02
IRAS 08208+2816	15.2±0.6	Co98
IRAS 08339+6517	3.68±0.46	~300	Ca04	33.56 ^a	Co90
POX 4 ^b	4.31	130	LS10b	4.2±0.5	Co98
UM 420	1.1±0.3	HSLD02
SBS 0926+606A ^c	1.30±0.49	120±37	P02	2.7±0.6	HSLD02
SBS 0926+606B ^c	1.10±0.49	120±37	P02
SBS 0948+532	<0.9	HSLD02
SBS 1054+365	4.03±0.39	117±11	Z00	1.28±0.14	BWH95
SBS 1211+540	0.71±0.12	47	H05	<0.9	HSLD02
SBS 1319+579	8.4	134	H07	<2.9	HSLD02
SBS 1415+437	4.73±0.32	66	H05	<0.5	H05
III Zw 107	4.48±0.79	200±25	P03	8.0±0.5	Co98+Y01
Tol 9 ^b	5.02±0.40	185	LS10b	19.2±0.7	Co98
Tol 1457-262 ^d	4.3	176	Kor06	38.9±1.8	Co98+Y01
Arp 252 ^{d,e}	Kor06	97.6±3.0	Co98+Y01
NGC 5253 ^b	43.1±2.6	106±6	LS10a	87.1±3.5	LS10a

^a Co90 (Condon et al. 1990) gave radio-continuum values at 1.49 GHz. The value of $S_{1.4\text{GHz}}$ shown in the table was computed from $S_{1.49\text{GHz}}$ using the (Condon, Cotton & Broderick 2002) relation between both quantities, as it was explained in López-Sánchez, Esteban & García-Rojas (2006).

^b A detailed analysis of the H I gas within the galaxies POX 4, Tol 9 and NGC 5253 using the *Australia Telescope Compact Array* (ATCA) will be soon presented elsewhere (López-Sánchez et al. 2010a,b).

^c SBS 0926+606 was observed by Huchtmeier et al. (2007), who gave a measurement of the H I flux for both A and B galaxies. Only interferometric studies can disentangle the amount of neutral gas in the individual galaxies.

^d This galaxy was observed in H I by Casasola, Bettoni & Galletta (2004) using a single-dish antenna, but it was not detected.

^e This galaxy is not detected in H I in HIPASS (Koribalski 2006, priv. comm.).

REFERENCES: Ca04: Cannon et al. (2004); CBG04: Casasola, Bettoni & Galletta (2004); Co90: Condon et al. (1990); Co98: Condon et al. (1998); DC04: Davoust & Contini (2004); GG81: Gordon & Gottesman (1981); HSLD02: Hopkins, Schulte-Ladbeck & Drozdovsky (2002); H05: Huchtmeier, Krishna & Petrosian (2005); H07: Huchtmeier et al. (2007); Kor06: Koribalski (2006), priv. comm.; LS10a: López-Sánchez et al. (2010a); LS10b: López-Sánchez et al. (2010b); Pa03: Patrel et al. (2003); HyperLEDA; P02: Pustilnik et al. (2002); VM05: Verdes-Montenegro et al. (2005); Y01: Yun, Reddy & Condon (2001); Z00: Zasov et al. (2000).

are used to determine both the neutral gas mass (H I gas) and the dynamical mass (M_{dyn}) of the systems. Single-dish H I surveys, –e.g. Mathewson et al. 1992, the H I *Parkes Sky Survey* (HIPASS, Barnes et al. 2001; Koribalski et al. 2004; Meyer et al. 2004), and the *Arecibo Legacy Fast ALFA* survey (ALFALFA; Giovanelli et al. 2005)–, give spectra with detected H I emission of thousands of galaxies. However, the best tool to analyze the neutral gas content in galaxies is via radio interferometer observations (e.g., THINGS; LVHIS; FIGGS; *The H I Rogues Gallery*). Knowing the amount of available neutral gas, the timescale of the starbursts (i.e., the time in which the H I cloud will be exhausted if the star formation activity continue at the current SFR) can be calculated.

Table 1 compiles all H I 21 cm data found for our galaxy sample. The majority of the H I data is provided by single-dish H I observations, but for some few cases (HGC 31 and IRAS 08339+6517) interferometric H I maps are available. Table 1 lists the H I flux density, f_{HI} (in units of Jy km s⁻¹), and the H I equivalent width, W_{HI} (in km s⁻¹). We note that for 3 galaxies (POX 4, Tol 9 and NGC 5253) we are using the data provided by our new interferometric maps obtained using the *Australia Telescope Compact*

Array. For these objects, we compile the integrated H I flux and width; their detailed analysis will be soon presented elsewhere (López-Sánchez et al. 2010a,b). The total H I mass is computed applying

$$M_{\text{HI}} = 2.356 \times 10^5 d^2 f_{\text{HI}} \quad (1)$$

(Roberts 1975; Roberts & Haynes 1994) where the distance to the galaxy, d , is expressed in Mpc and the result for the neutral gas mass is given in solar units. The dynamical mass of the system, M_{dyn} , can be estimated from H I radio observations considering the inclination-corrected maximum rotation velocity, v_{max}^i , that is obtained at radius R_{max} and assuming a virial equilibrium,

$$M_{\text{dyn}} = 2.31 \times 10^5 R_{\text{max}} (v_{\text{max}}^i)^2, \quad (2)$$

being the result in solar masses and assuming $v_{\text{max}}^i = \frac{W_{\text{HI}}}{2 \sin i}$. The inclination angle, i , is defined as that found between the plane of the sky and the plane of the galaxy (hence, $i=90^\circ$ in an edge-on galaxy and $i=0^\circ$ in a face-on galaxy). We usually estimated this angle assuming that the elliptical shape of the galaxy is just a consequence of its orientation. Note that the usual problem deriving virial masses is the unknowledge of the inclination angle, i , and sometimes also

Table 2. *FIR* and *FUV* data for the WR galaxy sample analyzed in this work. *FIR* data were provided by IRAS, *FUV* data were provided by GALEX. The value of the total *FIR* flux was computed using Equation 7.

Galaxy	$f_{12\ \mu\text{m}}$ [Jy]	$f_{25\ \mu\text{m}}$ [Jy]	$f_{60\ \mu\text{m}}$ [Jy]	$f_{100\ \mu\text{m}}$ [Jy]	F_{FIR} (a)	Reg. (b)	m_{FUV} [mag]	f_{FUV} (c)
HCG 31	0.110±0.020	0.580±0.040	3.92±0.31	5.84±0.47	2.01±0.16	AC	14.97±0.06	7.54±0.44
						B	16.80±0.09	3.32±0.26
						E	18.01±0.08	0.456±0.035
						F	18.24±0.11	0.460±0.047
						G	15.93±0.06	3.11±0.18
						H	20.63±0.40	0.0041±0.0014
Mkn 1087	0.103±0.029	0.414±0.058	3.03±0.33	4.44±0.40	1.54±0.16
Haro 15	0.118±0.034	0.297±0.089	1.36±0.12	1.97±0.20	0.690±0.064	...	15.12±0.07	9.41±0.57
Mkn 1199	0.282±0.031	1.28±0.09	6.82±0.34	8.85±0.53	3.33±0.18
Mkn 5	<0.0503	<0.0533	0.21±0.04	<0.8473	<1.75	...	17.76±0.07	1.59±0.10
IRAS 08208+2816	0.126±0.029	0.278±0.067	1.15±0.09	1.70±0.17	0.588±0.051	...	16.59±0.07	3.75±0.23
IRAS 08339+6517	0.250±0.025	1.13±0.02	5.81±0.04	6.48±0.09	2.71±0.02	...	15.37±0.06	10.7±0.6
						c	19.70±0.10	0.160±0.014
POX 4	<0.987	0.153±0.040	0.629±0.057	<0.5798	<0.278	POX 4	16.03±0.06	2.82±0.16
						Comp.	19.06±0.12	0.269±0.030
UM 420	...	<0.275	0.411:	0.613:	0.211:	...	18.22±0.06	0.377±0.021
SBS 0926+606	<0.07553	<0.08818	0.269±0.046	<0.5296	<0.154	A	16.71±0.06	1.75±0.09
						B	17.84±0.10	0.829±0.073
SBS 0948+532
SBS 1054+365	<0.055	<0.100	0.536±0.048	0.97±0.15	0.296±0.035	...	16.67±0.07	1.18±0.08
SBS 1211+540	18.40±0.07	0.370±0.022
SBS 1319+579	0.209:	0.685:	0.154:	...	17.00±0.06	0.864±0.048
						A	18.60±0.06	0.199±0.010
SBS 1415+437	16.22±0.06	3.95±0.22
III Zw 107	<0.0968	0.336±0.050	1.37±0.20	1.72±0.31	0.662±0.104
Tol 9	0.111±0.030	0.465±0.051	2.71±0.22	<5.516	<1.58	...	17.57±0.07	4.22±0.22
Tol 1457-262	<0.117	0.611±0.067	3.09±0.19	3.68±0.40	1.47±0.11	...	15.84±0.07	6.95±0.47
						Obj 1	16.15±0.06	5.26±0.29
						Obj 2	17.41±0.13	1.64±0.18
						#15	19.71±0.21	0.199±0.037
Arp 252	0.188±0.023	0.994±0.050	3.91±0.20	4.11±0.25	1.79±0.10	A	18.67±0.08	1.91±0.13
						B	18.84±0.07	0.441±0.027
NGC 5253	2.50±0.02	12.07±0.05	29.84±0.07	30.08±0.21	13.49±0.05	...	12.81±0.06	123.0±6.5

(a) In units of 10^{-10} erg s $^{-1}$ cm $^{-2}$.

(b) Region within each system (HCG 31, IRAS 08339+6517, POX 4, SBS 0926+606, SBS 1319+579, Tol 1457-262, and Arp 252; see Paper I for identification of the regions). The *FIR* emission provided by IRAS does not allow to distinguish between these regions, but *FUV* data provided by GALEX does. In Arp 252, region A is galaxy ESO 566-8 and region B is galaxy ESO 566-7.

(c) In units of 10^{-14} erg s $^{-1}$ cm $^{-2}$ Å $^{-1}$.

R_{max} , specially in galaxies showing disturbed morphologies. We adopted the maximum radius observed in our deep optical images. Therefore, as the extension of the neutral gas is usually larger than the extension of the stellar component, our values of M_{dyn} may be underestimated. The gas depletion timescale defined by Skillman et al. (2003) was computed using M_{HI} and the assumed SFR derived for each galaxy (see below).

2.1.2. Radio-continuum data

For an individual star-forming galaxy, the SFR is directly proportional to its radio luminosity (i.e., Condon 1992). Hence, the radio continuum flux is widely used as a dust-free indicator of the star formation rate. Nearly all of the radio-continuum luminosity from galaxies without a significant Active Galactic Nucleus (AGN) can be traced to recently formed massive ($M \geq 8 M_{\odot}$) stars (Condon et al. 1992). The 10% of the continuum emission at 1.4 GHz is due to free-free emission from extremely massive main-sequence stars (thermal emission) and almost 90% is synchrotron radiation from relativistic electrons accelerated in the remnants of core-collapse supernovae (non-thermal

emission). As the stars that contribute significantly to the radio emission have lifetimes $\tau \leq 3 \times 10^7$ yr and the relativistic electrons have lifetimes $\tau \leq 10^8$ yr, the current radio luminosity is nearly proportional to the rate of massive star formation during the past $\tau \leq 10^8$ yr (Condon, Cotton & Broderick 2002):

$$SFR_{1.4\ \text{GHz}} (M > 5M_{\odot}) \sim 2.5 \times 10^{-22} L_{1.4\ \text{GHz}}, \quad (3)$$

where $L_{1.4\ \text{GHz}}$ has units of W Hz $^{-1}$.

Table 1 compiles all 1.4 GHz radio-continuum flux data available for our WR galaxy sample in the literature. The 1.4 GHz luminosity, $S_{1.4\ \text{GHz}}$, can be computed using the expression given by Yun, Reddy & Condon (2001):

$$\log L_{1.4\ \text{GHz}} = 20.07 + 2 \log d + \log S_{1.4\ \text{GHz}}, \quad (4)$$

where the result is given in units of W Hz $^{-1}$, the distance d is expressed in Mpc and $S_{1.4\ \text{GHz}}$ is expressed in Jy.

Radio-continuum observations at several cm wavelengths are used to quantify the thermal and non-thermal contributions, and thereby distinguish older and supernova-rich regions from younger and mostly thermal areas (i.e., Deeg et al. 1993, Beck et al. 2000, Cannon et

al. 2004, 2005). These observations also permit to detect extremely young, dense heavily embedded star clusters (Kobulnicky & Johnson 1999; Johnson & Kobulnicky 2003). Although radio data at frequencies different of 1.4 GHz are not usually available for this kind of galaxies, we applied the equation provided by Dopita et al. (2002),

$$F_{1.4\text{ GHz thermal}} = 1.21 \times 10^{12} F_{H\alpha}, \quad (5)$$

to obtain an estimation of the thermal emission at 1.4 GHz, $F_{1.4\text{ GHz thermal}}$, using the $H\alpha$ flux derived from our images (see Paper I). In this equation, $F_{H\alpha}$ is in units of $\text{erg cm}^{-2} \text{s}^{-1}$ and the result is given in mJy. The comparison between $F_{1.4\text{ GHz thermal}}$ and $F_{1.4\text{ GHz}}$ allows the estimation of the non-thermal flux. Condon (1992) and Niklas, Klein & Wielebinski (1997) indicated that the non-thermal component is more than 90% of the total at this frequency. It is common to consider the non-thermal to thermal ratio, R ; Dopita et al. (2002) reported that the average value in starburst galaxies is $\log R = 1.3 \pm 0.4$. Radio continuum and *FIR* data help to discern between the normal or active (that is, a galaxy hosting an AGN) nature.

2.2. FIR data

Many of the problems found to derive the SFR from optical data can be avoided by measuring the far-infrared (FIR) and sub-millimeter spectral energy distributions (SEDs). These are determined by the re-radiation as thermal continuum by the dust grains of stellar photospheric radiation absorbed in the visible and UV regions of the spectrum. Assuming that the dust completely surrounds the star forming regions, it acts as a bolometer reprocessing the luminosity produced by the stars. Therefore, the SFR can be also computed using theoretical stellar flux distributions and evolutionary models. Kennicutt (1998) provides the following correlation between the SFR (in units of $M_{\odot} \text{yr}^{-1}$) and the far-infrared flux:

$$SFR_{FIR} = 4.5 \times 10^{-44} L_{FIR}, \quad (6)$$

where L_{FIR} (given in units of erg s^{-1}) is obtained using the *FIR* flux between 42.5 and 122.5 μm (Sanders & Mirabel 1996),

$$F_{FIR} = 1.26 \times 10^{-11} (2.58 f_{60} + f_{100}), \quad (7)$$

being f_{60} and f_{100} the flux densities (in Jy) for 60 μm and 100 μm and the conventional expression between flux and luminosity, $L = 4\pi d^2 F$. This relation can be applied only in starbursts with ages less than 10^8 yr, where the approximations assumed by Kennicutt (1998) are valid. If the SFR value derived from L_{FIR} agrees with that estimated from the $H\alpha$ luminosity we may consider that the correction by extinction done to derive the $H\alpha$ flux is correct.

Assuming that all the UV and blue radiation from massive stars is absorbed by grains and is re-emitted as thermal radiation in the 40-120 μm band, Condon (1992) derives the following relation between SFR and $L_{60\mu\text{m}}$ (in units of W Hz^{-1}):

$$SFR_{60\mu\text{m}} \sim 1.96 \times 10^{-24} L_{60\mu\text{m}}, \quad (8)$$

i.e.,

$$SFR_{60\mu\text{m}} \sim 2.346 \times 10^{-4} f_{60\mu\text{m}} d^2, \quad (9)$$

being $f_{60\mu\text{m}}$ expressed in Jy and d in Mpc. Although some authors (Lonsdale et al. 1984) have argued that radiation from stars less massive than $5 M_{\odot}$ will contribute significantly to FIR emission from galactic disks, this relation seems to give good values for the SFR.

Roussel et al. (2001) provide an alternative SFR calibration using the 15 μm luminosity:

$$SFR_{15\mu\text{m}} \sim 3.66 \times 10^{-3} d^2 f_{15\mu\text{m}}, \quad (10)$$

being $f_{15\mu\text{m}}$ the monochromatic flux at 15 μm and d the distance in Mpc. This formula is applicable only when the mid-infrared emission is dominated by unidentified infrared bands (UIBs) with a negligible very small grains (VSG) continuum, which is the case in disk galaxies, but is not always verified at 15 μm in galactic central regions. It may be assumed that $L_{15\mu\text{m}} \sim L_{12\mu\text{m}}$.

The warm dust mass can be estimated using the 60 and 100 μm fluxes and applying the relation given by Huchtmeier, Sage & Henkel (1995),

$$M_{dust} = 4.78 d^2 f_{100\mu\text{m}} \left(\exp \left[2.94 \left(\frac{f_{100\mu\text{m}}}{f_{60\mu\text{m}}} \right)^{0.4} \right] - 1 \right), \quad (11)$$

where the distance is expressed in Mpc, the flux densities are in Jy and the result is given in M_{\odot} .

We have used the far-infrared (*FIR*) data provided by the *Infrared Astronomical Satellite* (IRAS) to obtain the monochromatic fluxes at 12, 25, 60 and 100 μm . These data are used to get an independent estimation of the SFR and to derive the warm dust mass within every galaxy. We will also check if the galaxies follow the *FIR*-radio relationship. Table 2 compiles all the *FIR* data found for our sample of WR galaxies, three of them have no useful measurements at these frequencies.

2.3. FUV data

In the last years, the *GALaxy Evolution eXplorer* (GALEX) satellite is providing astonishing ultraviolet (*UV*) images of galaxies, and revealing recent star-formation activity in their external regions (i.e., Gil de Paz, 2005, 2007; Thilker et al. 2005; Koribalski & López-Sánchez, 2009). The GALEX point spread function in the central 0.5° has a full width at half-maximum (*FWHM*) of ~ 5 arcsec, matching quite nicely with the spatial resolution of our optical/*NIR* images. We searched for GALEX observations of the galaxies that compose our sample in the *far-UV* band (*FUV*, 1350–1750 Å), all of them except four objects (Mkn 1087, Mkn 1199, SBS 0948+532 and III Zw 107) have useful *FUV* data.

In general, the *FUV* emission of our sample galaxies matches quite well with their optical emission. In many cases, *FUV* emission is much more extended than the $H\alpha$ emission. Figure 1 shows as examples the GALEX *FUV* images of HCG 31, Haro 15, and SBS 0926+606. As we can see when comparing with our optical images (see Paper I), the star-forming regions are clearly observed in *FUV*. Just quick comments about three galaxies:

- we note that the eastern tail of SBS 0926+606 B is quite bright in the *FUV* image, suggesting an extended distribution of massive OB stars that we do not detect in our deep $H\alpha$ image (see Fig. 15 and Sec. 3.10.1 in Paper I),

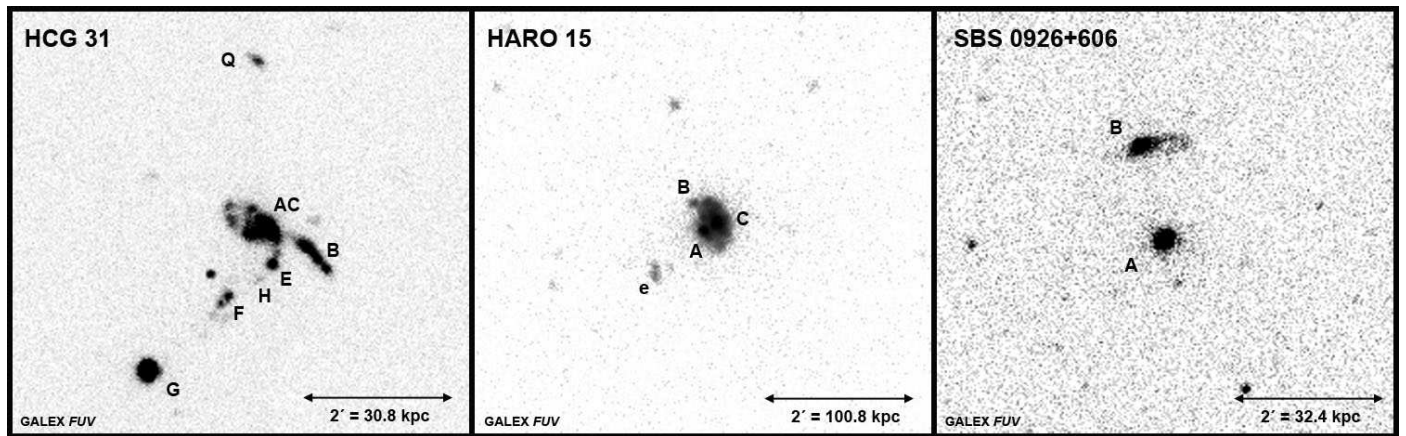


Fig. 1. Example of GALEX images, showing the FUV emission in HCG 31, Haro 15 and SBS 0926+606. Regions within each object have been labeled following the notation given in Paper I.

- the star-forming galaxy #15 in Tol 1457-262 is clearly detected in the FUV emission, but the faint galaxy #16 is not seen (Fig 31 and Sect. 3.18.1 in Paper I), and
- in Arp 252, FUV emission is not only detected at the center of the galaxies (ESO 566-8 and ESO 566-7) but also throughout the tails and in tidal dwarf candidates c , e and d (see Fig. 34 and Sect. 3.19.1 in Paper I).

FUV data can be used to get an independent estimation of the SFR of the galaxies. UV -emission probes star formation over time-scales of ~ 100 Myr, the lifetime of the massive OB stars. We integrated the counts per second (CPS) within each galaxy or region and then applied $m_{FUV} = -2.5 \log(\text{CPS}) + 18.82$ (Morrissey et al. 2005) to derive the magnitude in the FUV -band. We compile the m_{FUV} found for each galaxy in Table 2. We then corrected by extinction using $A_{FUV} = 7.9E(B - V)$ –the value of $E(B - V)$ adopted for every region was derived from our optical spectroscopy and it is compiled in Table 5 of Paper I– and then apply

$$f_{FUV} = 1.40 \times 10^{-15} \times 10^{0.4(18.82 - m_{FUV}^0)}, \quad (12)$$

where $m_{FUV}^0 = m_{FUV} - A_{FUV}$ and f_{FUV} is obtained in units of $\text{erg s}^{-1} \text{cm}^{-2} \text{\AA}^{-1}$. The value of f_{FUV} computed for each galaxy is also shown in Table 2. Once the FUV luminosity is computed ($L_{FUV} = 4\pi d^2 f_{FUV}$), the FUV -based SFR is derived applying the calibration provided by Salim et al. (2007),

$$SFR_{FUV} = 8.1 \times 10^{-41} L_{FUV}. \quad (13)$$

2.4. X-ray data

Finally, we also looked for the X-ray data available for our WR galaxy sample. Only four objects (HCG 31 AC, IRAS 08339+6517, Tol 9 and NGC 5253) have been observed at these high frequencies; their X -ray luminosities are compiled in Table 3. Beside these data, we will also use (see Section 3.3) the WR galaxy sample that Stevens & Strickland (1998a,b) observed in X-ray.

3. Analysis of the star formation rates

The star formation rate (SFR), defined as the stellar mass formed per unit time, is the standard parameter used to

Table 3. X-ray data available for our WR galaxy sample.

Galaxy	$\log L_{X,(0.2-2.0 \text{ keV})}$ [erg s^{-1}]	Ref.
HCG 31	40.88 ± 0.13	SS98
IRAS 08339+6517	41.45	SS98
Tol 9	$< 40.29^a$	FFZ82
NGC 5253	38.60 ± 0.18	SS98

^a This value was derived assuming the distance to Tol 9 and the flux quoted by FFZ82, $f_{0.5-3 \text{ keV}} < 1.2 \times 10^{-13} \text{ erg cm}^{-2} \text{ s}^{-1}$, and multiplying for 0.72 to correct for the X-ray range.

REFERENCES: FFZ82: Fabbiano, Feigelson & Zamorani (1982); SS98: Stevens & Strickland (1998b).

quantify the star formation activity in galaxies. The determination of the SFR is fundamental to get a proper understanding of the formation and evolution of the galaxies. As we said in the introduction, different techniques involving different data sets from UV to radio often yield to different SFR results. Part of the problem is related with the unknown amount of extinction within each particular galaxy (Calzetti 2001), such as the amount of dust obscuration depends on the galaxy mass, galaxy type, the chemical evolutionary state, gas content or even if the galaxy is interacting or merging with another independent object. As we explained in the previous section, FIR and radio data provide an extinction-free estimation of the SFR, while FUV emission nicely traces the very young stellar component. Here, we analyzed all the available multiwavelength data for our sample of WR galaxies, including our reddening-corrected $H\alpha$ estimations (see Paper I), to determine in a comprehensive way the SFR within these objects.

Table 4 compiles all FUV , U , B , $H\alpha$, H , FIR , $15 \mu\text{m}$, $60 \mu\text{m}$, and 1.4 GHz luminosities for the galaxies analyzed in this work. The U , B , and H luminosities were computed from the reddening-corrected absolute magnitudes in the U , B and H bands (see Paper I) using the standard equation $\log L_x = 0.4 \times (M_{x,\odot} - M_x)$, and considering $M_{U,\odot} = 5.58$ and $M_{B,\odot} = 5.48$ (Bessell, Castelli & Plez 1998) and $M_{H,\odot} = 3.35$ (Colina, Bohlin & Castelli 1996).

We used the values listed in Table 4 to estimate the SFR that each object is experiencing, following the different multi-wavelength techniques explained in the previous section. The values of the $H\alpha$ -based SFR are extracted from Paper I and consider the Kennicutt (1998) calibra-

Table 4. *FUV*, *U*, *B*, *H α* , *H*, *FIR*, 15 μm , 60 μm and 1.4 GHz luminosities for all galaxies analyzed in this work.

Galaxy	L_{FUV} [10^{39} erg s $^{-1}$ \AA^{-1}]	L_U [$10^8 L_\odot$]	L_B [$10^8 L_\odot$]	$L_{H\alpha}$ [10^{40} erg s $^{-1}$]	L_H [$10^8 L_\odot$]	L_{FIR} [10^{42} erg s $^{-1}$]	$L_{15\ \mu\text{m}}$ [10^{22} W Hz $^{-1}$]	$L_{60\ \mu\text{m}}$ [10^{23} W Hz $^{-1}$]	$L_{1.4\ \text{GHz}}$ [10^{20} W Hz $^{-1}$]
HCG 31	49 \pm 3	356	202 \pm 7	52 \pm 4	42.2	72 \pm 6 ^a	3.9 \pm 0.7 ^a	14.1 \pm 1.1 ^a	98 \pm 14
" AC	24.9 \pm 1.5	175	92 \pm 4	36.3 \pm 2.3	18.0	79 \pm 11
" B	11.0 \pm 0.9	73.8	47.4 \pm 1.8	3.1 \pm 0.3	10.0	7.5 \pm 1.1
" E	1.51 \pm 0.12	6.3	3.13 \pm 0.17	1.49 \pm 0.16	0.586
" F ^b	1.52 \pm 0.15	10.9	4.0 \pm 0.2	5.0 \pm 0.3	0.486
" H	0.13 \pm 0.05	0.045 \pm 0.013
" G	10.3 \pm 0.6	90.4	55 \pm 2	6.4 \pm 0.4	13.1	11.9 \pm 1.8
Mkn 1087	...	1803	1127 \pm 83	70 \pm 5	360	228 \pm 23	15 \pm 4	45 \pm 5	178 \pm 9
" N	26.1 \pm 0.9	2.27 \pm 0.19	5.01
Haro 15	84 \pm 5	614	347 \pm 13	42 \pm 5	124	62 \pm 6	11 \pm 3	12.2 \pm 1.1	160 \pm 9
Mkn 1199	...	479	291 \pm 11	49 \pm 7	344	116 \pm 6	9.8 \pm 1.1	23.8 \pm 1.2	126 \pm 4
" NE	...	21.1	16.6 \pm 0.6	0.90 \pm 0.23	21.7
Mkn 5	0.274 \pm 0.018	4.21	2.63 \pm 0.10	0.582 \pm 0.014	1.89	<0.30	<0.087	0.036 \pm 0.007	3.9 \pm 0.8
IRAS 08208+2816	162 \pm 10	879	511 \pm 14	142 \pm 12	373	254 \pm 22	<5.5	49.7 \pm 4.0	657 \pm 26
IRAS 08339+6517	79 \pm 4	1159	661 \pm 23	120 \pm 6	592	198.6 \pm 1.8	18.3 \pm 1.8	42.6 \pm 0.3	249 \pm 37
" Comp.	1.17 \pm 0.10	38	29.9 \pm 1.6	2.1 \pm 0.4	23.3
POX 4	7.0 \pm 0.4	104.7	51.1 \pm 0.5	23.3 \pm 1.9 ^c	17.9	6.9 \pm 0.5	<24	1.56 \pm 0.14	10.4 \pm 1.2
" Comp.	0.667 \pm 0.075	2.42	2.17 \pm 0.07	0.188 \pm 0.018 ^c	1.1:
UM 420	25.4 \pm 1.4	236	103 \pm 4	47 \pm 3	57	142:	...	27.7	74 \pm 34
SBS 0926+606 ^b	41.4 \pm 3.4	52.3	26.6 \pm 0.8	11.8 \pm 0.7	9.49	5.8 \pm 0.6	2.8	1.01 \pm 0.17	10 \pm 2
" A	6.4 \pm 0.4	28.1	12.8 \pm 0.4	9.4 \pm 0.5	3.63
" B	35 \pm 3	24.2	13.8 \pm 0.4	2.4 \pm 0.2	5.86
SBS 0948+532	...	121.3	36.7 \pm 1.0	78 \pm 3	15.8	<38
SBS 1054+365	0.090 \pm 0.006	0.982	0.655 \pm 0.018	0.450 \pm 0.017	0.413	0.23 \pm 0.03	<0.042	0.041 \pm 0.005	0.098 \pm 0.011
SBS 1211+540	0.076 \pm 0.005	0.608	0.316 \pm 0.008	0.141 \pm 0.005	0.127	<0.50
SBS 1319+579	0.86 \pm 0.05	63.1	40.2 \pm 1.4	2.38 \pm 0.15	28.6	5.3:	...	0.85	<2.9
SBS 1415+437	0.409 \pm 0.023	1.69	1.00 \pm 0.03	0.50 \pm 0.02	0.581	<0.052
III Zw 107	...	286	177 \pm 5	40.1 \pm 1.8	77.3	50 \pm 8	<7.3	10.4 \pm 1.5	62 \pm 4
Tol 9	9.5 \pm 0.7	118	79 \pm 2	22.9 \pm 1.6	55.5	35.4 \pm 1.6	2.5 \pm 0.7	6.1 \pm 0.5	87.3 \pm 1.6
Tol 1457-262 ^b	38.6 \pm 2.6	319	182 \pm 5	63 \pm 3	109	82 \pm 6	<6.5	17.2 \pm 1.1	216 \pm 10
" Obj 1	29.2 \pm 1.6	223	121 \pm 3	46.2 \pm 2.7	58.6
" Obj 2	9.2 \pm 1.1	97.3	60.3 \pm 1.7	17.2 \pm 0.8	45.3
" #15	1.10 \pm 0.21	8.39	6.08 \pm 0.23	0.47 \pm 0.04	5.5:
Arp 252 ^b	47.4 \pm 3.3	711	435 \pm 13	90 \pm 6	423	361 \pm 19	38 \pm 5	79 \pm 4	1968 \pm 60
" ESO 566-8	38.5 \pm 2.7	597	350 \pm 10	84 \pm 6	313
" ESO 566-7	8.9 \pm 0.6	114	85 \pm 3	6.3 \pm 0.4	110
NGC 5253	2.35 \pm 0.15	36.6	22.9 \pm 0.2	4.4 \pm 0.2	14.2	2.583 \pm 0.009	0.479 \pm 0.004	0.571 \pm 0.001	1.64 \pm 0.07

^a As IRAS data do not allow to distinguish regions within the HCG 31 group, this value considers the flux of all galaxy members.

^b We are considering the flux of two galaxies: members F1 and F2 for HCG 31 F; galaxies A and B for SBS 0926+606; *obj 1* and *obj 2* for Tol 1457-262; and ESO 566-8 (A) and ESO 566-7 (B) for Arp 252.

^c As we commented in Paper I, the $H\alpha$ flux for POX 4 provided by Méndez & Esteban (1999) seems to be overestimated, hence we consider here the value provided by Gil de Paz, Madore & Pevunova (2003), that is 0.61 times smaller. We also scale our $H\alpha$ flux of POX 4 Comp using this factor.

tion. Recently, Calzetti et al. (2007) re-calibrated the relationship between the $H\alpha$ -luminosity and the SFR; the $H\alpha$ -based values of the SFR provided by Calzetti et al. (2007) are 0.67 times the values derived using the Kennicutt (1998) calibration.

Table 5 compiles all SFR values derived for each galaxy. From this table, it is evident that the agreement between values obtained using different methods is usually good, although sometimes we find clear discrepancies (i.e. POX 4, NGC 5253). We note that for systems that involve two or more galaxies (HCG 31, SBS 0926+606, Tol 1457-262 and Arp 252) we list both the global and individual SFRs, because the *FIR* and the radio data do not have enough spatial resolution to distinguish the emission coming from different members, but *FUV* and $H\alpha$ data do. We also considered HCG 31 F1 and F2 as a single entity (HCG 31 F) because the available HI data include both TDG candidates.

Figure 2 compares our $H\alpha$ -based SFR (corrected for both extinction and [N II] contribution as we explained in

Appendix C of Paper I) with the SFR estimations derived from *FIR*, 15 μm , 60 μm and 1.4 GHz luminosities. The diagram involving $L_{15\ \mu\text{m}}$ seems to show a higher scatter at higher SFR, but this calibration is more uncertain. As a particular case, Arp 252 always shows a disagreement between the SFR derived from $H\alpha$ and other parameters, remarking with the 1.4 GHz luminosity. The main object within Arp 252 is the bright galaxy ESO 566-8. This behavior, together the fact that the *FIR*-radio-continuum relation is not satisfied in this system (see below) strongly suggest that ESO 566-8 has some activity different to its starbursting nature (an AGN or a radio-galaxy), something we already commented when we analyzed this system (see Sect. 3.19.2 of Paper I). The rest of the objects agree rather well when comparing values obtained from different calibrations. As previous authors pointed out (i.e. Dopita et al. 2002; James et al. 2005), the correction of the $H\alpha$ fluxes for both extinction and [N II] emission is vital to get a reliable estimation of the SFR using $H\alpha$ -images.

Table 5. SFR values (in units of $M_{\odot} \text{ yr}^{-1}$) derived for each galaxy using different luminosities and calibrations. The references are: S07 = Salim et al. (2007); G84 = Gallagher et al. (1984); K98 = Kennicutt (1998); R01 = Roussel et al. (2001); C92 = Condon (1992); C02 = Condon et al. (2002) using the expression for $M > 5 M_{\odot}$. The last column indicates the assumed value of the SFR we estimate to each galaxy considering all available data.

Galaxy	<i>FUV</i>	<i>U</i>	<i>B</i>		<i>Hα</i>	<i>FIR</i>	15 μm	60 μm	1.4 GHz	Assumed
	S07	Eq. 15	G84	Eq. 14	K98 ^a	K98	R01	C92	C02	SFR ^b
HCG 31	4.0±0.3	2.8	0.59	2.5	4.1±0.4	3.3±0.3	1.2±0.2	2.8±0.2	2.5±0.2	3.1
" AC (NGC 1741)	2.02±0.12	1.5	0.27	1.2	2.88±0.18	1.98±0.03	2.0
" B	0.89±0.07	0.68	0.14	0.67	0.24±0.02	0.19±0.03	0.62
" E	0.122±0.009	0.073	0.009	0.057	0.118±0.013	0.10
" F	0.123±0.013	0.12	0.012	0.071	0.40±0.03	0.20
" G (Mkn 1090)	0.83±0.05	0.81	0.16	0.77	0.51±0.03	0.30±0.04	0.49
" H	0.011±0.004	0.004±0.001	0.008
Mkn 1087	...	12.1	3.27	11.8	5.6±0.4	10.3±1.1	4.6±1.3	8.8±1.0	4.5±0.2	6.3
" N	0.076	0.39	0.180±0.015	0.12
Haro 15	6.8±0.4	4.6	1.00	4.1	3.3±0.4	2.8±0.3	3.2±0.9	2.4±0.2	4.0±0.2	3.6
Mkn 1199	...	3.7	0.84	3.5	3.9±0.6	5.2±0.3	3.0±0.3	4.7±0.2	3.16±0.10	3.7
" NE	...	0.22	0.048	0.26	0.07±0.02	0.05
Mkn 5	0.022±0.0014	0.050	0.008	0.049	0.046±0.011	<0.014	<0.03	0.067±0.008	<0.10	0.040
IRAS 08208+2816	13.1±0.8	6.4	1.48	5.8	11.3±0.9	11.4±1.0	<1.68	9.7±0.8	16.4±0.7	11.6
IRAS 08339+6517	6.4±0.4	8.2	1.92	7.3	9.5±0.5	8.93±0.08	5.6 ± 0.6	8.36 ± 0.06	6.2±0.9	7.0
" Comp	0.095±0.008	0.37	0.087	0.44	0.17±0.02	0.10
POX 4	0.57±0.03	0.93	0.15	0.72	1.85±0.06	0.31±0.02	<7.48	0.31±0.03	0.26±0.03	0.54
" Comp	0.054±0.006	0.030	0.0063	0.041	0.012±0.004	0.031
UM 420	2.01±0.11	1.9	0.30	1.4	3.7±0.2	6.4 ^c	...	5.4 ^c	1.9±0.8	2.1
SBS 0926+606	3.4±0.3	0.50	0.08	0.40	0.94±0.06	0.26±0.03	<0.86	0.20±0.03	0.25±0.06	0.95
" A	0.53±0.03	0.28	0.04	0.20	0.75±0.04	0.52
" B ^d	2.82±0.25	0.25	0.04	0.22	0.19±0.02	1.4?
SBS 0948+532	...	1.1	0.11	0.53	6.2±0.2	<0.95	4.2
SBS 1054+365	0.0073±0.0005	0.013	0.0014	0.019	0.036±0.001	0.016	<0.01	0.015	0.025±0.004	0.018
SBS 1211+540	0.0062±0.0004	0.009	0.0007	0.009	0.011±0.001	<0.01	0.007
SBS 1319+579	0.069±0.004	0.59	0.12	0.58	0.189±0.012	0.24	...	0.17	<0.07	0.15
SBS 1415+437	0.0331±0.0018	0.022	0.0029	0.020	0.039±0.002	<0.01	0.030
III Zw 107	...	2.3	0.51	2.2	3.19±0.15	2.3±0.4	<2.24	2.0±0.3	1.52±0.09	2.0
Tol 9	0.77±0.06	1.0	0.23	1.1	1.82±0.13	1.59±0.07	0.8±0.2	1.19±0.08	2.18±0.04	1.3
Tol 1457-262	3.2±0.2	2.6	0.53	2.3	5.0±0.3	3.7±0.3	<1.99	3.4±0.2	5.4±0.3	3.8
" Obj 1	2.37±0.13	1.8	0.35	1.6	3.7±0.2	2.4
" Obj 2	0.74±0.09	0.87	0.17	0.83	1.37±0.06	0.83
" #15	0.089±0.017	0.09	0.018	0.10	0.038±0.003	0.06
Arp 252	3.84±0.26	5.3	1.26	5.0	7.2±0.5	16.2±0.9	11.6±1.4	15.4±0.8	49.2±1.5	10
" ESO 566-8	3.12±0.22	4.5	1.01	4.1	6.7±0.5	3.8
" ESO 566-7	0.72±0.04	1.0	0.25	1.1	0.50±0.04	0.53
NGC 5253	0.190±0.010	0.36	0.07	0.35	0.348±0.017	0.12	0.15	0.11	0.041±0.002	0.14

^a Considering the new correlation between the SFR and the $H\alpha$ -luminosity provided by Calzetti et al. (2007), the $H\alpha$ -based SFRs are 0.67 times the values shown here.

^b We consider the $H\alpha$ -based SFR values provided by the Calzetti et al. (2007) calibration to estimate the average SFR (see text).

^c The *FIR* and 60 μm luminosities in UM 420 are overestimated because of the contribution of the foreground galaxy UGC 01809 (see Fig. 13 and Sect. 3.9.1 in Paper I).

^d SBS 0926+606 B shows extended *FUV* emission, as it is seen in the right panel of Figure 1. The values of the SFR provided by its *FUV* and $H\alpha$ emission are very different.

Although the agreement between the $H\alpha$ -based SFR and the SFRs derived using *FIR* and radio luminosities is good, we observe that the values provided using the $H\alpha$ luminosities are slightly higher than those estimated using the other calibrations. The difference seems to be higher at lower $H\alpha$ -luminosities. A linear fit to the data (green continuous lines in Figure 2) confirms this trend. The zero-points of the fits (0.59, 0.52, 0.58, 0.68 for the $H\alpha$ -*FIR*, $H\alpha$ -1.4 GHz, $H\alpha$ -60 μm , and $H\alpha$ -15 μm relations, respectively) indicate that, for $\text{SFR}=1 M_{\odot} \text{ yr}^{-1}$, the value of the SFR provided by $H\alpha$ -luminosity is ~ 0.6 times the SFR values estimated using the other relations. Bell (2003) concluded that both radio and *FIR* luminosities underestimate the SFR for low-luminosity galaxies because the non-thermal emission seems to be suppressed by a factor of 2–3 in dwarf objects. However, the difference is not significant if we use the Calzetti et al.

(2007) calibration instead of the Kennicutt (1998) calibration to derive the $H\alpha$ -based SFR.

The comparison of the *FUV*-based with the $H\alpha$ -based SFR (Figure 3) also shows a good agreement: except for some few objects (remarkably SBS 0926+606 B¹) both relations provide similar values. We also observe that the *FUV*-based SFRs seem to be slightly lower than the $H\alpha$ -based SFRs. A linear fit to the data (shown in Figure 3 with a continuous green line and with a correlation coefficient of $r=0.927$) indicates that the *FUV*-based SFR is, on average, ~ 0.71 times the $H\alpha$ -based SFR. This value is similar to the factors found before when comparing the $H\alpha$ -based SFR with the *FIR*- and radio-

¹ As we commented before, the *FUV* emission observed in SBS 0926+606 B is much more extended than the $H\alpha$ emission, and hence the derived SFR is more than one order of magnitude higher using the *FUV* than the $H\alpha$ emission.

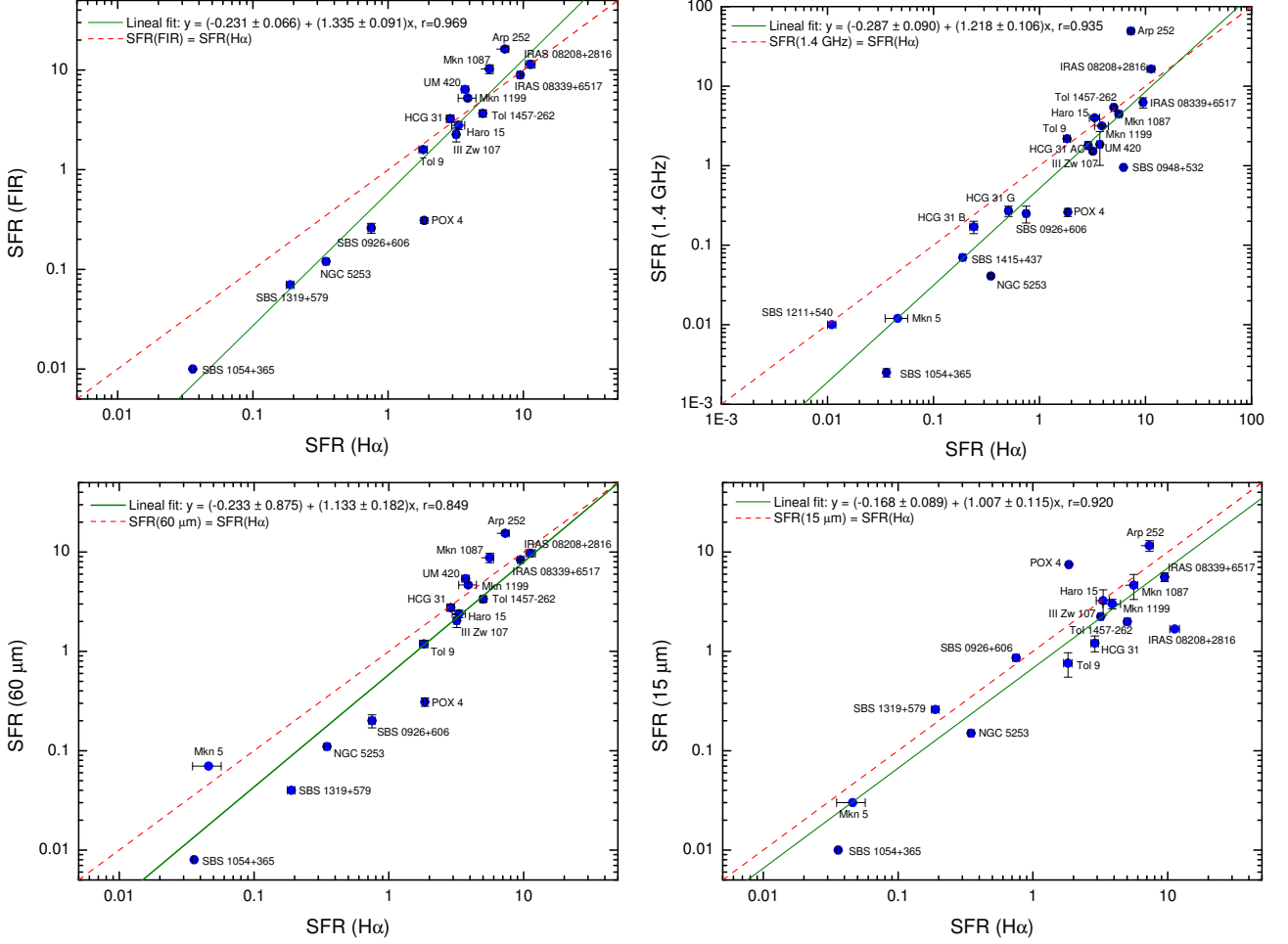


Fig. 2. Comparison between the $H\alpha$ -based SFR –corrected for both extinction and $[N II]$ contribution and assuming Kennicutt (1998), x-axis– with the SFRs derived using the FIR , $15 \mu m$, $60 \mu m$ and $1.4 GHz$ luminosities. The dotted red lines indicate the position with equal SFR, the continuous green lines show a lineal fit to the data.

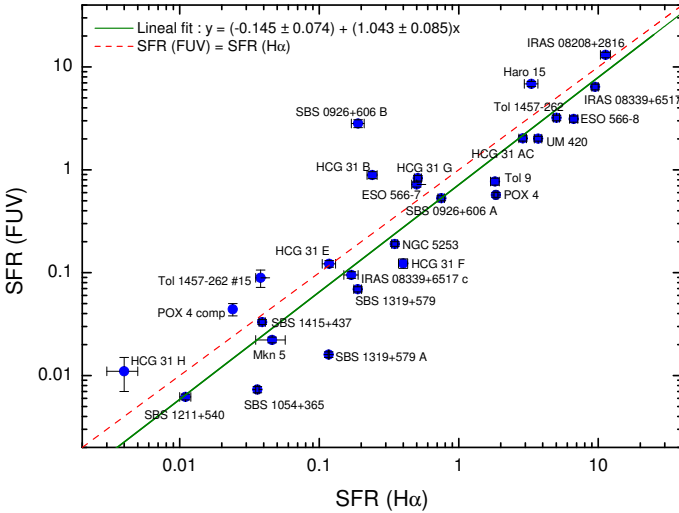


Fig. 3. Comparison between the $H\alpha$ -based SFR –corrected for both extinction and $[N II]$ contribution and assuming Kennicutt (1998), x-axis– with the SFRs derived using the FUV luminosities. The dotted red line indicates the position with equal SFR, while the continuous green line shows a fit to the data.

based SFRs. Interestingly, all these numbers are coincident with the ratio between the Kennicutt (1998) and the Calzetti et al. (2007) calibrations to the SFR using the $H\alpha$ flux, $SFR_{C07}(H\alpha)/SFR_{K98}(H\alpha)=0.67$. We therefore conclude that the new $H\alpha$ -based calibration provided by Calzetti et al. (2007) should be preferred over the widely-used Kennicutt (1998) calibration when computing the SFR from $H\alpha$ luminosities. The SFR estimated for each object considering all available multiwavelength data, and listed in last column of Table 5, has been computed considering the Calzetti et al. (2007) value. Finally, we must say that there are increasing evidences that the $H\alpha$ luminosity underestimates the SFR relative to the FUV luminosity in dwarf galaxies with $SFR \leq 0.01 M_{\odot} yr^{-1}$ (i.e., Lee et al. 2009) and hence the FUV -based SFR should be preferred over the $H\alpha$ -based SFR in those systems.

3.1. L_B -SFR and L_U -SFR relations for starburst galaxies

Just for comparison, we also estimated the SFR from the B -luminosity using the calibration provided by Gallagher et al. (1984). SFR_B represents the star formation activity occurred in the last few hundreds of Myr, while the rest of the calibrations are tracing the massive stars and the nebular emission of the gas that only last for some few tens of Myr.

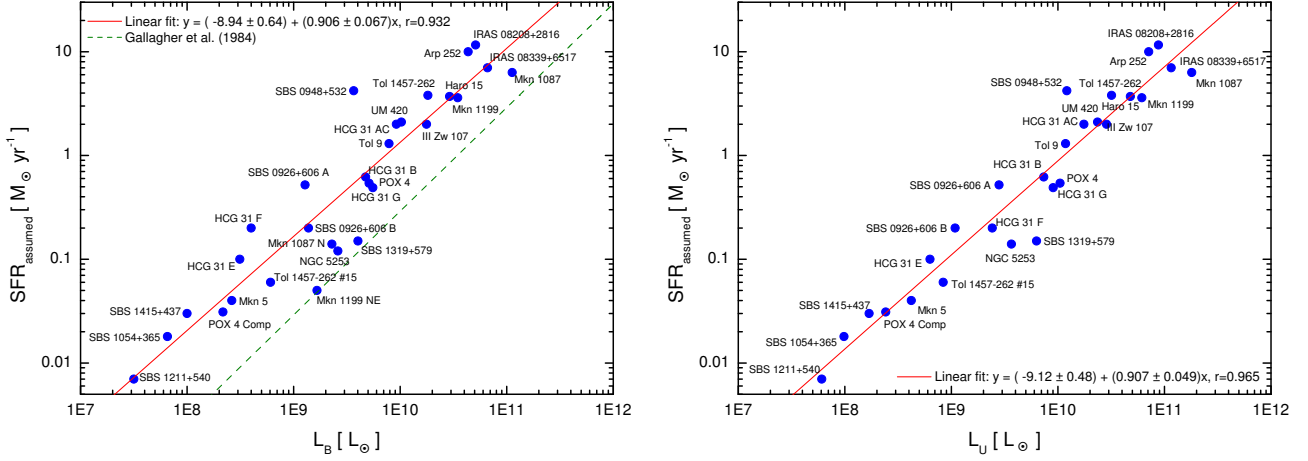


Fig. 4. Assumed SFR vs. B -luminosity (left panel) and U -luminosity (right panel) for the analyzed galaxies. Luminosities are plotted in solar units. The best fit (in logarithm scale) to our data are plotted with a continuous red line. The previous calibration given by Gallagher et al. (1984) between the SFR and the B -luminosity is shown by a discontinuous green line.

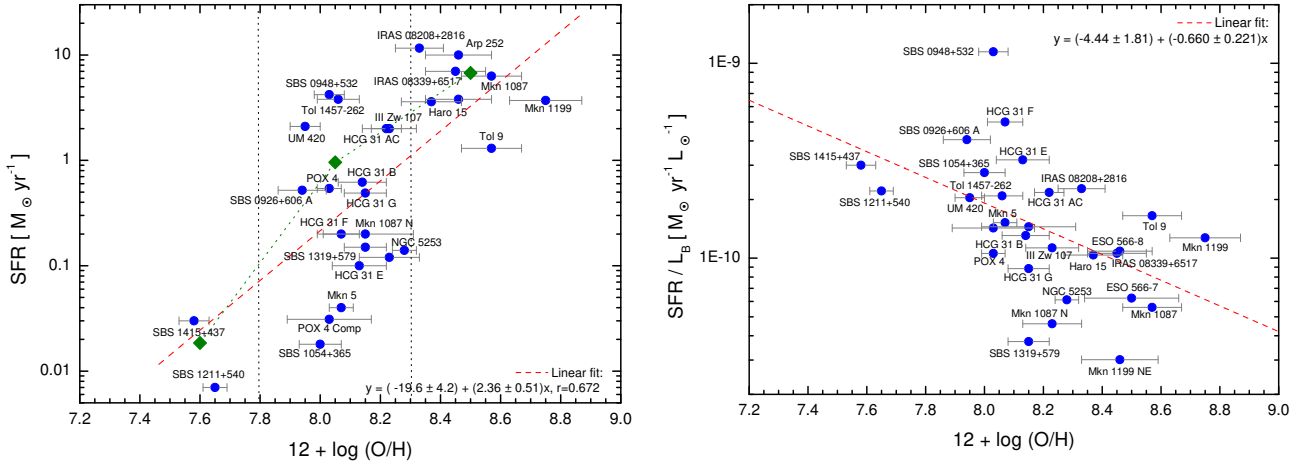


Fig. 5. SFR vs $12+\log(\text{O}/\text{H})$ (left) and SFR/L_B vs $12+\log(\text{O}/\text{H})$ (right) for our sample of WR galaxies. The red-dotted line indicates a fit to our data. Green diamonds in left panel plot the average value obtained in the low, intermediate and high-metallicity regimes.

For our galaxy sample, SFR_B is always lower than the SFR derived from the other calibrations, as we should expect because of the starbursting nature of the analyzed galaxies. The value of the SFR_B in Mkn 1087 using Gallagher et al. (1984) equation is only half of that estimated from other calibrators, remarking its Luminous Blue Compact Galaxy (LCBG) nature (López-Sánchez et al. 2004b).

We used our data to establish a new relation between the SFR and the B -luminosity, that should be applied only in starburst galaxies and just as a first estimation of the actual SFR. The left panel of Figure 4 shows the relation between L_B (in solar units) and the assumed SFR for all our galaxies. Despite some clear discrepancies between some galaxies that show very different SFR for a similar B -luminosity (for example, just compare members G and F of HCG 31), we observe a good agreement, having galaxies with higher B -luminosities higher star-formation activity. The discrepancies are consequence of the different star-formation histories of the galaxies (relative contribution and age of the underlying stellar population, metallicity,

age of the most recent star-formation event). A linear fit to our data provides the relation

$$\text{SFR}_{B,\text{starbursts}} = 1.148 \times 10^{-9} L_B^{0.906} \quad (14)$$

being L_B expressed in units of L_\odot . The correlation coefficient of this fit is $r=0.932$. The third column in Table 5 compiles the SFR_B computed for each galaxy using this equation. The relation obtained by Gallagher et al. (1984) gives values one order of magnitude lower than those we obtain with our new calibration.

We also computed a relation between the SFR and the U -luminosity for our sample galaxies. The right panel of Figure 4 shows such relation. A linear fit to the data yields

$$\text{SFR}_{U,\text{starbursts}} = 7.59 \times 10^{-10} L_U^{0.907}, \quad (15)$$

being L_U expressed in units of L_\odot . This fit has somewhat smaller scatter than our derived $\text{SFR}-L_B$ relation, resulting in a correlation coefficient $r=0.965$. However, the slope for both calibrations (0.894 ± 0.070 and 0.900 ± 0.054 for $\text{SFR}-L_B$ and $\text{SFR}-L_U$, respectively) are similar. We remark that Equations 14 and 15 can not be applied to galaxies with

no strong star-formation activity, because the SFR value derived from them will be overestimated (as it is happening in Mkn 1199 NE or IRAS 08339+6517 comp).

3.2. Comparison of SFR and metallicity

Left panel of Figure 5 compares the assumed SFR with the oxygen abundance computed for each galaxy. We estimated the average SFR values in the low ($12+\log(\text{O}/\text{H}) < 7.8$), intermediate ($7.8 < 12+\log(\text{O}/\text{H}) < 8.3$) and high ($12+\log(\text{O}/\text{H}) > 8.3$) metallicity regimes, then we plot in this figure using green diamonds. As we see, the dispersion in the intermediate-metallicity range is quite high, but that is just a consequence of the star-formation history of each particular galaxy (see Paper IV), as in this metallicity regime lies both very dwarf objects (i.e., Mkn 5, SBS 1054+365) and large and bright star-forming galaxies (i.e., Tol 1456-262, III Zw 107) which share a relatively similar chemical history. Besides the large dispersion in the intermediate-metallicity regime, it is clear that galaxies with higher metallicity have higher global star formation rates. That is a consequence of the building of the galaxies, because more massive objects are more metal-rich than less massive galaxies (see below) and, hence, when the starburst is initiated, galaxies with higher mass (and with higher metallicities) will create stars at a higher rate than those found in smaller objects. The comparison of the SFR per B -luminosity, SFR/L_B with the metallicity (Figure 5, right) also shows a tremendous dispersion for $12+\log(\text{O}/\text{H})$ between 8.0 and 8.2. However, we observe that SFR/L_B decreases with increasing oxygen abundance (the red-dotted line shows a fit to the data), indicating that galaxies with lower metallicity (and, therefore, less massive objects) have stronger star-forming bursts than those found in higher metallicity (more massive) objects. SBS 0948+532 has the highest SFR/L_B in our sample, indicating the strength of the starburst, as we saw when analyzed its photometric properties (see Sect. 3.11 in Paper I). On the other hand, SBS 1319+579 has a very low SFR/L_B in comparison with BCDGs of similar characteristics, indicating the peculiarity of this galaxy. We will see below that other properties of SBS 1319+579 show additional discrepancies with the average behavior in BCDGs, suggesting that the star-formation activity has been somewhat suppressed in this object. For example, the gas depletion timescale is extremely long for a starburst galaxy, ($\tau \sim 12.7$ Gyr, see Table 6).

3.3. A L_X -SFR relation for starburst galaxies

Although several relations between the X-ray luminosity and the star formation rate have been proposed (i.e., Ranalli et al. 2003; Lou & Bian 2005) they seem not to be appropriate for young starbursting systems. For example, as we explained in the analysis of the LCBG IRAS 08339+6517 (López-Sánchez et al. 2006), the relation provided by Ranalli et al. (2003) gives a very high SFR value ($61.8 M_\odot \text{yr}^{-1}$) in comparison with the estimations obtained using other frequencies ($6\text{--}8 M_\odot \text{yr}^{-1}$). Stevens & Strickland (1998a) showed that the X-ray luminosities in WR galaxies are substantially higher than those found in non-WR galaxies with similar B -luminosity. That

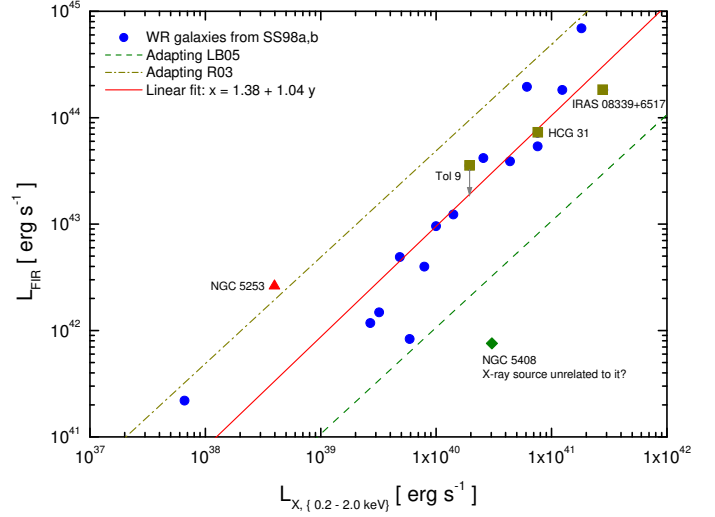


Fig. 6. X-ray luminosity in the 0.2–2.0 keV range vs. FIR luminosity for the sample of WR galaxies analyzed by Stevens & Strickland (1998a,b). The red continuous line is the best fit to the data, excluding the values for NGC 5253 and NGC 5408. The green discontinuous line is the relation obtained using the $\text{SFR}-L_X$ calibration provided by Lou & Bian (2005), while the yellow dotted-dashed line is the relation obtained from the Ranalli et al. (2003) calibration. The three additional WR galaxies of our sample for which X-ray data are available (HCG 31, IRAS 08339+6517, and Tol 9) are indicated with dark yellow squares.

is a consequence of the higher rate of superbubbles and supernova explosions in WR galaxies.

We have used the sample of WR galaxies analyzed by Stevens & Strickland (1998a,b) to get a tentative calibration between SFR and L_X for this kind of objects. These authors obtained X-ray data in the 0.2–2.0 keV range using the satellite ROSAT. We have checked which of these galaxies also possess FIR data from the IRAS satellite, and established a relation between L_{FIR} and L_X , as it is shown in Figure 6. Only 18 galaxies have available data for both luminosities. NGC 5253 was included in the Stevens & Strickland (1998a,b) analysis, but they indicated that the X-ray emission in this object is very peculiar. The X-ray emission measured in NGC 5408 may be unrelated with the galaxy. Hence, neglecting the contribution of these two galaxies, the linear fit to the data gives

$$L_{FIR} = 24 \times L_X^{1.04}, \quad (16)$$

being the correlation coefficient $r=0.929$. Considering the calibration given by Kennicutt (1998) between L_{FIR} and SFR (Equation 6), we find the following calibration between soft X-rays (0.2–2.0 keV) and SFR:

$$\text{SFR}_X = 1.08 \times 10^{-42} L_X^{1.04}. \quad (17)$$

As it can be seen in Figure 6, our new $\text{SFR}-L_X$ calibration agrees better with the observational data than the relations explained before. Indeed, Lou & Bian (2005) relation gives values around one order of magnitude lower than those expected from the FIR luminosity, but Ranalli et al. (2003) calibration provides values almost one order of magnitude higher than the actual ones. Using our new relation and the available X-ray data for our WR galaxies (see Table 3), we derive a SFR_X of 3.5, 13.8, and $0.86 M_\odot \text{yr}^{-1}$ for HCG 31,

Table 6. Additional *FIR* and radio properties.

Galaxy	q^a	$\log R^b$	τ_g [Gyr]
HCG 31 AC	2.39	1.19	1.92
HCG 31 B	...	1.25	5.3
HCG 31 F	2.9
HCG 31 G	...	1.11	2.3
Mkn 1087	2.53	1.30	3.3
Haro 15	2.01	1.48	1.9
Mkn 1199	2.39	1.31	0.40
Mkn 5	2.1
IRAS 08208+2816	2.01	1.57	...
IRAS 08339+6517	2.33	1.21	0.89
POX 4	2.25	0.93	4.2
UM 420	2.71	1.08	...
SBS 0926+606	2.18	0.79	2.0 (A), 5.6 (B)
SBS 0948+532
SBS 1054+365	2.79	-0.10	4.0
SBS 1211+540	3.5
SBS 1319+579	2.15	...	12.7
SBS 1415+437	3.5
III Zw 107	2.34	1.06	3.5
Tol 9	2.03	1.16	1.95
Tol 1457-262	2.00	1.43	1.51
Arp 252	1.69	2.28	...
NGC 5253	2.62	0.33	0.97

^a The logarithmic ratio of *FIR* to radio flux density parameter, q , is defined in Equation 20.

^b R is the non-thermal to thermal ratio, derived from the 1.4 GHz and $H\alpha$ fluxes.

^c The gas depletion timescale is defined as $\tau_g = 1.32M_{\text{HI}}/\text{SFR}$ (Skillman et al. 2003)

IRAS 08339+6517, and Tol 9, respectively. These values agree well with the actual SFR estimated for each object (see Table 5).

4. FIR/radio correlation

We have used the luminosity data shown in Table 4 to check if our WR galaxies follow the *FIR*/radio correlation. As it was shown by Condon et al. (1992), the *FIR*/radio correlation is much tighter for starbursts than for active galaxies. Figure 7 (left) plots the 1.4 GHz luminosity vs. the 60 μm luminosity for our sample galaxies and the relation between both quantities found by Yun, Reddy & Condon (2001),

$$L_{1.4\text{GHz}} [\text{W Hz}^{-1}] = 10^{12} L_{60\ \mu\text{m}} [L_{\odot}], \quad (18)$$

while Figure 7 (right) shows $L_{1.4\text{GHz}}$ vs. the total *FIR* luminosity and the relation given by Condon et al. (1991),

$$\log L_{1.4\text{GHz}} [\text{W Hz}^{-1}] = 1.1 \log L_{\text{FIR}} [L_{\odot}] + 10.45. \quad (19)$$

Bell (2003) remarked that the radio-*FIR* correlation is linear not because both radio and *FIR* emission track SFR, but rather because they fail to track SFR in independent, but coincidentally quite similar, ways. Further analysis (i.e., Hunt et al. 2005) also found that this relation is not hold for some low-metallicity or young starbursts galaxies. However, as it is seen in Figure 7, all analyzed objects except Mkn 5 (which has a very uncertain value for *FIR*) and Arp 252 (ESO 566-8 hosts some kind of nuclear activity) follow well both relations. This indicates that the galaxies are starbursting systems and are not active galaxies (Seyfert or

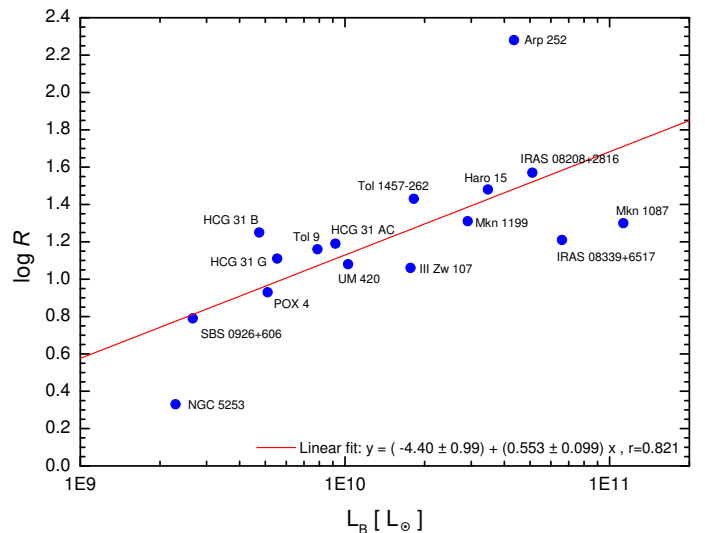


Fig. 8. Comparison of the *B*-luminosity (in solar units) and the logarithmic non-thermal to thermal ratio, $\log R$, for our sample galaxies. A linear fit is shown with a continuous red line.

AGNs). We already reached this conclusion when we analyzed the diagnostic diagrams involving several emission-line ratios (see Paper III). Figure 7 includes a linear fit (in logarithmic scale) to our data (neglecting Mkn 5, for which the *FIR* values have high uncertainties). The relation given by Condon et al. (1991) seems to be slightly displaced with respect our observational data, although we also see some small discrepancies in the Yun, Reddy & Condon (2001) relation for the faintest objects.

The non-AGN nature of our sample of WR galaxies is also supported by the analysis of the q parameter and the *FIR* spectral index. The q parameter is defined as the logarithmic ratio of *FIR* to radio flux density,

$$q \equiv \log \frac{F_{\text{FIR}} (\text{W m}^{-2}) / 3.75 \times 10^{12} \text{ Hz}}{S_{1.4 \text{ GHz}} (\text{W m}^{-2} \text{ Hz}^{-1})}, \quad (20)$$

and it is very robust for most galaxy populations: $\langle q \rangle = 2.34 \pm 0.19$ (Condon et al. 1991; Yun et al. 2001). Galaxies with $q < 1.8$ are more than 3 times more radio loud than the mean for the star-forming galaxies, so they can be classified as AGN-powered. As it seen in Table 6, all galaxies except Arp 252 have a q value similar to that expected for starburst galaxies.

Table 6 also compiles the non-thermal to thermal ratio, R , of the galaxies with available 1.4 GHz radio-continuum data. The thermal flux at 1.4 GHz was computed applying Equation 5. The majority of the galaxies show the typical value for star-forming galaxies, $\log R = 1.3 \pm 0.4$ (Dopita et al. 2002). The low value in R found in POX 4 and NGC 5253 may be because the $H\alpha$ flux has been overestimated, although the situation of NGC 5253 is far from clear (López-Sánchez et al. 2010a). The value obtained for SBS 1054+365 is not reliable, we consider that or the 1.4 GHz flux was underestimated (very probably) or the $H\alpha$ flux was overestimated. However, the high value found in Arp 252 (the emission comes mainly from ESO 566-8), $\log R = 2.28$, is real and indicates that the thermal flux at 1.4 GHz is less than 0.5%. As reported by several authors (i.e., Klein, Wielebinski & Thuan 1984; Klein, Weiland & Brinks 1991; Bell 2003), dwarf galaxies seem to have a lower

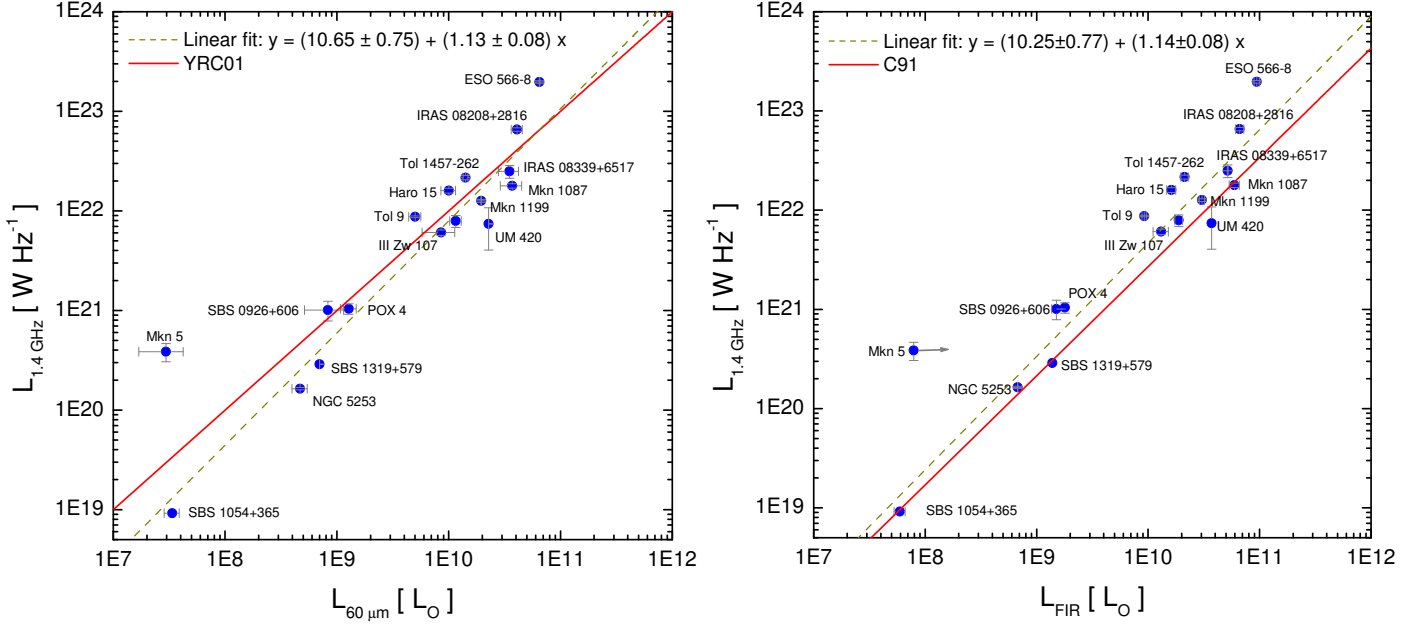


Fig. 7. 1.4 GHz radio-continuum luminosity vs. the $60\mu\text{m}$ luminosity (left) and the FIR luminosity (right). The relations derived by Yun, Reddy & Condon (2001) (Equation 18, left diagram) and Condon et al. (1991) (Equation 19, right diagram) are plotted with a red continuous line. The best linear fits to our data (in logarithmic units) are shown with a yellow dashed line.

non-thermal-to-thermal emission ratio than normal spiral galaxies. The values obtained for the R parameter in our galaxy sample tend to be lower at lower B -luminosities, as it is shown in Figure 8. The difference between dwarf and larger galaxies is often interpreted as higher efficiency of cosmic-ray confinement in more massive galaxies (e.g., Klein et al. 1984; Price & Duric 1992; Niklas, Klein & Wielebinski 1997; Bell 2003).

5. Analysis of the masses

For this work, we have estimated the ionized gas mass $-M_{\text{HII}}$, using the $\text{H}\alpha$ images presented in Paper I–; neutral gas mass $-M_{\text{HI}}$, using HI data at 21 cm compiled from the literature–; mass of the ionizing star cluster $-M_*$, using $\text{H}\alpha$ and $W(\text{H}\beta)$, see Paper I–; warm dust mass $-M_{\text{dust}}$, using the FIR fluxes–; Keplerian mass $-M_{\text{Kep}}$, via the kinematics of the ionized gas–; and dynamical mass $-M_{\text{dyn}}$, using the HI kinematics–. All these data are compiled in Table 7. The estimation of M_{Kep} and M_{dyn} for each galaxy was explained in Paper II. We just remember that, as the extension of the neutral gas is usually larger than the stellar component, our estimations of M_{dyn} are very probably underestimated. Furthermore, no-rotational movements would yield in an overestimation of the total mass. Only interferometric HI analysis can definitely provide a more precise determination of the dynamical mass of each system. However, we may use our M_{dyn} values as a rough estimation of the total mass of the systems. Their comparison with M_{Kep} , M_{HI} , M_{HII} , M_{dust} and their associated mass-to-light ratios will give clues about the galaxy type, dynamics and the fate of the neutral gas.

We first compare all mass determinations with the optical luminosity of the galaxies. Figure 9 shows the relations between M_{HII} , M_{HI} , M_{dust} and M_* with the absolute B -magnitude. As we should expect, and besides some scatter, all mass determinations clearly increase with increasing op-

tical luminosity. We have performed a linear fit to the data; the results are:

$$\log M_{\text{HII}} = (-0.21 \pm 0.56) - (0.342 \pm 0.030)M_B, \quad (21)$$

$$\log M_{\text{HI}} = (3.69 \pm 0.52) - (0.292 \pm 0.028)M_B, \quad (22)$$

$$\log M_{\text{dust}} = (-1.15 \pm 0.92) - (0.364 \pm 0.047)M_B, \quad (23)$$

$$\log M_* = (-0.47 \pm 0.54) - (0.397 \pm 0.029)M_B, \quad (24)$$

with correlation coefficients of 0.899, 0.922, 0.912 and 0.928, respectively. Some deviations to the fits are found in Mkn 1199 (that possesses a relatively low M_{HI}), SBS 0948+532 (with a very high M_{HII}), POX 4 (it seems to be M_{dust} deficient, while its ionized gas mass may be overestimated), UM 420 (its high M_{dust} is very probably consequence of the contamination of the FIR emission by the foreground galaxy UGC 01809, see Sect. 3.9 in Paper I and Sect. 3.9 in Paper II), SBS 1319+579 and IRAS 08339+6517 Comp (that have a very low M_* for their absolute B -magnitude) and NGC 5253 (that is both M_{HI} and M_{dust} deficient).

Figure 10 plots the dynamical mass (that represents the total mass of the galaxy) versus the absolute magnitude in several broad-band filters (B , V , R and J). We find a clear correlation between these quantities, a linear fit to the data yields:

$$\log M_{\text{dyn}} = (4.37 \pm 0.58) - (0.304 \pm 0.032)M_B, \quad (25)$$

$$\log M_{\text{dyn}} = (4.28 \pm 0.55) - (0.306 \pm 0.030)M_V, \quad (26)$$

$$\log M_{\text{dyn}} = (3.86 \pm 0.57) - (0.324 \pm 0.030)M_R, \quad (27)$$

$$\log M_{\text{dyn}} = (4.60 \pm 0.65) - (0.281 \pm 0.034)M_J, \quad (28)$$

with correlation coefficients r of 0.922, 0.931, 0.940 and 0.907, respectively. Notice that slopes in all fits are quite similar. The most important deviations to these fits are found in clearly interacting systems (Mkn 1199 and HCG 31 AC) but also in Mkn 5 and SBS 1054+365.

We have compared the Keplerian mass (derived from the kinematics of the ionized gas) with the dynamical

Table 7. Keplerian mass (M_{Kep}), dynamical mass (M_{dyn}), neutral gas mass (M_{HI}), ionized gas mass (M_{HII}), warm dust mass (M_{dust}), mass of the ionizing star cluster (M_{\star}), total stellar mass (M_{stars}), and baryonic mass (M_{bar}) of the galaxies analyzed in this work.

Galaxy	M_{Kep} [$10^8 M_{\odot}$]	M_{dyn} [$10^8 M_{\odot}$]	M_{HI} [$10^8 M_{\odot}$]	M_{HII} [$10^6 M_{\odot}$]	M_{dust}^a [$10^6 M_{\odot}$]	M_{\star} [$10^6 M_{\odot}$]	M_{stars} [$10^8 M_{\odot}$]	M_{bar} [$10^8 M_{\odot}$]
HCG 31	74.6	7.8±0.5	2.56	37.8±2.8	33.8	141
" AC	340	850	36.4	5.4±0.3	...	18.2±1.2	14.4	62.5
" B	26	54	19.4	0.45±0.04	...	8.2±0.7	8.0	33.6
" E	...	13 ^b	...	0.22±0.02	...	2.6±0.3	0.47	...
" F	3.0	15	6.13	0.75±0.04	...	0.40±0.03	0.39	8.5
" G	21	68	19.4	0.96±0.05	...	7.0±0.4	10.5	36.1
Mkn 1087	560	1800	156	10.4±9.7	7.8	129±9	288	494
" N	2.2	45 ^b	...	0.337±0.028	...	3.34±0.28	4.0	...
Haro 15	121	365	55±18	6.2±0.7	2.1	77±9	99.2	172
Mkn 1199	82	1650	12.2	7.3±1.1	3.1	140±21	275	291
" NE	2.9	70 ^b	...	0.13±0.03	...	1.7±0.4	17.4	...
Mkn 5	21	36	0.72±0.09	0.081±0.010	0.099	0.300±0.012	1.5	2.5
IRAS 08208+2816	39	600 ^b	...	21.1±1.7	8.84	166±14	298	...
IRAS 08339+6517	100	370	53±6	14.5±0.7	3.91	226±10	476	546
" Comp	80	100	7.0±0.9	0.26±0.03	...	4.1±0.5	18.6	27.9
POX 4	5.0	76	21	5.70±0.18	0.093	9.8±0.3	14.3	29.1
" Comp	0.05	...	0.79±0.07	0.88	...
UM 420	21	200 ^b	...	6.9±0.4	5.0 ^c	13.8±0.9	45.6	...
SBS 0926+606	17.7±7.2	1.75±0.10	0.37	8.4±0.6	7.59	30.9
" A	...	23	9.6±3.6	1.40±0.07	...	3.59±0.17	2.9	15.5
" B	...	45	8.1±3.6	0.35±0.03	...	4.8±0.4	4.7	15.4
SBS 0948+532	21	90 ^b	...	11.6±0.4	...	18.8±0.7	12.6 ^d	...
SBS 1054+365	0.78	15	0.61±0.06	0.067±0.003	0.012	0.23±0.01	0.33	1.13
SBS 1211+540	1.13	1.14	0.24±0.04	0.021±0.001	...	0.05	0.102 ^d	0.420
SBS 1319+579	86	140	16.4	0.35±0.02	0.30	0.78±0.05	22.9	44.5
SBS 1415+437	2.5	4.9	0.96±0.07	0.074±0.003	...	0.14±0.01	0.46	1.74
III Zw 107	8.2	180	67±12	6.0±0.3	1.25	74±3	61.8	150
Tol 9	12	580 ^e	22±2	3.4±0.2	2.41	27.4±1.9	44.4	106
Tol 1457-262	...	950	47	9.4±0.5	1.83	41±2	87.2	149
" Obj 1	62	290 ^b	...	6.9±0.4	...	23.4±1.5	46.9	...
" Obj 2	...	150 ^b	...	2.56±0.12	...	14.4±0.7	36.2	...
Arp 252	13.4±0.9	6.32	82.3±4.9	338	...
" ESO 566-8	73	440 ^b	...	12.5±0.8	...	45±3	250	...
" ESO 566-7	4	150 ^b	...	0.93±0.07	...	16.8±1.2	88	...
NGC 5253	...	83 ^e	1.63±0.10	0.65±0.03	0.042	2.22±0.11	11.4	13.6

^a This value is for the entire system: all galaxies in the HCG 31 group, members A and B in SBS 0926+606, all galaxies in Tol 1457-262, and ESO 566-8 and ESO 566-7 in Arp 252. We neglect the contribution of the *FIR* emission in dwarf objects associated to larger galaxies (companion objects surrounding Mkn 1087, Mkn 1199, IRAS 08339+6519, and POX 4).

^b Tentative value of M_{dyn} computed using Equations 25–28 and 29.

^c The warm dust mass is very probably overestimated because of the *FIR* contribution of the foreground galaxy UGC 01809.

^d M_{stars} computed assuming $V - J \sim 0.8$ and $J - H \sim 0.3$.

^e The detailed analysis of the H I gas and its kinematics will be presented elsewhere (LS+10).

mass (estimated from the kinematics of the neutral gas). Figure 11 plots both sets of values. As we expected, M_{Kep} is lower than M_{dyn} for almost all cases ($M_{\text{Kep}}=M_{\text{dyn}}$ is shown by a dotted green line in Figure 11). Although the dispersion is high –and we remember that M_{Kep} and/or M_{dyn} may be overestimate because of interaction features– we have performed a tentative fit to the data, that yield

$$M_{\text{dyn}} = 0.584 \times M_{\text{Kep}}^{1.114}. \quad (29)$$

with a correlation coefficient $r = 0.827$. This relation is included in Figure 11 as a red dashed line. As we explained in Sect. 3.13 of Paper II, M_{Kep} in SBS 1211+540 has been probably overestimated, so we did not consider this point in the analysis. The relation indicates that M_{Kep} is between 12% (for $M_{\text{dyn}}=10^{11} M_{\odot}$) and 24% (for $M_{\text{dyn}}=10^8 M_{\odot}$) the total dynamical mass. Hence, as we should expect, more massive galaxies have a higher $M_{\text{dyn}}/M_{\text{Kep}}$ ratio, indicating that the kinematics of the ionized gas is not appropriate to derive the total dynamical mass in those objects.

Using Equations 25–28 and 29 we have computed a tentative value for the dynamical mass in the galaxies with lack of H I data. We have included the results in Table 7, and plotted these points in Figure 11 (dark yellow diamonds). As we can see, they match well with the positions of the galaxies for which M_{dyn} was derived from H I data, but we will not consider these points in the subsequent analysis.

We prefer to use our *NIR* data to derive a proper value of the stellar mass of all the galaxies. Following the description provided by Kirby et al. (2008), we may assume a *H*-band mass-to-light ratio of $M_{\text{stars}}/L_H=0.8$ to compute the stellar mass, M_{stars} , from the *H*-luminosity (that is compiled for all objects in Table 4). This assumption is well supported by both observations (Bell 2003; Kirby et al. 2008) and theory (de Jong 1996), and considers a 12 Gyr old solar metallicity stellar population with a constant star-formation rate and Salpeter initial mass function. Hence, the *H*-band mass-to-light ratio may be somewhat overestimated for our young galaxies. Combining the *H*-band de-

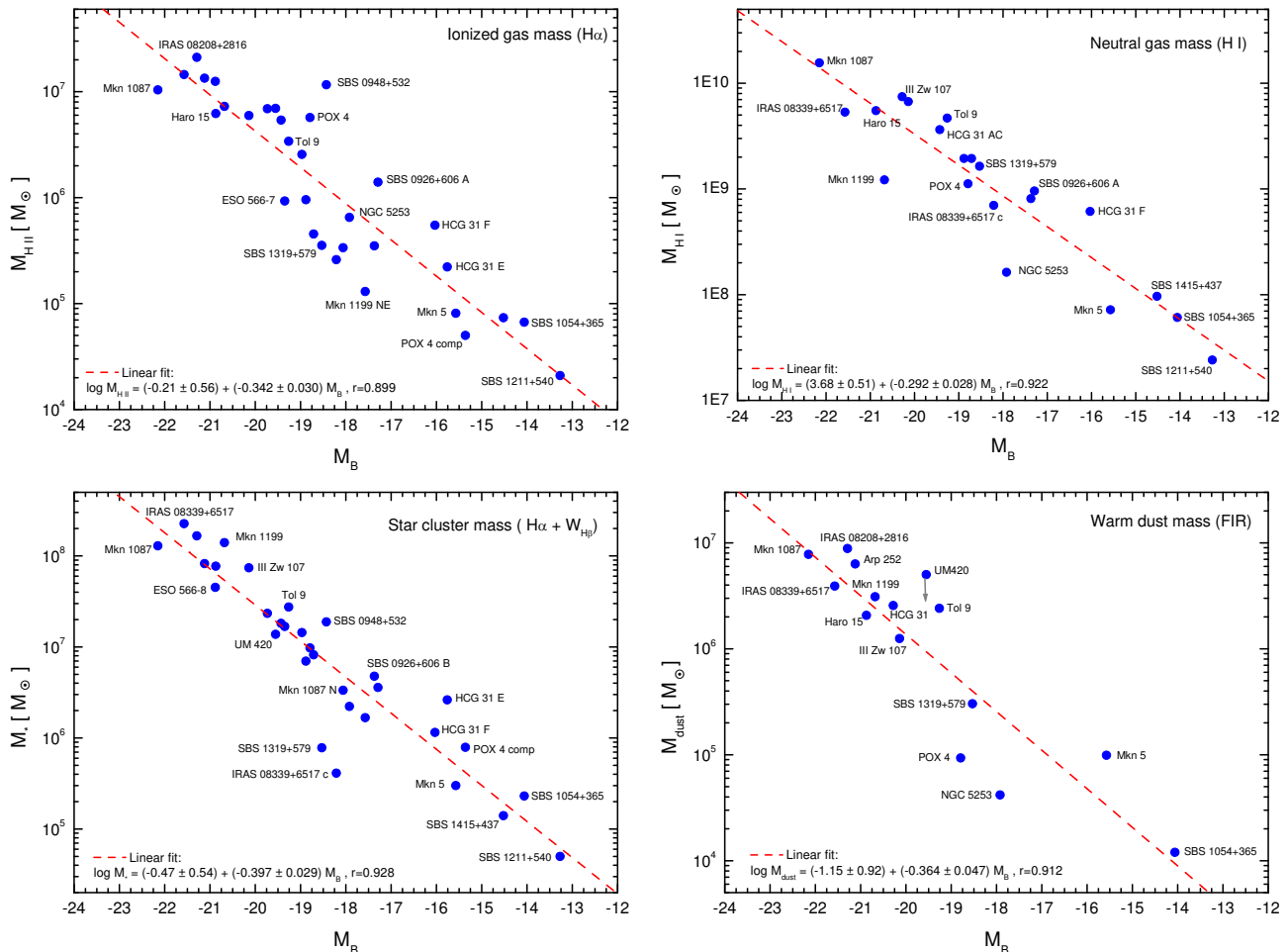


Fig. 9. Ionized gas mass (M_{HII}), neutral gas mass (M_{HI}), mass of the ionizing star cluster (M_*), and warm dust mass (M_{dust}) vs. the absolute B magnitude for the analyzed galaxies. Linear fits to the data are shown with a dashed red line.

rived stellar mass and the H I mass (we neglect the ionized gas, molecular gas, and dust contributions), the total baryonic mass, M_{bar} , can be computed via

$$M_{\text{bar}} = M_{\text{stars}} + 1.32M_{\text{HI}}, \quad (30)$$

where the factor 1.32 corrects the H I mass for the presence of helium. The derived values for both M_{bar} and M_{stars} are compiled in last columns in Table 7. For SBS 0948+532 and SBS 1211+540, that lack of NIR colors, we have assumed that $V - J \sim 0.8$ and $J - H \sim 0.3$ to derive the H -band luminosity.

As we should expect, the comparison between the dynamical and the baryonic masses (Figure 12) indicates that M_{dyn} is always larger than M_{bar} —except for IRAS 08339+6517, that has expelled a considerable fraction of its neutral gas to the intergalactic medium and shows a disturbed H I kinematics (Cannon et al. 2004) with a long tidal stream that makes impossible to get a good estimation of M_{dyn} (López-Sánchez, Esteban & García-Rojas 2006)—. Besides the uncertainties in M_{dyn} , this indicates the presence of dark matter in all systems. The dark matter contribution would be even higher if, as we said, our values of M_{dyn} are underestimated because of the uncertainty in the extension of the H I disk (in all cases, except in those galaxies for which interferometric data were available, we used the maximum of the radius of the optical extent to com-

pute M_{dyn}). The dotted yellow line in Fig 12 indicates the position of $M_{\text{dyn}} = M_{\text{bar}}$ if M_{dyn} is computed assuming that the extension of the neutral gas is 2.5 times the size of the optical extent. Indeed, only interferometric H I maps and a detailed analysis of the rotation of the neutral gas (i.e., de Blok et al. 2008; Westmeier et al. 2010) can provide a better estimation of the dynamical masses of galaxies. This issue is even more important if interactions are disturbing the rotation pattern of the H I gas. A clear example of this is Tol 9 within the Klemola 13 group. Our interferometric H I map (López-Sánchez et al. 2008b, 2010b) shows that the neutral gas cloud in which this BCG is embedded includes not only Tol 9 but also some nearby dwarf galaxies. Indeed, this H I cloud seems to rotate as a single entity, and shows a long tidal tail in direction to other galaxies of the group. However, the maximum of the H I emission is located exactly at Tol 9.

In any way, the important aspect to emphasize here is that, besides the unknown amount of dark matter, strongly interacting systems, as HCG 31 AC or Tol 1457-262, lie away from the observed main trend, having dynamical masses that are almost 14 and 7 times their baryonic masses. Mkn 1087, Mkn 1199 and Tol 9, that are in clear interaction with nearby objects, also have larger M_{dyn} than expected. Consequently, SBS 1054+365 and Mkn 5, that clearly have dynamical masses which are more than one

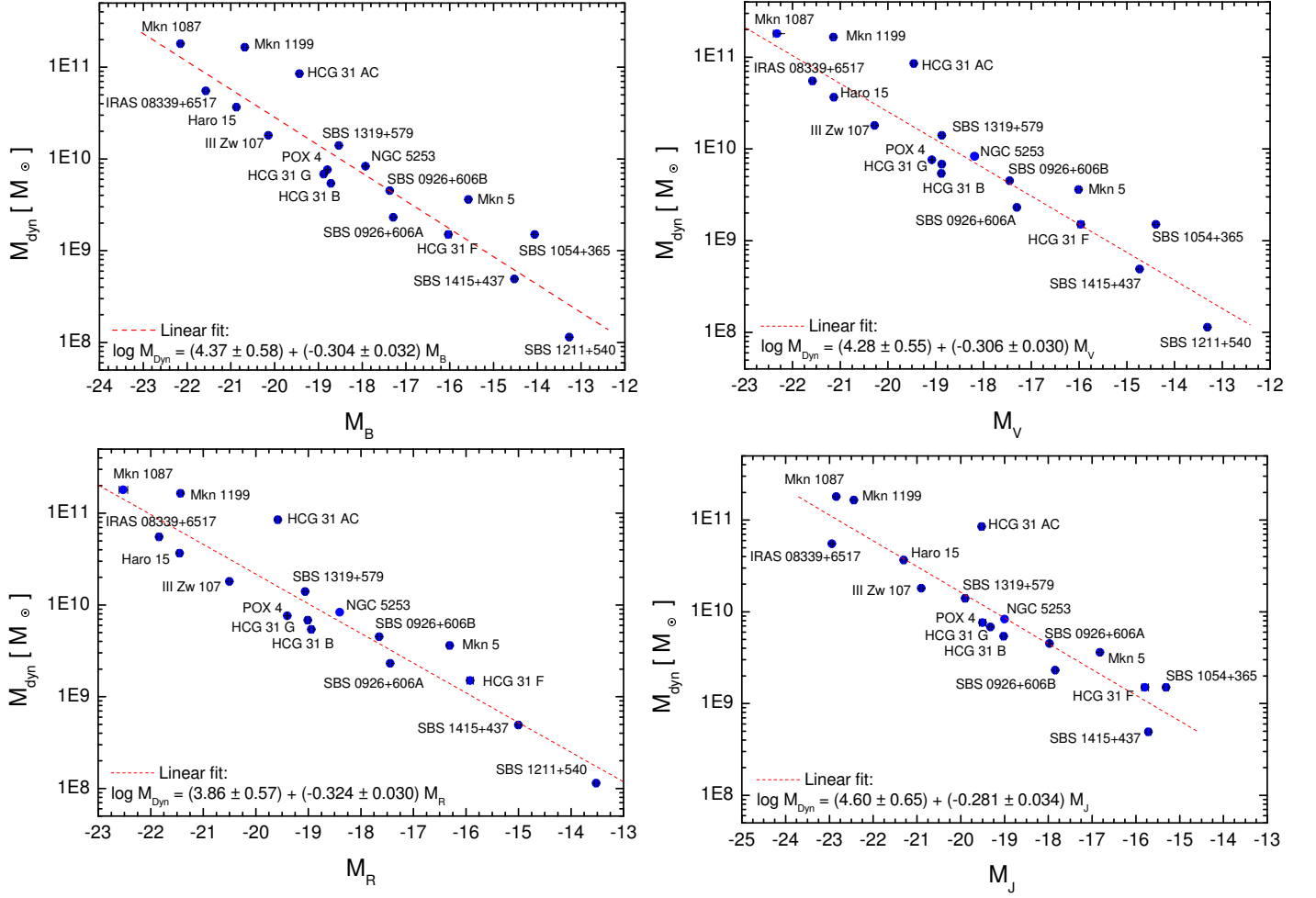


Fig. 10. Dynamical mass (M_{dyn}) vs. absolute B , V , R and J magnitudes for the galaxies analyzed in this work. A linear fit is shown with a dashed red line.

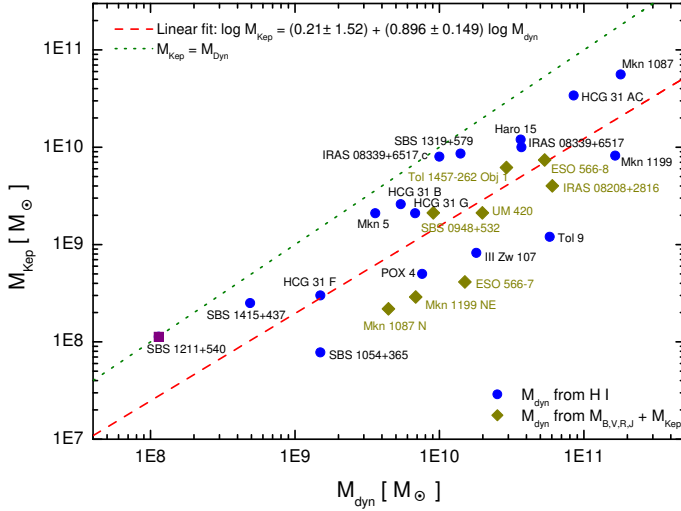


Fig. 11. Keplerian mass (M_{Kep}) vs. dynamical mass (M_{dyn}) for the galaxies studied in this work. Blue circles plot galaxies with a direct estimation of M_{dyn} using the HI data, while the dark yellow diamonds indicate when M_{dyn} was derived using Equations 25–28 and 29. The dashed red line is a linear fit to the M_{dyn} derived from the HI data excluding SBS 1211+540. The dotted green line indicates $M_{\text{Kep}}=M_{\text{dyn}}$.

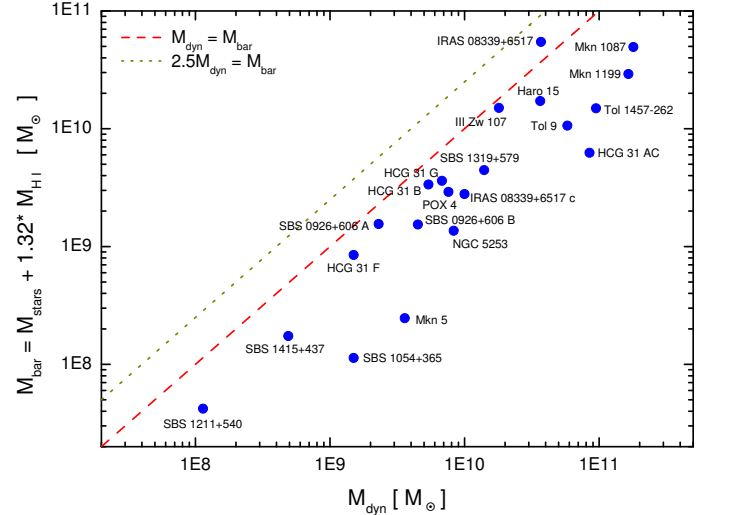


Fig. 12. Comparison between the baryonic mass (M_{bar}) and the dynamical mass (M_{dyn}) for our sample galaxies. The dashed red line indicates $M_{\text{bar}}=M_{\text{dyn}}$, the dotted yellow line indicates the position of $M_{\text{bar}}=M_{\text{dyn}}$ if M_{dyn} is computed assuming that the HI size of the galaxies is 2.5 their optical extend. Note that strongly interacting systems (HCG 31 AC or Tol 1457-262) lie away from the observed main trend.

order of magnitude higher than those expected for dwarf galaxies with $M_{\text{bar}} \sim 10^8 M_{\odot}$, may also have highly perturbed HI kinematics. The same situation may be happening in NGC 5253, which has a dynamical mass that is almost an order of magnitude higher than that expected for a galaxy with $M_{\text{bar}} \sim 10^9 M_{\odot}$.

6. Mass-metallicity relations

Our data set allows to investigate the mass-metallicity ($M - Z$) relation of star-forming galaxies. The relationship between metallicity and stellar mass provides key clues about galaxy formation and evolution; however commonly the luminosity is used instead of the mass to analyze such correlations (i.e., Paper IV and references within). Observationally, the $M - Z$ relation arises because low mass galaxies have larger gas fractions than higher mass galaxies (i.e., Boselli et al. 2001; Kewley & Ellison 2008). Theoretically, the mean stellar metallicity of the galaxies increases with age as a consequence of the chemical enrichment of the ISM, while the stellar mass increases with time as galaxies undergo merging processes (i.e. Somerville & Primack 1999; Calura, Matteucci & Menci 2004). Once the *NIR* luminosities or the optical-*NIR* SED are known, M_{stars} can be estimated relatively well using stellar evolutionary synthesis models, as we explained in the previous section. Hence, the main problem to study the $M - Z$ relation lies in all the uncertainties involving the determination of an accurate oxygen abundance, such as different methods yield to very different results (see Paper IV and Kewley & Ellison 2008). Here, the oxygen abundance of the majority of the galaxies was computed using the direct method, but Pilyugin (2001a) calibration has been applied to compute the metallicity of some few massive objects (Mkn 1087, Haro 15, IRAS 08339+6517, ESO 566-7, ESO 566-8), as we explained in Paper IV.

Figure 13 shows the relations between the stellar mass and the oxygen abundance, and Figure 14 shows the relations between the baryonic mass (left panel) and the dynamical mass (right panel) with the oxygen abundance. From Figures 13 and 14 is quite evident that a $M - Z$ relation is satisfied for our sample galaxies. Although there is still a considerable dispersion for some objects, the comparison with the luminosity-metallicity relation (see Fig. 17 and Sect. 5 of Paper IV) suggests a closest correlation when using the stellar, baryonic, or the dynamical masses than the absolute optical/*NIR* magnitudes.

The $M_{\text{stars}} - Z$ diagram (Fig. 13) shows a large dispersion for galaxies with $12 + \log(\text{O}/\text{H}) \sim 8$, as there are dwarf galaxies with $M_{\text{stars}} \sim 4 \times 10^7 M_{\odot}$ (HCG 31 F and E, SBS 1054+365) and large systems with $M_{\text{stars}} \sim 5 \times 10^9 M_{\odot}$ (UM 420, Tol 1457-262 Obj 1) within this metallicity range. The origin of this dispersion is that the low-mass systems are TDG candidates, that have higher oxygen abundance than that expected for their mass (this is not the case of SBS 1054+365), while the high-mass objects are very probably a merger of two independent galaxies (and hence their oxygen abundance is much lower than the expected for a single, more massive galaxy). Neglecting the TDG candidates and the galaxies in the processing of merging, a linear fit to the data yields to

$$x = (6.03 \pm 0.28) + (0.238 \pm 0.031) \log M_{\text{stars}}, \quad (31)$$

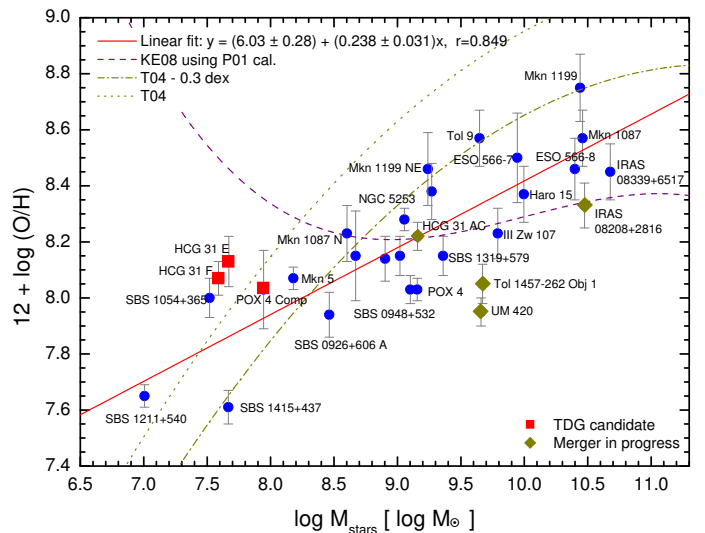


Fig. 13. Relation between M_{stars} and the oxygen abundance for our galaxy sample. A linear fit to the data is shown with a dashed red line. The TDG candidates are plotted with a red square, while galaxies in the process of merging are shown with a yellow diamond. A linear fit to the data without considering these two groups of objects is shown with a continuous red line. Some previous $M_{\text{stars}} - Z$ relations are also plotted: Tremonti et al. (2004) with a yellow dotted line, Tremonti et al. (2004) corrected by a factor of 0.3 dex in oxygen abundance –dotted-dashed yellow line–, and the Kewley & Ellison (2008) relation considering the Pilyugin (2001b) empirical calibration to derive the metallicity –dashed pink line–. These relations are only valid for $\log M_{\text{stars}} \geq 8.5$.

being $x = 12 + \log(\text{O}/\text{H})$. This relation has a correlation coefficient of $r = 0.849$ and it is plotted in Fig. 13 with a red continuous line. Our $M_{\text{stars}} - Z$ relation is quite different from previous relations given in the literature. For comparison, the $M_{\text{stars}} - Z$ diagram includes the relations provided by Tremonti et al. (2004) –dotted yellow line– and Kewley & Ellison (2008) using the Pilyugin (2001b) calibration to compute the oxygen abundance² –dashed pink line–. Tremonti et al. (2004) derived the oxygen abundances using theoretical photoionization models, that overestimate between 0.2 and 0.4 dex the metallicity derived from the direct T_e method (see Paper IV). Hence, we also plot in Fig. 13 the Tremonti et al. (2004) relation corrected by a factor of 0.3 dex in oxygen abundance (dotted-dashed yellow line). As we see, Tremonti et al. (2004) relation is steeper than that derived here, and does not agree well with our data. On the other hand, the Kewley & Ellison (2008) relation is quite flat in comparison with our observational data. These authors commented that for masses between 3×10^8 and $10^{11} M_{\odot}$, the metallicity of their sample galaxies rises only ~ 0.2 dex on average, but we find a variation of ~ 0.7 dex in the same mass interval.

Interestingly, Kewley & Ellison (2008) did not derive any $M_{\text{stars}} - Z$ relation using oxygen abundances determined with the T_e method, such as the SDSS catalog contains very few metal-poor and starbursting galaxies, and the scatter of the available data is huge. These authors finally concluded that the choice of the metallicity calibra-

² As we concluded in Paper IV, this calibration provides the best results to the oxygen abundances derived for our galaxies, that were mainly computed following the direct T_e method.

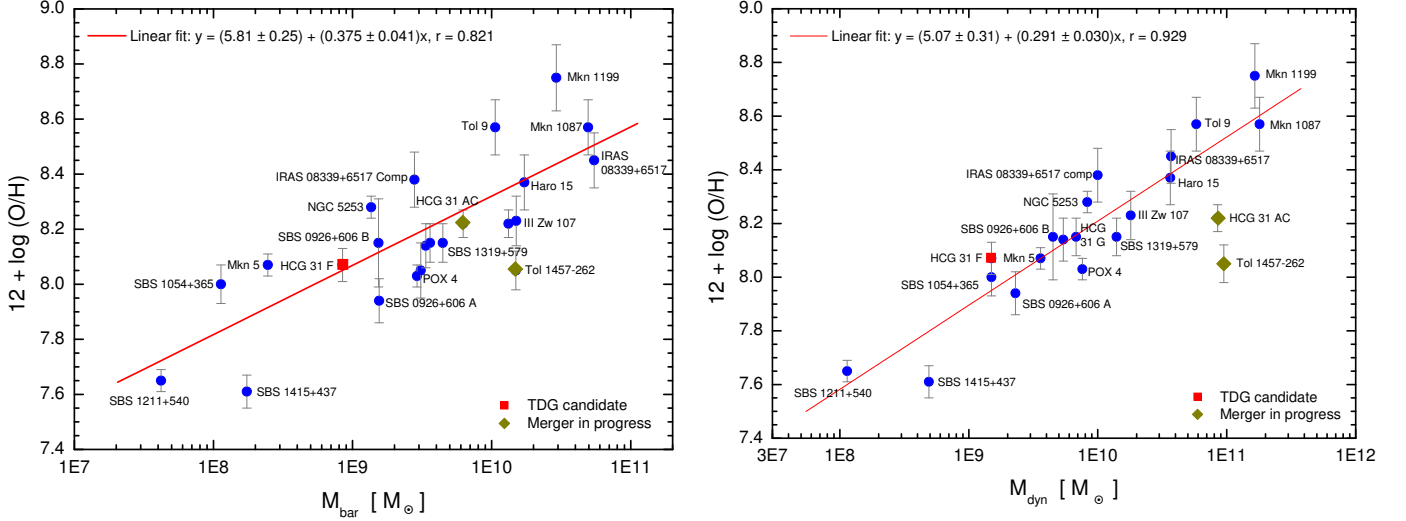


Fig. 14. Relation between M_{bar} (left panel) and M_{dyn} (right panel) with the oxygen abundance for our galaxy sample. The TDG candidate HCG 31 F is plotted with a red square, while HCG 31 AC and Tol 1457-262, that are galaxies in the process of merging, are shown with a yellow diamond. A linear fit to the data without considering these problematic objects is shown with a continuous red line in both diagrams.

tion has the strongest effect on the $M - Z$ relation, because a considerable variation in shapes and y -intercepts are found. Many of their fits suggested a flatter $M - Z$ relation at higher masses, something that was previously noticed by Tremonti et al. (2004). These authors explained this issue as a consequence of effective galactic winds that remove metals from the low-mass galaxies ($M \leq 10^{10.5} M_{\odot}$). Although our data do not allow to explore this issue at high masses, we do not see any trend of this effect.

It is very interesting to note that Tol 9, in which we detect a clear example of galactic wind, has a relatively low stellar mass for its expected metallicity. Probably that is indicating the strength and youth of the star-formation phenomena in this BCG. We should expect that the position of this object in the M_{stars} -O/H diagram will move to higher masses and lower metallicities if the star-formation processes continue and the fresh new material is expelled far from the galaxy via the effect of galactic winds.

The linear fits to the $M_{bar} - Z$ and $M_{dyn} - Z$ relations, that are plotted with red continuous lines in Figure 14 and do not consider TDG candidates and mergers in progress, are

$$x = (5.81 \pm 0.25) + (0.375 \pm 0.041) \log M_{bar}, \quad (32)$$

$$x = (5.07 \pm 0.31) + (0.291 \pm 0.030) \log M_{dyn}, \quad (33)$$

being $x=12+\log(\text{O}/\text{H})$. The correlation coefficients are $r = 0.821$ and $r = 0.929$ for the $M_{bar} - Z$ and $M_{dyn} - Z$ relations, respectively. The slopes of all the $M - Z$ relations agree relatively well. We note the tightness of the $M_{dyn} - Z$ relation: except the mergers in progress (HCG 31 AC and Tol 1457-262), all galaxies are found relatively close to the relation. This indicates that the dark matter content of the galaxies also increases with the metallicity, in agreement with the predictions of the evolutionary galaxy models.

In summary, the scatter observed in the luminosity-metallicity and in the mass-metallicity relationships of star-forming galaxies are consequence of both the nature and the star-formation histories experienced by these objects. Only a detailed analysis of each system can give the clues

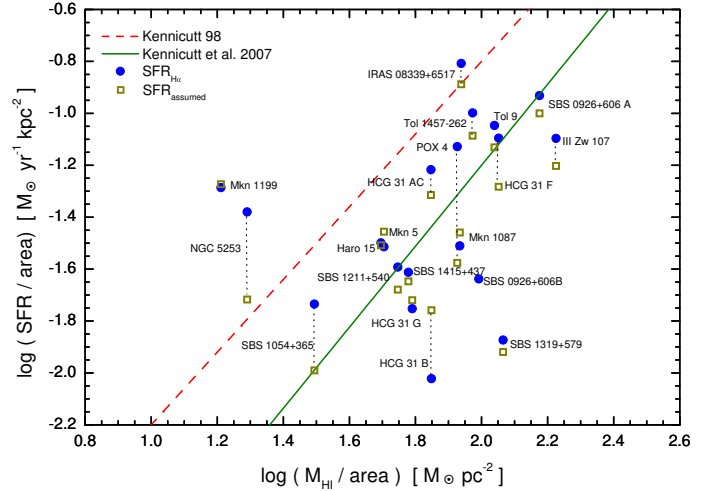


Fig. 15. Relation between the SFR/area and the H I gas density for our galaxy sample. We show two values per galaxy, one assuming the $\text{H}\alpha$ -based SFR following the Kennicutt (1998) calibration (blue circles) and other considering the SFR assumed combining all multi-wavelength data. The solid green line is the best fit to the M 51 data Kennicutt et al. (2007); the dashed red line is the relation for integrated values of star-forming galaxies derived by Kennicutt (1998).

needed to understand the evolution of the global properties in star-forming galaxies and their comparison between dwarf, normal and massive galaxies.

7. Schmidt-Kennicutt relation

We now investigate if the studied galaxies do obey the Schmidt-Kennicutt scaling laws of star formation. It is well known that there exist a tight correlation between the average SFR per unit area and the mean surface density of the cold gas on global galactic scales. Such correlation is usually parameterized via a power-law relation (Schmidt 1959, 1963; Kennicutt 1998; Kennicutt et al. 2007) that has

Table 8. Mass-to-light ratios of all mass estimations compiled in Table 7. The $M_{\text{bar}}/M_{\text{dyn}}$, $M_{\text{stars}}/M_{\text{bar}}$, $M_{\text{gas}}/M_{\text{bar}}$, $M_{\text{gas}}/M_{\text{stars}}$, and $M_{\text{dust}}/M_{\text{gas}}$ ratios are also listed in the last columns.

Galaxy	$\frac{M_{\text{HI}}}{L_B}$ [$\frac{M_\odot}{L_\odot}$]	$\frac{M_{\text{HII}}}{L_B}$ [$10^4 \frac{M_\odot}{L_\odot}$]	$\frac{M_{\text{dust}}}{L_B}$ [$10^4 \frac{M_\odot}{L_\odot}$]	$\frac{M_\star}{L_B}$ [$10^4 \frac{M_\odot}{L_\odot}$]	$\frac{M_{\text{Kep}}}{L_B}$ [$\frac{M_\odot}{L_\odot}$]	$\frac{M_{\text{dyn}}}{L_B}$ [$\frac{M_\odot}{L_\odot}$]	$\frac{M_{\text{stars}}}{L_B}$ [$\frac{M_\odot}{L_\odot}$]	$\frac{M_{\text{bar}}}{L_B}$ [$\frac{M_\odot}{L_\odot}$]	$\frac{M_{\text{bar}}}{M_{\text{dyn}}}$	$\frac{M_{\text{stars}}}{M_{\text{bar}}}$	$\frac{M_{\text{gas}}}{M_{\text{bar}}}$	$\frac{M_{\text{gas}}}{M_{\text{stars}}}$	$\frac{M_{\text{dust}}}{M_{\text{gas}}}$ [10^4]
HCG 31	0.369	3.86	1.27	18.7	0.167	0.655	...	0.255	0.744	2.91	2.60
" AC	0.395	5.86	...	19.8	3.7	9.23	0.156	0.678	0.073	0.231	0.769	3.34	...
" B	0.409	0.96	...	17.3	0.55	1.14	0.169	0.709	0.622	0.238	0.762	3.20	...
" E	...	7.09	...	83.7	...	4.15 ^a	0.150
" F	1.53	13.7	...	28.6	0.75	3.73	0.097	2.11	0.565	0.046	0.954	20.8	...
" G	0.350	1.72	...	12.6	0.38	1.23	0.189	0.651	0.531	0.290	0.710	2.44	...
Mkn 1087	0.138	0.92	0.69	11.4	0.50	1.60	0.256	0.438	0.274	0.583	0.417	0.715	3.78
" N	...	1.29	...	12.8	0.084	2.78	0.153
Haro 15	0.159	1.79	0.60	22.2	0.35	1.05	0.286	0.495	0.471	0.577	0.423	0.732	2.85
Mkn 1199	0.0419	2.49	1.07	48.0	0.28	5.67	0.945	1.00	0.177	0.945	0.055	0.059	19.2
" NE	...	0.78	...	10.1	0.17	4.22 ^a	1.05
Mkn 5	0.273	3.08	3.76	11.4	8.0	13.7	0.575	0.936	0.068	0.614	0.386	0.628	10.4
IRAS 08208+2816	...	4.14	1.73	32.5	0.076	1.18 ^a	0.585
IRAS 08339+6517	0.0805	2.19	0.59	34.2	0.151	0.56	0.720	0.827	1.48	0.871	0.129	0.148	5.57
" Comp	0.234	0.87	...	1.37	...	3.34	0.623	0.932	0.279	0.669	0.331	0.496	...
POX 4	0.219	11.2	0.183	19.1	0.098	1.49	0.281	0.570	0.383	0.492	0.508	1.03	0.63
" Comp	...	2.30	...	36.4	0.406
UM 420	...	6.76	4.9 ^b	13.4	0.204	1.94 ^a	0.444
SBS 0926+606	0.664	6.58	1.39	31.6	0.285	1.16	...	0.246	0.754	3.97	1.59
" A	0.746	10.9	...	28.0	...	1.79	0.226	1.21	0.676	0.187	0.813	4.35	...
" B	0.587	2.54	...	34.5	...	3.26	0.340	1.11	0.342	0.305	0.695	2.28	...
SBS 0948+532	...	31.7	...	51.4	0.57	2.46 ^a	0.345
SBS 1054+365	0.929	10.2	1.83	35.1	1.19	22.9	0.505	1.73	0.076	0.292	0.798	2.43	1.50
SBS 1211+540	0.762	6.61	...	15.8	3.57	3.61	0.321	1.33	0.368	0.242	0.758	3.13	...
SBS 1319+579	0.408	0.88	0.75	1.94	2.14	3.48	0.669	1.11	0.318	0.514	0.486	0.946	1.40
SBS 1415+437	0.964	7.35	...	14.0	2.50	4.90	0.465	1.74	0.355	0.268	0.732	2.74	...
III Zw 107	0.378	3.37	0.71	41.8	0.046	1.02	0.349	0.848	0.834	0.412	0.588	1.43	1.42
Tol 9 ^e	0.595	4.32	3.06	34.8	0.152	7.38	0.564	1.35	0.183	0.418	0.582	1.39	3.90
Tol 1457-262	0.258	5.17	1.01	22.5	...	5.22	0.479	0.820	0.157	0.584	0.416	0.711	2.95
" Obj 1	...	5.70	...	19.3	0.051	2.40 ^a	0.387
" Obj 2	...	4.25	...	23.9	...	2.49 ^a	0.601
Arp 252	...	3.01	1.45	18.9	0.775
" ESO 566-8	...	3.57	...	12.9	0.21	1.54 ^a	0.716
" ESO 566-7	...	1.09	...	19.6	0.047	1.75 ^a	1.03
NGC 5253	0.070	2.84	0.182	9.67	...	3.60	0.496	0.594	0.164	0.841	0.159	0.189	1.94

^a Using the tentative value of M_{dyn} computed using Eq 25.

proven to be very useful as an input scaling law for analytical and numerical models of galaxy evolution (e.g., Kay et al. 2002).

Figure 15 shows, on logarithm scale, the SFR per unit area versus the surface density of the HI gas ($M_{\text{HI}}/\text{area}$) for all the galaxies for which we have HI measurements. We plot two values for each galaxy, one assuming the H α -based SFR using Kennicutt (1998) calibration (blue circles) and other considering the SFR assumed combining all multi-wavelength data (last column in Table 5). Almost both values are quite similar in all galaxies except in some objects, remarkably POX 4 and NGC 5253. The majority of the galaxies are located close to the relation given by Kennicutt et al. (2007), which is the best fit to the data of star-forming regions within the nearby Sbc galaxy M 51. These authors also included the molecular gas to get this relation, but we have not considered it in our galaxy sample. The assumption of neglecting the molecular gas is valid in low-mass, low-metallicity galaxies, because of both the difficulty of detecting CO and the uncertainties of the correspondence between CO and H₂ in low-metallicity objects (i.e., Wilson 1995; Taylor, Kobulnicky & Skillman 1998; Braine et al. 2004). However, we should expect some

molecular gas contribution in more massive galaxies, as IRAS 08339+6517, Mkn 1087 and Mkn 1199.

From Fig. 15, it is evident that our data agree much better with the relation given by Kennicutt et al. (2007) than with the relation obtained by Kennicutt (1998) for star-forming galaxies (and not regions within galaxies). Interestingly, a recent study of the star-formation activity within UV-rich regions found in the outskirts of the galaxy pair NGC 1512/1510 (Koribalski & López-Sánchez 2009) yield to this same result. We note that we plot the H α -based SFR using the Kennicutt (1998) calibration because both Kennicutt (1998) and Kennicutt et al. (2007) relations use this calibration. In case of using the H α -based SFR derived from the Calzetti et al. (2007) calibration, the agreement of our data with the Kennicutt et al. (2007) relation will be even better. Some clear disagreements with the scaling laws of star formation are Mkn 1199 and NGC 5253 (both seem to be HI deficient; the molecular gas component in Mkn 1199 would not explain its position in the diagram, as it would require that $\sim 40\%$ of the total neutral hydrogen mass is H₂) and SBS 1319+579 (that show lower SFR than that predicted considering their HI gas amount). We then conclude that some external factors are indeed affecting the *normal* star-formation activity in these three galaxies.

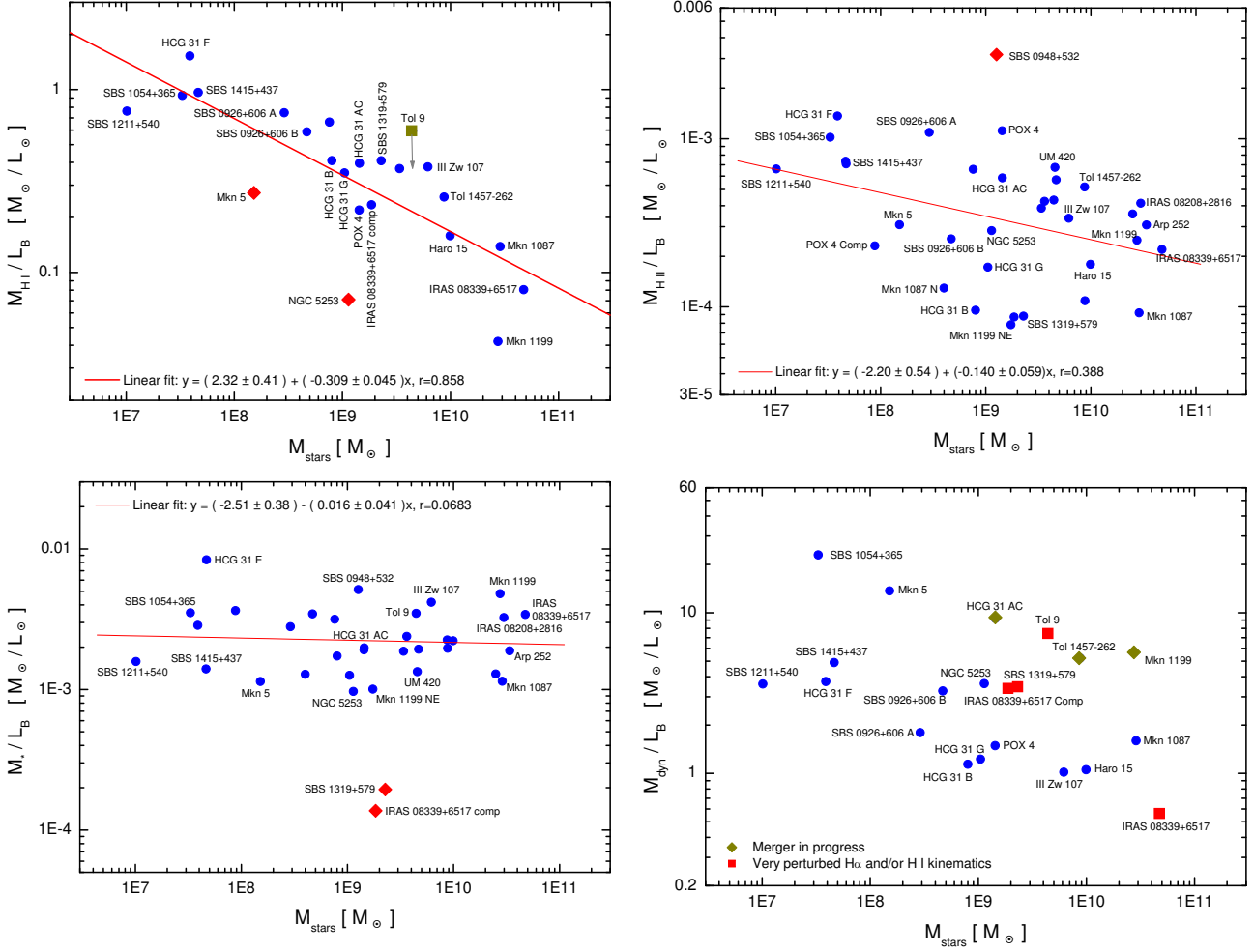


Fig. 16. Comparison between the stellar mass and some mass-to-light ratios for our sample galaxies.

8. Analysis of the mass-to-light ratios

Table 8 compiles all the mass-to- B luminosity ratios derived in this work. Some interesting relations are plotted in Figure 16, that compares some mass-to-light ratios with the stellar mass derived from the H -band luminosity.

The H I mass-to-light ratio of a galaxy is a distance-independent quantity that compares the H I mass with the luminosity in the B -band. This property correlates with many galaxy parameter, as the galaxy type, galaxy color or galaxy mass (Roberts & Haynes 1994). Indeed, the comparison of the M_{HI}/L_B ratio with the stellar mass in our sample galaxy clearly indicates that less massive galaxies have a higher mass fraction of neutral gas. The majority of the galaxies have a H I-mass-to-light ratio between 0.1 and 1.0, in agreement with previous estimations in star-forming dwarf galaxies (Salzer et al. 2002; Huchtmeier, Krishna & Petrosian 2005). We note some peculiar objects in this diagram. The H I-mass of Tol 9 has been overestimated because the H I cloud in which it is embedded includes several dwarf galaxies (López-Sánchez et al. 2008b, 2010b). On the other hand, two galaxies (Mkn 5 and NGC 5253) are very H I-deficient. In particular, NGC 5253 is very far from the typical position of the galaxies, showing a M_{HI}/L_B of $\sim 0.051 M_{\odot}/L_B$. The M_{HI}/L_B ratio of Mkn 1199 is also slightly low, even for a massive galaxy. As we already suggested (Sect. 3.4.3 of

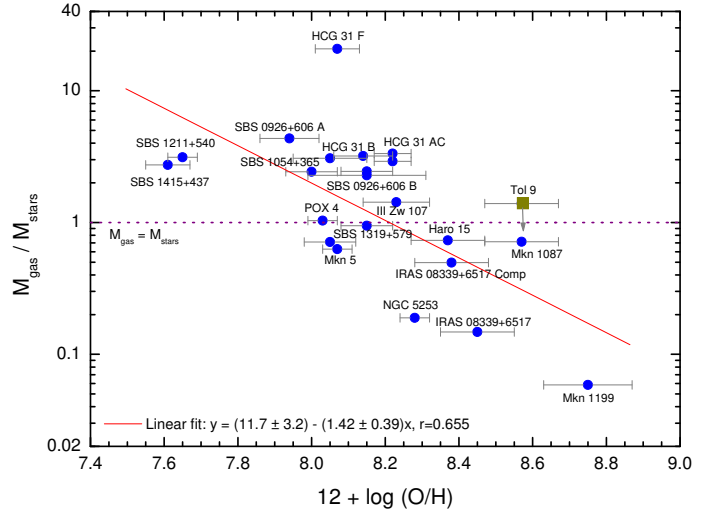


Fig. 17. Comparison of the $M_{\text{gas}}/M_{\text{stars}}$ ratio with the oxygen abundance for our sample galaxies. The dotted horizontal pink line indicates the position of $M_{\text{gas}} = M_{\text{stars}}$. The red continuous line is a linear fit to the data, neglecting Tol 9, for which the neutral gas mass corresponds to this object and some dwarf surrounding galaxies (see text and LS08).

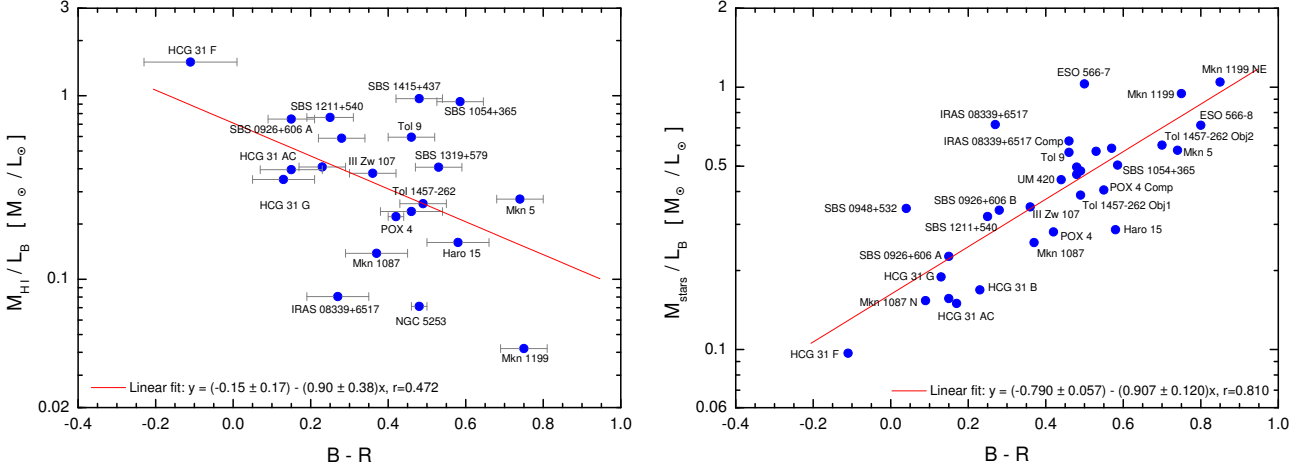


Fig. 18. Relation between the M_{HI}/L_B ratio (left panel) and the M_{stars}/L_B ratio (right panel) with the $B - R$ color for our sample galaxies. Linear fits are plotted with a continuous red line. Some objects have been labeled.

Paper II), Mkn 1199 may have lost part of its neutral gas in the interaction process with its NE companion. Neglecting the contribution of Tol 9, Mkn 5 and NGC 5253, a linear fit provides the empirical relation

$$\log \frac{M_{\text{HI}}}{L_B} = (2.32 \pm 0.41) - (0.309 \pm 0.045) \log M_{\text{stars}}, \quad (34)$$

that has a correlation coefficient of $r = 0.858$.

We do not find any high M_{HI}/L_B ratio ($> 1M_{\odot}/L_B$) in our sample galaxy, except in the case of the TDG candidate HCG 31 F, that has $1.53 M_{\odot}/L_B$. High H I mass-to-light ratios have been reported in some few galaxies. The detailed analysis of the gas-rich low surface brightness dwarf irregular galaxy ESO 215-G009 performed by Warren, Jerjen & Koribalski (2004) confirmed an extremely high M_{HI}/L_B of $22 \pm 4 M_{\odot}/L_B$ in this galaxy, for which the H I disk extends 6.4 ± 0.4 times the Holmberg radius. They concluded that ESO 215-G009, that is very isolated (no neighbors identified out to 1 Mpc), has a low SFR that probably remained unchanged throughout the galaxy's existence. In a subsequent paper (Warren, Jerjen & Koribalski 2006) these authors suggested that high M_{HI}/L_B galaxies are not lacking the baryons to create stars, but are underluminous as they lack either the internal or external stimulation for more extensive star formation.

Warren, Jerjen & Koribalski (2007) derived an empirical upper envelope for M_{HI}/L_B as a function of the absolute B -magnitude, that accounts for the maximum amount of atomic hydrogen gas a galaxy of a particular luminosity can retain in the Universe today. All our sample galaxies satisfy this empirical relation.

The derived M_{HII}/L_B ratios for our galaxy sample lie in the range 10^{-3} – $10^{-4} M_{\odot}/L_B$. Although the scatter of our data is high (a tentative linear fit gives a very low correlation coefficient), they indicate that the M_{HII}/L_B ratio slightly decreases with increasing stellar mass, suggesting that the ionized gas to stars ratio is higher in dwarf galaxies. SBS 0948+532 is away from the rest of the objects because of its very high H α flux (see Sect. 3.11 in Paper I). On the other hand, the ionizing star cluster mass-to-light ratio, M_{\star}/L_B , seems to be rather constant with the stellar mass, showing an average value of $\sim 0.0022 M_{\odot}/L_B$.

Two galaxies, SBS 1319+579 and the companion object of IRAS 08339+6517 lie apart from this tendency, as we also saw in Fig. 9.

The M_{dyn}/L_B ratio seems to slightly decrease with the stellar mass. However, the analysis of this diagram is difficult, because interactions notably modify the estimation of the dynamical mass. Usually, perturbed kinematics yield to higher M_{dyn} (HCG 31 AC, Mkn 1199, Tol 1457-262, Tol 9), but sometimes the existence of tidal tails with a rather constant velocity give a lower M_{dyn} than the real one (IRAS 08339+6517). SBS 1319+579 (a probable merging of two dwarf objects) and IRAS 08339+6517 Comp (in interaction with the main galaxy of the system) also show somewhat high M_{dyn}/L_B ratios. Hence, we may suggest that galaxies Mkn 5 and SBS 1054+365, that lie far from the rest of the objects, have a perturbed kinematics, being M_{dyn} overestimated in both cases.

Figure 17 compares the ratio between the gas and the stellar masses with the oxygen abundance. Clearly, $M_{\text{gas}}/M_{\text{stars}}$ decreases with increasing metallicity, indicating that the importance of the stellar component to the total mass is higher in more massive galaxies. We should expect this result, which is qualitatively the inverse behavior of the M_{HI}/L_B ratio with the stellar mass. A tentative linear fit to the data (excluding Tol 9) is plotted in Fig. 17) with a continuous red line, and provides

$$\log \frac{M_{\text{gas}}}{M_{\text{stars}}} = (11.7 \pm 3.2) - (1.42 \pm 0.39)x, \quad (35)$$

being $x = 12 + \log(\text{O}/\text{H})$, and has a correlation coefficient of $r = 0.655$. Following this analysis, we should expect that galaxies with $12 + \log(\text{O}/\text{H}) \sim 8.2$ – 8.3 have relatively equal gas and stellar masses. HCG 31 F is the galaxy with highest $M_{\text{gas}}/M_{\text{stars}}$ ratio (and lowest M_{stars}/L_B ratio), indicating its low content of evolved stars. This result agrees with our suggestion (López-Sánchez et al. 2004a) that this TDG has created stars mainly using the neutral gas from the long arm-like H I structure (Verdes-Montenegro et al. 2005) found between members AC and G of the HCG 31 galaxy system.

Finally, we compare some mass-to-light ratios with the colours of the galaxies. Amorín et al. (2009) reported that the underlying component (host) of blue compact galax-

ies is redder with decreasing M_{HI}/L_B . We do not find any correlation between the M_{HI}/L_B ratio and the optical colors of the underlying component, but we did not perform a detailed analysis of the structural parameters of the host underlying the starburst as Amorín et al. (2009) did. The comparison of the global $B - R$ colour and the neutral gas mass-to-light ratio is shown in the left panel of Fig 18, and has a huge scatter. We should remember that Mkn 1199, Mkn 5 and NGC 5253 seem to be HI deficient, and that IRAS 08339+6517 is a luminous blue compact galaxy (López-Sánchez et al. 2006), and hence their real positions in this diagram is uncertain. Although a tentative fit to the data suggests that galaxies with redder $B - V$ colours have lower M_{HI}/L_B ratios, the huge scatter does not allow us to confirm such tendency.

However, we do observe a clear relation between the stellar-to-light ratio and the global $B - R$ colour of the galaxies (right panel of Fig. 18). This tendency seems to be also a consequence of the building of the galaxies, as more massive galaxies have experienced more star-formation events than less massive objects, and hence tend to show redder stellar populations than dwarf galaxies. This result also agrees quite well with the observed tendencies that M_{HI}/L_B ratio decreases with the stellar mass and that $M_{\text{gas}}/M_{\text{stars}}$ ratio decreases with increasing metallicity.

9. Dust properties in star-forming galaxies

Our data set allows us to investigate the properties and effects of the dust content in low-metallicity star-forming galaxies. Figure 19 plots the reddening coefficient, $c(\text{H}\beta)$ –obtained using our optical spectra–, as a function of the warm dust mass, M_{dust} –derived from *FIR* data–. Neglecting the data for UM 420 (as we said before, M_{dust} is overestimated because of the *FIR* contribution of the foreground galaxy UGC 01809), we see a clear correlation between both quantities: galaxies with higher amount of warm dust (and hence, as we saw in Figure 9, higher luminosity) show higher extinction. This conclusion is in agreement with other results previously found in this work, as the correlation between $c(\text{H}\beta)$ and the oxygen abundance discussed in Paper IV. More important, this result indicates that most of the dust is internal to the galaxy and not in the line of sight. Detailed analysis of the dust distribution within nearby galaxies (i.e. Muñoz-Mateos et al. 2009) found clear relationships between the dust content and general properties of nearby spiral galaxies, such as galaxy type, luminosity, and metallicity. Here we confirm in an independent way, such as the extinction was derived from our optical spectra, that the dust content and therefore the extinction in dwarf galaxies depends on their metallicities and luminosities, and very probably also on their star-formation histories. A proper estimation of the amount of dust within such objects is needed to perform appropriate statistical analysis involving larger galaxy samples.

We now investigate the dust-to-gas ratio, $M_{\text{dust}}/M_{\text{gas}}$, of our sample galaxies, a very important quantity when studying the chemical enrichment of the ISM, as it accounts for the amount of metals locked up onto dust grains through the stellar yields. The existence of a correlation between the $M_{\text{dust}}/M_{\text{gas}}$ and the oxygen abundance has been reported in many studies (i.e., Lisenfeld & Ferrara 1998; James et al. 2002; Draine et al. 2007; Muñoz-Mateos et al. 2009). Figure 20 shows the dust-to-gas ratio as a function of the

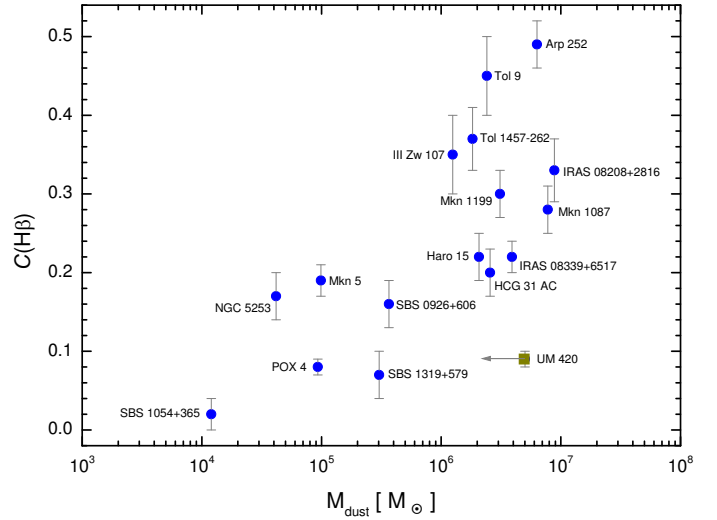


Fig. 19. Reddening coefficient, $c(\text{H}\beta)$, vs. warm dust mass, M_{dust} . We note that the M_{dust} value in UM 420 is overestimated because of the *FIR* contribution of UGC 01809.

oxygen abundance. The gas mass was computed assuming only the HI and the HeI gas, but not the contribution of the molecular gas, that as we already explained is not important in dwarf low-metallicity objects. The derived dust-to-gas ratio of each galaxy for which we have both HI and *FIR* data are compiled in the last column of Table 8. From Figure 20, it is evident that objects with higher metallicities tend to have higher $M_{\text{dust}}/M_{\text{gas}}$ ratios, such as the amount of dust increases while the neutral gas is consumed as the galaxies experience new star-formation phenomena. The linear fit to our data (continuous red line in Fig. 20) provides this tentative relation

$$\log(M_{\text{dust}}/M_{\text{gas}}) = (-12.0 \pm 2.9) + (1.02 \pm 0.36)x, \quad (36)$$

with $x=12+\log(\text{O}/\text{H})$ and correlation coefficient of $r = 0.637$. Mkn 5 lies far the the majority of the points, but as we already commented this object seem to be very deficient in HI, so we did not include this point in the fit. Although with higher uncertainties, we also observe that more massive objects also tend to have higher $M_{\text{dust}}/M_{\text{gas}}$ ratios.

Draine et al. (2007) provided a relation between $M_{\text{dust}}/M_{\text{gas}}$ and the oxygen abundance –computed following the Pilyugin & Thuan (2005) calibration– in a sample of spiral and irregular galaxies, that we may re-write as

$$\log(M_{\text{dust}}/M_{\text{gas}}) = 6.48 + x, \quad (37)$$

being $x=12+\log(\text{O}/\text{H})$, and plotted in Figure 20 with a dotted pink line. The factor 6.48 was derived from $\log[(M_{\text{dust}}/M_{\text{gas}})_{\text{MW}}/1.32] + x_{\text{MW}}$ assuming $(M_{\text{dust}}/M_{\text{gas}})_{\text{MW}} = 0.010$ and $x_{\text{MW}} = 8.6$ for the Milky Way. As we see, this relation lies away from our data, although the slope is the same in both cases. Draine et al. (2007) also found that the global dust-to-gas ratio of all their galaxies with $12+\log(\text{O}/\text{H}) < 8.1$ falls below this equation, sometimes by a factor larger than 10. The dashed-dotted green line in Figure 20 plots the Draine et al. (2007) relation divided by a factor 10. As we can see, this relation agrees better with our data. Draine et al. (2007) also remarked that many of the low-metallicity galaxies have large HI envelopes mainly

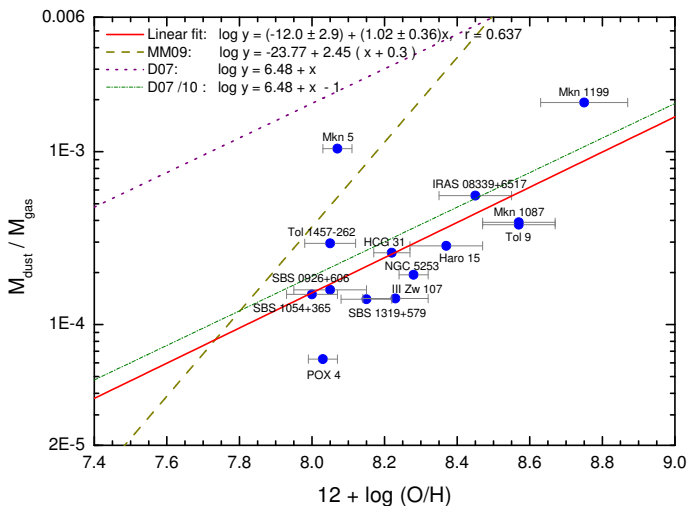


Fig. 20. Dust-to-gas ratio, M_{dust}/M_{gas} , vs. the oxygen abundance for our sample galaxies. The red continuous line is a fit to our data (neglecting Mkn 5). The dashed yellow line indicates the relation found by Muñoz-Mateos et al. (2009) analyzing the radial dust-to-gas profiles for a larger sample of spiral galaxies. This relation has been corrected by 0.3 dex because it was derived assuming the Kobulnicky & Kewley (2004) calibration to compute the oxygen abundances, that overestimates in 0.2–0.4 dex the oxygen abundance provided by the direct T_e method. The dotted pink line is the relation provided by Draine et al. (2007) in their analysis of a sample of spiral and irregular galaxies. The dashed-dotted green line indicates the Draine et al. (2007) relation divided by a factor 10.

composed by un-enriched material. However, the metallicity is derived from the brightest H II regions, that usually show the highest metallicities (most recent star formation) within the system. Consequently, the derived M_{dust}/M_{gas} ratio should correspond to lower oxygen abundances.

Recently, Muñoz-Mateos et al. (2009) analyzed the radial dust-to-gas profiles for a larger sample of spiral galaxies and found a steeper relation between M_{dust}/M_{gas} and the metallicity, that they explained because the outskirts of spiral galaxies seem to have a much lower M_{dust}/M_{gas} than the central regions (see their figure 16). These authors suggested a link with the behavior found in dwarf galaxies because in the external regions of the spiral galaxies the neutral gas has not yet undergone star-formation activity. However, this trend could also be a consequence of the radial decrease of the star-formation efficiency found in nearby spirals (i.e., Thilker et al. 2007; Leroy et al. 2008).

We may check these hypotheses comparing our data with the relation provided by Muñoz-Mateos et al. (2009). However, we should modify slightly their equation, because these authors used the Kobulnicky & Kewley (2004) method to derive the metallicities, and this calibration overestimates the oxygen abundances provided by the direct T_e method in 0.2–0.4 dex (see Paper IV). The modified relation that is plotted with a dashed yellow line in Figure 20 is

$$\log(M_{dust}/M_{gas}) = -23.77 + 2.45(x + 0.3), \quad (38)$$

being $x=12+\log(\text{O}/\text{H})$. We see that except for Mkn 5 all our data have lower M_{dust}/M_{gas} ratios than those predicted following this relation. Hence, we suggest that the low M_{dust}/M_{gas} ratios found in dwarf low-metallicity galaxies is a consequence of the large reserves of un-enriched

neutral gas in these systems, while the low M_{dust}/M_{gas} ratios reported by Muñoz-Mateos et al. (2009) in the external regions of spiral galaxies are due to the decreasing of the star-formation efficiency in those areas. Indeed, the outskirts of spiral galaxies seem to show lower H I surface densities $-\log(M_{\text{H}}/\text{area}) \sim 0.4\text{--}0.8 M_{\odot} \text{pc}^{-2}$ for external regions of M 51 (Kennicutt et al. 2007) and NGC 1512 (Koribalski & López-Sánchez 2009)– than the neutral gas envelopes of dwarf galaxies $-\log(M_{\text{H}}/\text{area}) \sim 1.4\text{--}2.0 M_{\odot} \text{pc}^{-2}$ following Fig. 15–, that is translated in a decreasing of the star-formation activity following the Schmidt-Kennicutt law. However, more high-quality data and a detailed analysis of the dust and the H I distribution in nearby dwarf galaxies should be performed to confirm all these issues.

10. Comparison with the closed-box model

To study the environment effects of the gas content and the chemical enrichment in galaxies, it is common to compare with the so-called *closed-box chemical evolution* model (Schmidt 1963; Searle & Sargent 1972; Edmunds 1990). According to this model, a galaxy consists initially of gas with no stars and no metals. The stellar IMF is assumed to be constant on time. Stars that end their life as supernovae are assumed to enrich the ISM with metals immediately. Throughout its life, the galaxy experiences instantaneous recycling and the products of stellar nucleosynthesis are neither diluted by infalling pristine gas nor lost via outflow of enriched gas. Hence, the metallicity at any given time is only determined by the fraction of baryons which remains in gaseous form. The model can be written as

$$Z_{\text{O}} = y_{\text{O}} \ln(1/\mu), \quad (39)$$

where Z_{O} is the oxygen mass fraction, y_{O} is the yield by mass and μ is the ratio of the gas mass to the baryonic mass, $\mu = M_{\text{gas}}/M_{\text{bar}}$. The gas mass corresponds to the hydrogen atomic gas with a correction for neutral helium, but it does not include molecular gas ($M_{\text{gas}}=1.32M_{\text{HI}}$) that, as we already said, can be neglected in low-metallicity galaxies.

Left panel of Figure 21 compares the observed oxygen abundances to those predicted by closed-box models, that are plotted with lines with different y_{O} . The green continuous line indicates the model with $y_{\text{O}}=0.0074$, that is the theoretical yield of oxygen expected for stars with rotation following Meynet & Maeder (2002) models (van Zee & Haynes 2006). As we can see, the majority of the galaxies show oxygen abundances lower than the expected by the closed-box models. The yield of oxygen that best fits our data (the *effective yield*) is $y_{\text{O}}=0.003\text{--}0.005$, in agreement with previous results found in the literature (i.e., Lee et al. 2003; van Zee & Haynes 06; Lee, Zucker & Grebel 2007). Hence, the sample galaxies are generally not well reproduced by the simple closed box model, and therefore inflow of pristine gas or outflow of enriched gas have played an important role in their chemical evolution.

Interestingly, there is a galaxy that appears far away from the predictions given by the theoretical closed box model, but in the opposite direction to the rest of the galaxies. Indeed, HCG 31 F shows a much *higher* oxygen abundance than that expected following the closed box model. The explanation of this behavior is that this object is a TDG that was very probably formed from

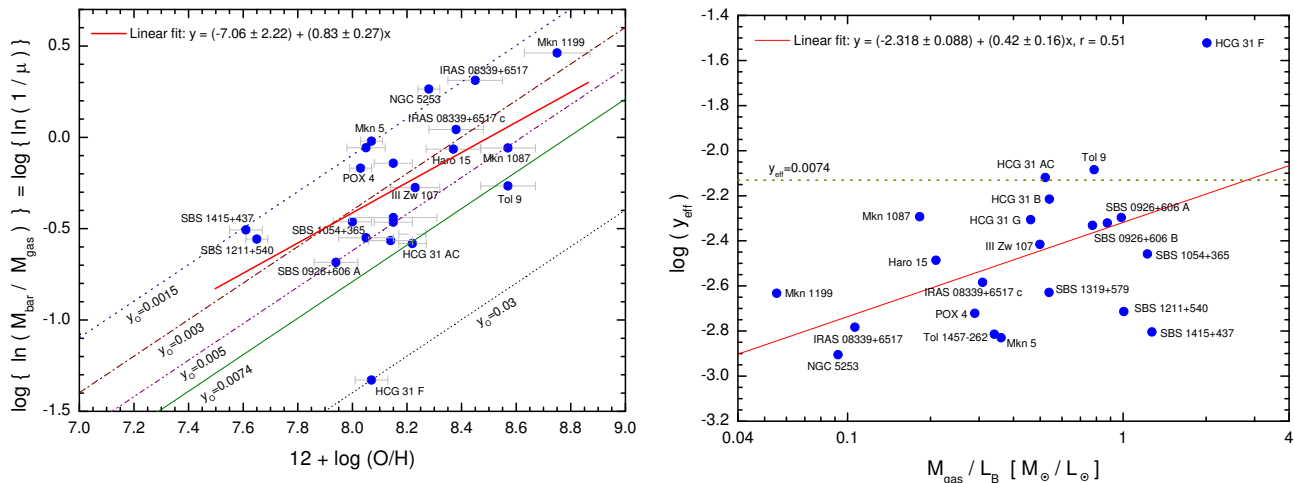


Fig. 21. (Left panel) Comparison of the observed oxygen abundance and that predicted by simple closed-box chemical evolution models with instantaneous recycling and constant star-formation rates. The continuous green line indicates the expected trend if the galaxies are closed boxes with an oxygen yield $y_{\text{O}}=0.0074$ (Meynet & Maeder 2002; van Zee & Haynes 2006). Closed-box models with $y_{\text{O}}=0.0015$, 0.003, 0.005, and 0.03 are also plotted. A linear fit to our data is shown with a continuous red line, and indicates an oxygen yield of $y_{\text{O}}=0.003$ –0.005. (Right panel) Effective yield plotted as a function of the M_{gas}/L_B ratio. The closed-box yield is plotted by a dotted yellow line. A linear fit to the data is shown with a continuous red line.

the material stripped from HCG 31 AC during the fly-by encounter between member G and the A+C complex (López-Sánchez et al. 2004a). The TDG has accreted a large fraction of the pre-enriched HI gas available in the arm-like structure and now hosts a very intense star-formation activity.

Finally, the comparison of the effective yield derived in each object with some global galaxy parameters (dynamical and baryonic mass, absolute magnitude, gas mass-to-luminosity ratio, and surface star formation rate) does not show any clear trend. This result is almost the same than that observed by van Zee & Haynes (2006) in the analysis of a sample of isolated dwarf irregular galaxies. The difference is that these authors reported a strong correlation with the gas mass-to-luminosity ratio, that they explained in the sense that gas-rich galaxies are more likely to be closed boxes. But, as we see in the right panel of Figure 21, such tight correlation is not satisfied by our data, although we do observe the trend that galaxies with higher M_{gas}/L_B ratios have lower effective yields (a linear fit to our data is shown with a continuous red line). Therefore, for intense star-forming and gas-rich galaxies, the closed box model is also not valid. We then conclude that environment effects are playing a crucial role in the evolution of these galaxies.

11. Quantification of the interaction features

Throughout this paper series we have compiled new evidences of the interaction-induced star-formation activity in starburst galaxies, in particular in dwarf galaxies. Alternative mechanisms, as the Stochastic Self-Propagating Star Formation (Gerola, Seiden, & Schulman 1980) model (that assumes statistical fluctuations of SFR), or the ideas of the cyclic gas re-processing of the ISM (Davé & Oppenheimer 1988) or gas compression by shocks due to the mass lost by galactic winds followed by the cooling of the ISM (Thuan 1991; Hirashita 2000), fail to explain some observational characteristics and the triggering mechanism of dwarf starburst galaxies (i.e., García-Lorenzo et

al. 2008; Cairós et al. 2009). In the previous section, we demonstrated that the closed-box model is not valid to explain the chemical evolution experienced by our sample of galaxies, emphasizing the idea that environment effects are needed to understand their observed properties. Indeed, the interaction/merger scenario explains, in a natural way, the starburst activity in these objects just as a consequence of the evolution of the galaxies throughout the cosmic time following hierarchical formation models (Kauffmann & White 1993; Kauffmann et al. 1997; Springel et al. 2005). These models predict that most galaxies have formed by merging of small clouds of protogalactic gas and that galaxy interactions between dwarf objects were very common at high redshifts.

However, the interaction features in dwarf objects are, in many cases, not evident because of the lack of deep and high-resolution images and spectra (Méndez & Esteban 2000) and detailed multi-wavelength analyses. Now it is well known that interactions in dwarf galaxies are not usual with nearby giant galaxies (Campos-Aguilar, Moles & Masegosa 1993; Telles & Terlevich 1995; Telles & Maddox 2000) but with low surface brightness galaxies (Wilcots, Lehman & Miller 1996; Noeske et al. 2001; Pustilnik et al. 2001), or HI clouds (e.g., Taylor et al. 1993, 1995, 1996; Thuan et al. 1999; van Zee, Salzer & Skillman 2001; Begum et al. 2006; Ekta, Chengalur & Pustilnik 2006; Hutchmeier et al. 2008; López-Sánchez & Esteban 2008). Méndez & Esteban (2000) suggested, for the first time, that interactions with or between dwarf objects could be the main star formation triggering mechanism in dwarf galaxies. Later, Östlin et al. (2001) and Bergvall & Östlin (2002) suggested that a merger between two galaxies with different metallicities or infall of intergalactic clouds could very probably explain the starburst activity in the most luminous BCDGs. Since then, studies focused on individual objects have also shown that interactions do play a decisive role in the evolution of these systems (Johnson et al.

Table 9. Interaction features in our WR galaxy sample.

Galaxy	Morphological features				Kinematics feat.		Differ. in abundances	M/L_B ratios	Other features	INTERACTION DEGREE
	Plume	Tail	Merger	TDGs	H II gas	H I gas				
HCG 31 AC ^a	X	X	X	X	X	X	X	X	X	VERY HIGH
Mkn 1087	–	X	–	X	X	...	X	–	–	HIGH
Haro 15	?	–	X	?	X	...	X	–	–	VERY HIGH
Mkn 1199 ^a	X	–	X	–	X	...	X	X	X	VERY HIGH
Mkn 5	–	–	–	–	–	...	?	X	X	LOW
IRAS 08208+2816	–	X	?	?	X	...	X	–	–	VERY HIGH
IRAS 08339+6517 ^a	X	–	–	?	X	X	–	–	–	HIGH
POX 4	X	–	–	?	X	X	–	–	X	HIGH
UM 420	–	X	?	–	?	...	–	–	–	VERY HIGH
SBS 0926+606 A	X	–	X	–	X	...	–	–	–	VERY HIGH
SBS 0926+606 B	X	X	–	?	X	...	–	–	–	HIGH
SBS 0948+532	–	X	–	–	?	...	–	X	–	PROBABLE
SBS 1054+365	–	–	–	?	X	...	–	X	X	LOW
SBS 1211+540	X	–	?	–	X	...	–	–	–	PROBABLE
SBS 1319+579	–	–	?	–	X	...	?	X	X	PROBABLE
SBS 1415+437	–	–	–	–	?	...	–	–	–	LOW
III Zw 107	X	–	?	–	X	...	?	X	–	HIGH
Tol 9	X	–	–	–	X	X	–	X	X	HIGH
Tol 1457-262	X	–	X	X	X	...	X	–	–	VERY HIGH
Arp 252 ^a	X	X	–	X	X	...	X	–	–	VERY HIGH
NGC 5253	–	–	–	–	X	X	X	X	X	PROBABLE ^b

^a Some interaction features in this galaxy were previously reported by other authors.

^b The chemical differences and the kinematics features can be explained by other reasons. See López-Sánchez et al. (2007) and López-Sánchez et al. (2010a).

2004; Bravo-Alfaro et al. 2004, 2006; Cumming et al. 2008; García-Lorenzo et al. 2008; James et al. 2009, 2010).

Our exhaustive multi-wavelength analysis of starburst galaxies combining broad-band optical/*NIR* and $H\alpha$ photometry, optical spectroscopy, and X-ray, *UV*, *FIR*, 21-cm H I line, and 1.4 GHz radio-continuum data compiled from the literature allows us to perform a quantitative analysis of the interaction features detected in each object. A summary of the results found in each individual system of our WR galaxy sample is presented in Appendix A. To quantify the interaction features, we compile in Table 9 some interaction indicators classified in several categories, that we describe below.

1. Morphological features, as the detection of faint plumes or bridges (Haro 15, IRAS 08339+6517, SBS 0926+606 B, SBS 1211+540, III Zw 107, Tol 9, Tol 1457-262, Arp 252), prominent tails (HCG 31, Mkn 1087, IRAS 08208+2816, UM 420, SBS 0948+532, Arp 252), disturbed morphology (HCG 31, POX 4, Tol 1457-262), TDGs candidates (HCG 31, Mkn 1087, SBS 0926+606 B, Arp 252) or mergers.
2. Kinematical features detected in the analysis of the ionized gas (see Paper II) and the neutral gas (only in those systems for which interferometer H I maps are available). The kinematical evidences found in the ionized gas of our sample galaxy includes: presence of objects with velocities decoupled from the main rotation pattern (Mkn 1087, Haro 15), sinusoidal velocity patterns that suggest a merging process (HCG 31 AC, Mkn 1199, IRAS 08208+2816, SBS 0926+606 A, III Zw 107, *Object 1* in Tol 1457-262), reversals in the velocity distribution (Tol 9, Arp 252), indications of tidal streaming (HCG 31, IRAS 08208+2816, SBS 1319+579, Tol 9), or the presence of TDG candidates (HCG 31 F1 and F2, Mkn 1087, IRAS 08339+6517, POX 4, Tol 1457-262).

3. Chemical abundance differences within several star-forming regions within the same system: Mkn 1087, Haro 15, and Mkn 1199 are clearly interacting with dwarf galaxies with lower O/H and N/O ratios. NGC 5253, IRAS 08208+2816, and Tol 1457-262 contain zones of different chemical composition. In the case of NGC 5253, this is produced by localized pollution of massive stars, but in the cases of IRAS 08208+2816 and Tol 1457-262 the different chemical compositions seem to be caused by the regions corresponding to different galaxies in interaction.
4. Furthermore, our multiwavelength analysis has provided us further indications of galaxies that do not follow their expected behavior. The analysis of the mass-to-light ratios indicates: very low $M_{H I}/L_B$ in SBS 1319+579 and NGC 5253, high $M_{H II}/L_B$ in SBS 0948+532, low M_{\star}/L_B in SBS 1319+579, and high M_{dyn}/L_B in HCG 31 AC, Mkn 1199, Mkn 5, SBS 1054+365, Tol 9, and Tol 1457-262. Other evidences are: low H I mass content from single-dish data (Mkn 1199, Mkn 5), very extended H I emission embedding several nearby galaxies as HCG 31 (VM03) and Tol 9 (LS08, LS+10b), high M_{Kep} (Mkn 5, IRAS 08339+65 Comp, SBS 1211+540, SBS 1319+579), or important deviations of the star-formation law (Mkn 1199, SBS 1319+579 and NGC 5253). These features may have been produced by interactions (loss of H I mass, enhancing of the star-formation activity, perturbed dynamics) but they are just indirect evidences that should be confirmed by new deep observations (i.e., H I maps).

A question mark in Table 9 indicates that the available data do not allow us to confirm this indicator. Last column in Table 9 compiles the interaction degree that each system is experiencing after considering all positive interaction indicators. We have divided the interaction degree

in four classes: low (no clear signs of interactions), probable (there are some interaction indicators, but deepest data are needed to confirm it), high (we found clear evidences of interactions, but we do not see merger features) and very high (in the cases of finding clear merger features).

Evident mergers between independent objects with relatively similar masses (major mergers) have been detected in HCG 31 AC, SBS 0926+606 A, IRAS 08208+2816 and Tol 1457+262. The galaxy pair Arp 252, that is composed by ESO 566-7 and ESO 566-8, seems also to be experiencing the first stages of a major merger. Minor mergers are found in Haro 15 and Mkn 1199. UM 420 seems also to be experiencing a merger, as deep 3D optical spectroscopy (James et al. 2009) suggests. All these galaxies have a very high interaction degree.

Mkn 1087, IRAS 08339+6517, POX 4, SBS 0926+606 B, III Zw 107 and Tol 9 are experiencing clear interactions with nearby dwarf objects. In the case of POX 4, we still have to investigate (López-Sánchez et al. 2010b) if its dwarf companion galaxy is a TDG candidate and the interaction was with a nearby diffuse H I cloud, or if this object actually is an independent dwarf galaxy that crossed the main body of POX 4 (Méndez & Esteban 1997). These six galaxies have a high interaction degree.

On the other hand, we find probable evidences of interaction in SBS 0948+532 (enhanced star formation activity, long optical tail, probable disturbed kinematics of the ionized gas), SBS 1211+540 (diffuse optical plumes, minor merger indications), SBS 1319+579 (peculiar M_{HI}/L_B , M_{HII}/L_B , and M_*/L_B ratios, perturbed kinematics suggesting merging or tidal stream phenomena). The H I data of NGC 5253 shows disturbed morphology and kinematics (López-Sánchez et al. 2008a), suggesting that this BCDG has disrupted or accreted recently a dwarf gas-rich companion (Kobulnicky & Skillman 2008; López-Sánchez et al. 2010a).

Only Mkn 5, SBS 1054+364, and SBS 1415+437 do not show interaction evidences in our exhaustive multi-wavelength study. However, Mkn 5 seems to be H I-deficient and seems to possess a perturbed neutral gas kinematics because of its relatively high M_{dyn}/L_B ratio. SBS 1054+364 also show a high M_{dyn}/L_B ratio that may suggest perturbed H I kinematics. Furthermore, the chemical abundance of this galaxy is very high in comparison to that expected from its baryonic mass. On the other hand, SBS 1415+437 shows a relatively low oxygen abundance for its baryonic mass.

Considering all indicators, we find that 13 up to 20 systems (68% of our WR galaxy sample) are classified with a high or very high interaction degree. We note, however, that four of these objects (HCG 31, Mkn 1199, IRAS 08339+6517 and Arp 252) show well known interaction evidences, but our analysis reinforces the evidences and improve our knowledge of these systems. Only three galaxies (Mkn 5, SBS 1054+364, and SBS 1415+437) do not show interaction features, but they show considerable divergences of some properties when comparing with similar objects. Hence, it is evident that **the majority of the analyzed galaxies** (17 up to 20) are interacting or merging with or between dwarf objects. Our analysis therefore demonstrates the importance of the low-luminosity galaxies, H I clouds and dwarf objects in the evolution of the galaxies. Interactions with dwarf galaxies also may initiate star-formation events in normal spiral

galaxies, such it occurs in the external arms of Mkn 1199, in Haro 15, surrounding Mkn 1087, or in the impressive galaxy pair NGC 1512/1510 (Koribalski & López-Sánchez 2009). Definetively, interactions between dwarf galaxies is one of the main triggering mechanism of the star-formation activity in starburst galaxies, but these dwarf objects are only detected when deep optical images and spectroscopy and complementary H I observations are obtained.

12. Conclusions

We have presented a comprehensive analysis of a sample of 20 starburst galaxies that show the presence of a substantial population of very young massive stars, most of them classified as Wolf-Rayet galaxies. In this paper, the last of the series, we analyze the global properties of our galaxy sample using all multiwavelength data, that include X-ray, *FUV*, *FIR*, and radio (both H I spectral line at 21 cm and 1.4 GHz radio-continuum) results. Our main conclusions are the following:

1. We compared the values of the SFR derived from several indicators that consider fluxes at different wavelengths. The results agree well within the experimental errors and with our H α -based values, that were obtained after correcting for reddening and [N II] contribution. However, we consider that the new H α -based calibration provided by Calzetti et al. (2007) should be preferred over the well-known and extensively used Kennicutt (1998) calibration. Additionally, we checked that the *FUV*-based SFR very often shows similar results to those obtained using the emission of the ionized gas, providing a powerful tool to analyze independently the star-formation activity in both global and local scales.
2. We checked that the SFR/ L_B ratio decreases with increasing metallicity. We derived empirical relationships between the *U*-band, *B*-band, and X-ray luminosities and the SFR, that can be only used in starburst galaxies and as a first estimation of the real SFR value.
3. All objects except one in our galaxy sample satisfy the *FIR*-radio correlation, indicating that they are pure star-forming systems. Only the galaxy ESO 566-8 lies away from the *FIR*-radio correlation because it seems to host some kind of nuclear activity. The non-thermal-to-thermal ratio seems to increase with increasing luminosity, suggesting that the cosmic-ray confinement is more efficient in massive galaxies than in dwarf objects.
4. We provided empirical relationships between the ionized gas mass, neutral gas mass, dust mass, stellar mass, and dynamical mass with the *B*-luminosity. Although all mass estimations increase with increasing luminosity, we find important deviations to the general trend in some objects, that seem to be consequence of peculiarities in these galaxies. The comparison between the dynamical mass (derived from the kinematics of the neutral gas) with the Keplerian mass (obtained from the kinematics of the ionized gas) and the stellar mass (from the *H*-band luminosity) provides further clues about systems in which the dynamics seem to be highly perturbed. We remark the importance of this study, because it is not common to find in the literature a comprehensive and detailed analysis of a sample of galaxies for which the total (dynamical or stellar) mass, the reddening-corrected

- luminosity in optical and *NIR* filters, and the T_e -based oxygen abundance, have been derived in a coherent way.
5. We investigated some mass-metallicity relations and compared with previous results found in the literature. As pointed out by Kewley & Ellison (2008), the choice of the metallicity calibration has a strong effect in the derived $M - Z$ relation. The tightness of the $M_{dyn} - Z$ calibration indicates that the dark matter content also increases with metallicity. The scatter in the $M_{stars} - Z$ and $M_{bar} - Z$ relations are consequence of both the nature (dwarf galaxies, TDG candidates, mergers) and the star-formation histories experienced in each galaxy.
 6. We found that our sample galaxies agree well with the Schmidt-Kennicutt scaling law of star-formation derived by Kennicutt et al. (2007), that considers individual star-forming regions within M 51. Some important deviation are found in NGC 5253 and Mkn 1199, that are very H I-deficient, and in SBS 1319+579, where the star-formation activity seems to be suppressed.
 7. The study of the mass-to-light ratios reinforces some of the results found in our analysis. We found that the neutral-gas-mass-to-luminosity ratio clearly decreases with increasing mass, as it seems to happen with the ionized-gas-mass-to-luminosity ratio. The ionizing-cluster-mass-to-luminosity ratio, however, seems to be constant with metallicity. The fact that we do not find any dwarf galaxy high M_{HI}/L_B ratio indicates that they have not experienced a lonely life. The analysis of the M_{gas}/M_{stars} ratio suggests that this kind of galaxies have equal amount of neutral and stellar masses for metallicities $12+\log(O/H)\sim 8.2-8.3$. The stellar-mass-to-luminosity ratio clearly increases with the $B - R$ colour.
 8. We found that the reddening coefficient derived from the Balmer decrement clearly increases the the warm dust mass, indicating that the extinction is mainly internal to the galaxy and not in the line-of-sight. We confirmed that the dust-to-gas ratio increases with the metallicity, and suggested that the low M_{dust}/M_{gas} ratios in dwarf low-metallicity galaxies is consequence of the large reserves of un-enriched neutral gas. However, the low M_{dust}/M_{gas} ratios observed at the outskirts of spiral galaxies seem to be a result of the decreasing of the star-formation efficiency in these regions.
 9. The comparison of our data with the closed-box model clearly indicates that environment effects have played and important role in the evolution of the analyzed galaxies. The main effective yield we derived for our data agrees quite well with results found in the literature, in particular with results found in other starburst or irregular dwarf galaxies.

Considering all available data, we quantified how many galaxies are experiencing interaction or merger processes. We found that 17 up to 20 objects are clearly interacting or merging with low-luminosity dwarf objects or H I clouds, and all the remnant three galaxies (Mkn 5, SBS 1054+364, and SBS 1415+437) show considerable divergences of some properties when comparing with similar objects. However, the interacting/merging features are only detected when deep optical spectroscopy and a detailed multi-wavelength analysis, remarking analysis of the kinematics and distribution of the neutral gas, are obtained. We therefore con-

clude that interactions do play a fundamental role in the triggering mechanism of the strong star-formation activity observed in dwarf starburst galaxies. This observational result completely agrees with the hierarchical model of galaxy formation that considers that large galactic structures were built up from the accretion of dwarf galaxies.

Acknowledgements. Based on observations made with NOT (Nordic Optical Telescope), INT (Isaac Newton Telescope) and WHT (William Herschel Telescope) operated on the island of La Palma jointly by Denmark, Finland, Iceland, Norway and Sweden (NOT) or the Isaac Newton Group (INT, WHT) in the Spanish Observatorio del Roque de Los Muchachos of the Instituto de Astrofísica de Canarias. Based on observations made at the Centro Astronómico Hispano Alemán (CAHA) at Calar Alto, operated by the Max-Planck Institut für Astronomie and the Instituto de Astrofísica de Andalucía (CSIC). Based on observations made with the ATCA (Australia Telescope Compact Array), which is funded by the Commonwealth of Australia for operation as a National Facility managed by CSIRO.

Á.R. L-S thanks César Esteban (his formal PhD supervisor) for all the help and very valuable explanations, talks and discussions along these years. He also acknowledges Jorge García-Rojas, Sergio Simón-Díaz and José Caballero for their help and friendship during his PhD, extending this acknowledge to all people at Instituto de Astrofísica de Canarias (Spain). Á.R. L-S. *deeply* thanks the Universidad de La Laguna (Tenerife, Spain) for force him to translate his PhD thesis from English to Spanish; he had to translate it from Spanish to English to complete this publication. This was the main reason of the delay of the publication of this research, because the main results shown here were already included in the PhD dissertation (in Spanish) which the author finished in 2006 (López-Sánchez 2006). The author is indebted to the people at the CSIRO Astronomy and Space Science / Australia Telescope National Facility, especially Bärbel Koribalski, for their support and friendship while translating his PhD. The author also thanks Bärbel Koribalski (CSIRO/ATNF) for her help analyzing HIPASS data and all the talk and discussions about radio-astronomy.

This work has been partially funded by the Spanish Ministerio de Ciencia y Tecnología (MCyT) under projects AYA2004-07466 and AYA2007-63030. This research has made use of the NASA/IPAC Extragalactic Database (NED) which is operated by the Jet Propulsion Laboratory, California Institute of Technology, under contract with the National Aeronautics and Space Administration. The Galaxy Evolution Explorer (GALEX) is a NASA Small Explorer, launched in April 2003. We gratefully acknowledge NASA's support for construction, operation, and science analysis for the GALEX mission. The Infrared Astronomical Satellite (IRAS) mission was a collaborative effort by the United States (NASA), the Netherlands (NIVR), and the United Kingdom (SERC). This research has made extensive use of the SAO/NASA Astrophysics Data System Bibliographic Services (ADS).

References

- Alloin D., Collin-Souffrin S., Joly M. & Vigroux L. 1979, *A&A*, 78, 200
 Amorín, R. O.; Muñoz-Tuñón, C., Aguerri, J.A.L., Cairós, L.M. & Caon, N. 2007, *A&A*, 467, 541
 Amorín, R., Aguerri, J.A.L., Muñoz-Tuñón, C. & Cairós, L. M. 2009, *A&A*, 501, 75
 Arp, H.C. 1966, *ApJS*, 14, 1
 Arribas, S., Bushouse, H., Lucas, R.A., Colina, L. & Borne, K.D. 2004, *AJ*, 127, 2522
 Barone, L.T., Heithausen, A., Hüttemeister, S., Fritz, T. & Klein, U. 2002, *MNRAS*, 317, 649
 Barnes, D.G. et al. 2001, *MNRAS*, 322, 486
 Barton, E.J., Geller, M.J. & Kenyon, S.J. 2000, *ApJ*, 530, 660
 Basu-Zych, A.R.; Goncalves, T.S., Overzier, R., Law, D.R., Schiminovich, D., Heckman, T., Martin, C., Wyder, T. & O'Dowd, M. 2009, *ApJ*, 699, 118
 Begum, A., Chengalur, J.N., Karachentsev, I.D., Kaisin, S.S. & Sharina, M.E. 2006, *MNRAS*, 365, 1220
 Begum, A., Chengalur, J.N., Karachentsev, I.D., Sharina, M.E. & Kaisin, S.S. 2008, *MNRAS*, 386, 1667
 Bekki, K. 2008, *MNRAS*, 388, 10
 Bell, E.F. 2003, *ApJ*, 586, 794
 Bell, E.F. & de Jong, R.S. 2000, *MNRAS*, 312, 497
 Bergvall, N. & Östlin, G. 2002, *A&A*, 390, 891
 Bessell, M. S., Castelli, F. & Plez, B. 1998, *A&A*, 333, 231
 Bomans, D.J. 2005, *AIPC*, 783, 98, proceedings of *The Evolution of the Starburst: The 331st Wilhelm and Else Heraeus Seminar*

- Bomars, D.J., van Eymeren, J., Dettmar, R.-J., Weis, K. & Hopp, U. 2007, *NewAR*, 51, 141
- Boselli, A., Gavazzi, G., Donas, J. & Scodreggio, M. 2001, *AJ*, 121, 753
- Bothun, G.D., Romanishin, W., Strom, S.E. & Strom, K.M. 1984, *AJ*, 89, 1300
- Braine, J., Lisenfeld, U. Due, P.-A. & Leon, S. 2000, *Natur*, 403, 867
- Braine, J., Duc, P.-A., Lisenfeld, U., Charmandaris, V., Vallejo, O., Leon, S. & Brinks, E. 2001, *A&A*, 378, 51
- Braine J., Duc P.-A., Lisenfeld U., Brinks E., Charmandaris V., Leon S. 2004, in 'Recycling Intergalactic and Interstellar Matter', IAU Symposium 217, ed. P.A. Duc, J. Braine and E. Brinks, p. 518
- Bravo-Alfaro, H., Brinks, E., Baker, A. J., Walter, F., & Kunth, D. 2004, *AJ*, 127, 264
- Bravo-Alfaro, H., Coziol, R., & Brinks, E. 2006, *RevMexAA*, 42, 261
- Brinchmann, J., Kunth, D., & Durret, F. 2008, *A&A*, 485, 657
- Broeils, A.H. & van Woerden, H. 1994, *A&AS*, 107, 129
- Bruzual, G. & Charlot, S. 2003, *MNRAS*, 344, 1000, BC03
- Cairós, L.M., Vílchez, J.M., González Pérez, J.N., Iglesias-Páramo, J. & Caon, N. 2001a, *ApJS*, 133, 321
- Cairós, L. M., Caon, N., Vílchez, J. M., González-Pérez, J. N. & Muñoz-Tuñón, C. 2001b, *ApJS*, 136, 393
- Cairós, L.M.; Caon, N., Zurita, C., Kehrig, C., Weibacher, P. & Roth, M. 2009, *A&A*, 507, 1291
- Calura, F., Matteucci, F. & Menci, N. 2004, *MNRAS*, 353, 500
- Calzetti, D. 2001, *PASP*, 113, 1149
- Calzetti, D. et al. 2007, *ApJ*, 666, 870
- Campos-Aguilar, A., Moles, M. & Masegosa, J. 1993, *AJ*, 106 1784
- Cannon, J.M., Skillman, E.D., Kunth, D., Leitherer, C., Mas-Hesse, M., Östlin, M. & Petrosian, A. 2004, *ApJ*, 608, 768
- Cardamone, C. et al. 2009, *MNRAS*, 399, 1191
- Cardelli, J. A., Clayton, G. C. & Mathis J. S. 1989, *ApJ*, 345, 245
- Casasola, V., Bettoni, D. & Galletta, G. 2004, *A&A*, 422, 941
- Clayton, D.D. & Pantelaki, I. 1993, *PhR*, 227, 293
- Colina, L., Bohlin, R.C. & Castelli, F., 1996, *AJ*, 112, 307
- Colina, L., Arribas, S. & Monreal-Ibero, A. 2005, *ApJ*, 621, 725
- Condon, J.J. 1992, *ARA&A* 30, 575
- Condon, J.J., Helou, G., Sanders, D.B. & Soifer, B.T. 1990, *ApJS* 73, 359
- Condon, J.J., Anderson, M.L. & Helou, G. 1991, *ApJ*, 376, 95
- Condon, J. J., Cotton, W. D., Greisen, E. W., Yin, Q. F., Perley, R. A., Taylor, G. B. & Broderick, J. J. 1998, *AJ*, 115, 1693
- Condon, J.J., Cotton, W.D. & Broderick, J.J. 2002, *AJ*, 124, 675
- Crowther, P.A. 2007, *ARA&A*, 45, 177
- Crowther, P.A. & Hadfield, L.J., 2006, *A&A*, 449, 711
- Cumming, R.J., Fathi, K., Östlin, G., Marquart, T., Márquez, I., Masegosa, J., Bergvall, N. & Amram, P. 2008, *A&A*, 479, 725
- Davé, R. & Oppenheimer, B.D. 2007, *MNRAS*, 374, 427
- Davies, J.I. & Phillipps, S. 1988, *MNRAS*, 233, 553
- Davoust, E. & Contini, T. 2004, *A&A*, 416, 515
- de Blok, W.J.G., Walter, F., Brinks, E., Trachternach, C., Oh, S.-H. & Kennicutt, R.C. 2008, *AJ*, 136, 2648
- de Jong, R.S. 1996, *A&A*, 313, 377
- De Lucia, G., Kauffmann, G. & White, S.D.M. 2004, *MNRAS*, 374, 323
- Denicoló, G., Terlevich, R. & Terlevich, E. 2002, *MNRAS*, 330, 69
- de Naray R. K., McGaugh S. S. & de Blok W. J. G., 2004, *MNRAS*, 355, 887
- De Rossi, M.E., Tissera, P.B., & Scannapieco, C. 2006, *MNRAS*, 374, 323
- Díaz, A.I., & Pérez-Montero, E. 2000, *MNRAS*, 312, 130
- Dopita, M.A. & Evans, I. N. 1986, *ApJ*, 307, 431
- Dopita, M.A., Kewley, L. J., Heisler, C.A. & Sutherland, R.S. 2000, *ApJ*, 542, 224
- Dopita, M.A., Pereira, M., Kewley, L.J. & Capaccioni, 2002, *ApJS* 143, 47
- Draine, B.T. et al. 2007, *ApJ*, 663, 866
- Dubois, Y. & Teyssier, R. 2007, *EAS*, 24, 95
- Duc, P.-A. & Mirabel, I. F. 1998, *A&A* 338, 813
- Duc, P.A., Brinks, E., Springel, V., Pichardo, B., Weibacher, P. & Mirabel, I.F. 2000, *AJ*, 120, 1238
- Edmunds, M.G. & Pagel, B.E.J. 1978, *MNRAS*, 185, 77
- Edmunds, M.G. & Pagel, B.E.J. 1984, *MNRAS*, 211, 507
- Edmunds, M.G. 1990, *MNRAS*, 246, 678
- Ekta, Chengalur J.N. & Pustilnik, S.A. 2006, *MNRAS*, 372, 853
- Ekta, Chengalur J.N. & Pustilnik, S.A. 2008, *MNRAS*, 391, 881
- Emonts, B.H.C., Morganti, R., Oosterloo, T.A., van der Hulst, J.M., Tadhunter, C.N., van Moorsel, G. & Holt, J. 2006, *AN*, 327, 139
- English, J., Koribalski, B.S., Bland-Hawthorn, J., Freeman, K.C. & McCain, C.F. 2010, *AJ*, 139, 102
- Erb, D.K., Shapley, A.E., Steidel, C.C., Pettini, M. et al. 2003, *ApJ*, 591, 101
- Erb, D.K., Shapley, A.E., Pettini, M., Steidel, C.C., Reddy, N.A. & Adelberger, K.L. 2006, *ApJ*, 644, 813
- Esteban, C. & Peimbert, M. 1995, *A&A*, 300, 78
- Esteban, C., Bresolin, F., Peimbert, M., García-Rojas, J., Peimbert, A. & Mesa-Delgado, A. 2009, *ApJ*, 700, 654
- Ferland G. J., Korista K. T., Verner D. A., Ferguson J. W., Kingdon J. B. & Verner E. M, 1998, *PASP*, 110, 761
- Fioc, M. & Rocca-Volmerange, B. 1997, *A&A* 326, 950
- Gallagher, J.S. III, Hunter, D.A. & Tutukov, A.V. 1984, *ApJ* 284, 544
- García-Lorenzo, B., Cairós, L.M., Caon, N., Monreal-Ibero, A. & Kehrig, C. 2008, *ApJ*, 677, 201
- García-Rojas, J. & Esteban, C., 2007, *ApJ*, 670, 457
- Garnett, D.R. 1992, *AJ*, 103, 1330
- Garnett, D.R. 2002, *ApJ*, 581, 1019
- Genzel, R., Lutz, D., Sturm, E., Egami, E., Kunze, D., Moorwood, A.F.M., Rigopoulou, D., Spoon, H.W.W., Sternberg, A., Tacconi-Garman, L.E., Tacconi, L. & Thatte, N. 1998, *ApJ*, 498, 579
- Gerola, H., Seiden, P.E. & Schulman, L.S. 1980, *ApJ*, 242, 517
- Giovanelli, R. et al. 2005, *AJ*, 130, 2598
- Gil de Paz, A., Madore, B.F. & Pevunova, O. 2003, *ApJS*, 147, 29
- Gil de Paz, A., Madore, B.F., Boissier, S., Swaters, R., Popescu, C. C., Tuffs, R. J., Sheth, K., Kennicutt, R.C., Jr., Bianchi, L., Thilker, D. & Martin, D.C. 2005, *ApJ*, 627, 29
- Gil de Paz, A., et al. 2007, *ApJ*, 661, 115
- Gordon, D. & Gottesman, S.T. 1981, *AJ*, 86, 161
- Guzman, R., Gallego, J., Koo, D.C., Phillips, A.C., Lowenthal, J.D., Faber, S.M., Illingworth, G.D. & Vogt, N.P. 1997, *ApJ*, 489, 559
- Hägele, G.F., Díez, A.L., Terlevich, E., Terlevich, R., Pérez-Montero, E. & Cardaci, M.V. 2008, *MNRAS*, 383, 209
- Heckmann, T.M. 1999, *Ap&SS*, 266, 3
- Henry, R.B.C., Edmunds, M.G. & Köppen, J. 2000, *ApJ*, 541, 660
- Hidalgo-Gómez, A.M. & Olofsson, K. 1998, *A&A*, 334, 45
- Hibbard, J.E. & van Gorkom, J.H. 1996, *AJ*, 111, 655
- Hibbard, J.E., van Gorkom, J.H., Rupen, M.P. & Schiminovich, D. 2001b, *An HI Rogues Gallery*, ASP Conf. Ser. 240: *Gas and Galaxy Evolution*, 240, 657
- Hirashita, H. 2000, *PASJ*, 52, 107
- Hirashita, H., Inoue, A.K., Kamaya, H. & Shibai, H. 2001, *A&A*, 366, 83
- Hopkins, A. M., Schulte-Ladbeck, R. E. & Drozdovsky, I. O. 2002, *AJ*, 124, 862
- Huchtmeier, W.K., Sage, L.J. & Henkel, C. 1995, *A&A*, 300, 675
- Huchtmeier, W. K., Krishna, G. & Petrosian, A. 2005, *A&A*, 434, 887
- Huchtmeier, W. K., Petrosian, A., Krishna, G. & Kunth, D. 2007, *A&A*, 462, 919
- Huchtmeier, W. K., Petrosian, A., Krishna, G. McLean, B. & Kunth, D. 2008, *A&A*, 492, 367
- Izotov, Y.I. & Thuan, T.X. 1998, *ApJ*, 500, 188
- Izotov, Y.I. & Thuan, T.X. 1999, *ApJ*, 511, 639
- Izotov, Y.I. & Thuan, T.X. 2004, *ApJ*, 616, 768
- Izotov, Y.I., Papaderos, P., Guseva, N.G., Fricke, K.J. & Thuan, T.X. 2004, *A&A* 421, 539
- Izotov, Y.I., Stasińska, G., Meynet, G., Guseva, N.G. & Thuan, T.X. 2006, *A&A*, 448, 955
- James, A., Dunne, L., Eales, S. & Edmunds, M.G. 2002, *MNRAS*, 335, 753
- James, P.A., Shane, N.S., Knapen, J.H., Etherton, J. & Percival, S.M. 2005, *A&A*, 429, 851
- James, B.L., Tsamis, Y.G., Barlow, M.J., Westmoquette, M.S., Walsh, J.R., Cuisinier, F. & Exter, K.M. 2009, *MNRAS*, 398, 2
- James, B.L., Tsamis, Y.G. & Barlow, M.J. 2010, *MNRAS*, 401, 759
- Jansen, R.A., Franx, M., Fabricant, D. & Caldwell, N. 2000, *ApJS*, 126, 271
- Jensen E. B., Strom K. M. & Strom S. E. 1976, *ApJ*, 209, 748
- Johnson, K.E. & Kobulnicky, H.A. 2003, *ApJ*, 597, 923
- Johnson, K.E., Indebetow, R., Watson, C., & Kobulnicky, H. A. 2004, *AJ*, 128, 610
- Joseph, R. D. & Wright, G. S. 1985, *MNRAS*, 214, 87
- Karachentsev, I.D., Karachentseva, V.E., Huchtmeier, W.K. & Makarov, D.I. 2004, *AJ*, 127, 2031
- Kauffmann, G. & White, S.D.M. 1993, *MNRAS*, 261, 921
- Kaufman, M., Brinks, E., Elmegreen, D.M., Thomasson, M., Elmegreen, B.G., Struck, C. & Klaric, M. 1997, *AJ*, 114, 2323
- Kauffmann, G. et al. 2003, *MNRAS*, 346, 1055
- Kay, S.T., Pearce, F.R., Frenk, C.S. & Jenkins, A. 2002, *MNRAS*, 330, 113
- Kennicutt, R.C. Jr. 1998, *ApJ*, 498, 541
- Kennicutt, R.C. Jr., Bresolin, F. & Garnett, D.R. 2003, *ApJ*, 591, 801
- Kennicutt, R.C. Jr., et al. 2007, *ApJ*, 671, 333
- Kewley, L.J., Dopita, M.A., Sutherland, R.S., Heisler, C.A. & Trevena, J. 2001, *ApJS*, 556, 121
- Kewley, L.J. & Dopita, M.A. 2002, *ApJS*, 142, 35
- Kewley, L.J., & Ellison, S.E. 2008, *ApJ*, 681, 1183
- Kinman, T.D. & Davidson, K. 1981, *ApJ*, 243, 127
- Kirby, E.M., Jerjen, H., Ryder, S.D. & Driver, S.P. 2008, *AJ*, 136, 1866
- Kobulnicky, H.A. & Skillman, E.D. 1998, *ApJ*, 497, 601
- Kobulnicky H. A. & Kewley L. J. 2004, *ApJ*, 617, 240
- Kobulnicky, H.A. & Skillman, E.D. 2008, *AJ*, 135, 527
- Kobulnicky, H.A., Skillman, E.D., Roy, J.-R., Walsh, J.R. & Rosa, M.R., 1997, *ApJ*, 277, 679
- Kobulnicky, H.A. & Johnson, K.E. 1999, *ApJ*, 627, 154
- Kobulnicky, H.A., Kennicutt, R.C.Jr. & Pizagno, J.L. 1999, *ApJ* 514, 544
- Kobulnicky, H. A., Willmer, C.N.A., Phillips, A.C., Koo, D.C., Faber, S.M., Weiner, B.J., Sarajedini, V.L., Simard, L. & Vogt, N.P. 2003, *ApJ* 599, 1006
- Koribalski, B. 1996, *ASPC* 106, 238
- Koribalski, B., Gordon, S. & Jones, K. 2003, *MNRAS*, 339, 1203

- Koribalski, B. S., et al. 2004, *AJ*, 128, 16
- Koribalski, B. & Dickey, J.M. 2004, *MNRAS*, 348, 1255
- Koribalski, B. & Manthey, E. 2005, *MNRAS*, 358, 202
- Koribalski, B.S. & López-Sánchez, Á.R. 2009, *MNRAS*, 400, 1749
- Lambas, D.G., Tissera, P.B., Alonso, M.S. & Coldwell, G. 2003, *MNRAS*, 346, 1189
- Larson, R. B. & Tinsley, B. M. 1978, *ApJ*, 219, 46
- Lee, H., McCall, M.L., Kingsburgh, R.L., Ross, R. & Stevenson, C.C. 2003, *AJ*, 125, 146
- Lee, H., Zucker, D.B. & Grebel, E.K. 2007, *MNRAS*, 376, 820
- Lee, J.C., Salzer J.J. & Melbourne, J. 2004, *ApJ*, 616, 752L
- Lee, J.C., et al. 2009, *ApJ*, 706, 599
- Leitherer, C., Schaerer, D., Goldader, J.D., González-Delgado, R.M., Robert, C., Kune, D.F., de Mello, D.F., Devost, D. & Heckman, T.M. 1999, *ApJS*, 123, 3 (*STARBURST 99*)
- Lequeux, J., Peimbert, M., Rayo, J.F., Serrano, A. & Torres-Peimbert, S. 1979, *A&A*, 80, 155
- Leroy, A.K., Walter, F., Brinks, E., Bigiel, F., de Blok, W.J.G., Madore, B. & Thornley, M.D. 2008, *AJ*, 136, 2782
- Liang, Y.C., Yin, S.Y., Hammer, F., Deng, L.C., Flores, H. & Zhang, B. 2006, *ApJ*, 652, 257
- Lilly, S.J., Carollo, C.M. & Stockton, A.N. 2003, *ApJ*, 597, 730
- Lisenfeld, U. & Ferrara, A. 1998, *ApJ*, 496, 145
- Lonsdale, C. J., Persson, S. E. & Matthews, K., 1984, *ApJ*, 287, 95
- López-Sánchez, Á.R. 2006, PhD Thesis, Universidad de la Laguna (Tenerife, Spain)
- López-Sánchez, Á.R., Esteban, C. & Rodríguez, M. 2004a, *ApJS*, 153, 243
- López-Sánchez, Á.R., Esteban, C. & Rodríguez, M. 2004b, *A&A* 428,445
- López-Sánchez, Á.R., Esteban, C. & García-Rojas, J. 2006, *A&A*, 449, 997
- López-Sánchez, Á.R., Esteban, C., García-Rojas, J., Peimbert, M. & Rodríguez, M. 2007, *ApJ*, 656, 168
- López-Sánchez, Á.R. & Esteban, C. 2008, *A&A*, 491, 131, Paper I
- López-Sánchez, Á.R., Koribalski, B. & Esteban, C. 2008a, *proc. of Galaxies in the Local Volume*, Springer, p.53
- López-Sánchez, Á.R., Koribalski, B., Esteban, C. & Hibbard, J. 2008b, *proc. of Galaxies in the Local Volume*, Springer, p.301
- López-Sánchez, Á.R. & Esteban, C. 2009, *A&A*, 508, 615, Paper II
- López-Sánchez, Á.R. & Esteban, C. 2010a, *A&A*, in press, Paper III
- López-Sánchez, Á.R. & Esteban, C. 2010b, *A&A*, in press, Paper IV
- López-Sánchez, Á.R., Koribalski, B.S., van Eymeren, J., Esteban, C. et al. 2010a, *MNRAS*, in prep (NGC 5253)
- López-Sánchez, Á.R., Koribalski, B.S., Esteban, C., et al. 2010b, *MNRAS*, in prep (Tol 9)
- Lou, Y.-Q. & Bian, F.-Y. 2005, *MNRAS*, 358, 1231
- Mac Low, M.-M. & Ferrara, A. 1999, *ApJ*, 513, 142
- Marlowe, A.T., Heckman, T.M., Wyse, R.F.G. & Schommer, R. 1995, *ApJ*, 438, 563
- Mathewson, D.S., Ford, V.L. & Buchhorn, M. 1992, *ApJS*, 81, 413
- McCall, M.L., Rybski, P.M. & Shields, G.A. 1985, *ApJS* 57, 1
- McGaugh, S.S. 1991, *ApJ*, 380, 140
- McGaugh, S.S. 1994, *ApJ*, 426, 135
- McGaugh, S.S. & de Blok, W.J.G. 1997, *ApJ*, 481, 689
- Mendes de Oliveira, C.L., Temporin, S., Cypriano, E.S., Plana, H., Amram, P., Sodr, L. Jr. & Balkowski, C. 2006, *AJ*, 132, 570
- Méndez, D.I. & Esteban, C. 1997, *ApJ*, 488, 652
- Méndez, D.I. & Esteban, C. 1999, *AJ*, 118, 2733
- Méndez, D.I. & Esteban, C., 2000, *A&A*, 359, 493
- Meyer, M.J. et al. 2004, *MNRAS*, 350, 1195
- Meynet, G. & Maeder, A. 2002, *A&A*, 390, 561
- Meynet G. & Maeder A. 2005, *A&A*, 429, 581
- Morrissey, P. & GALEX Science Team, 2005, *BAAS*, 37, 1454
- Muñoz-Mateos, J.C. et al. 2009, *ApJ*, 703, 1569
- Nagao, T., Maiolino, R. & Marconi, A. 2006, *A&A*, 459, 85
- Niklas, S., Klein, U. & Wielebinski, R. 1997, *A&A*, 322, 19
- Nikolic, B., Cullen, H. & Alexander, P. 2004, *MNRAS*, 355, 874
- Noeske, K.G., Iglesias-Páramo, J., Vílchez, J.M., Papaderos, P. & Fricke, K.J. 2001, *A&A*, 371, 806
- Noeske, K.G., Papaderos, P., Cairós, L.M. & Fricke, K.J. 2003, *A&A*, 410, 481
- Noeske, K.G., Papaderos, P., Cairós, L.M. & Fricke, K.J. 2005, *A&A*, 429, 115
- Oey M. S. & Shields J. C., 2000, *ApJ*, 539, 687
- Östlin, G., Amram, P., Bergvall, N., Masegosa, J., Boulesteix, J. & Márquez, I. 2001, *A&A*, 374, 800
- Östlin, G., Cumming, R.J., Amram, P., Bergvall, N., Kunth, D., Márquez, I., Masegosa, J. & Zackrisson, E. 2004, *A&A*, 419, 43
- Overzier, R.A. et al. 2009, *ApJ*, 706, 203
- Pagel, B. E. J., Edmunds, M. G., Blackwell, D. E., Chun, M. S., Smith, G. 1979, *MNRAS*, 189, 95
- Papaderos, P., Guseva, N.G., Izotov, Y.I., Noeske, K.G., Thuan, T.X. & Fricke, K.J., 2006, *A&A*, 457, 45
- Paturel, G., Theureau, G., Bottinelli, L., Gouguenheim, L., Coudreau-Durand, N., Hallet, N. & Petit, C. 2003, *A&A*, 412, 57
- Peimbert, M. 1967, *ApJ*, 150, 825
- Peimbert, M., Peimbert, A., Esteban, C.; García-Rojas, J., Bresolin, F., Carigi, L., Ruiz, M.T. & López-Sánchez, Á.R. 2007, *RMxAC*, 29, 72
- Peña, M. & Ayala, S. 1993, *RevMexAA*, 27, 171
- Pérez-Montero, E. & Díaz, A. I. 2005, *MNRAS*, 361, 1063
- Pettini, M. & Pagel, B.E.J. 2004, *MNRAS*, 348, 59
- Pettini, M., Shapley, A.E., Steidel, C.C., Cuby, J.-G., Dickinson, M., Moorwood, A.F.M., Adelberger, K.L. & Gialalisco, M. 2001, *ApJ*, 554, 981
- Pilyugin, L.S. 2000, *A&A*, 362, 325
- Pilyugin, L.S. 2001a, *A&A*, 369, 594
- Pilyugin, L.S. 2001b, *A&A*, 374, 412
- Pilyugin, L.S., Thuan, T.X. & Vílchez, J.M. 2003, *A&A*, 397, 487
- Pilyugin, L. S., Vílchez, J. M. & Contini, T. 2004, *A&A*, 425, 849
- Pilyugin, L.S. & Thuan, T.X. 2005, *ApJ*, 631, 231
- Piovan, L., Tantaló, R. & Chiosi, C. 2006, *MNRAS*, 366, 923
- Pustilnik, S. A., Kniazev, A. Y., Lipovetsky, V. A. & Ugryumov, A. V. 2001, *A&A*, 373, 24
- Pustilnik, S. A., Martin, J.-M., Huchtmeier, W. K., Brosch, N., Lipovetsky, V. A. & Richter, G. M. 2002, *A&A*, 389, 405
- Pustilnik, S., Kniazev, A., Pramskij, A., Izotov, Y., Foltz, C., Brosch, N., Martin, J.-M. & Ugryumov, A. 2004, *A&A* 419, 469
- Putman, M.E., Staveley-Smith, L., Freeman, K.C., Gibson, B.K. & Barnes, D.G. 2003, *ApJ*, 586, 170
- Ranalli, P., Comastri, A. & Setti, G. 2003, *A&A* 399, 39
- Richer, M.G. & McCall, M.L. 1995, *ApJ*, 445, 642
- Robert, M.S. 1975, in *Galaxies and the Universe*. Edited by Allan Sandage, Mary Sandage, and Jerome Kristian, with an index prepared by Gustav A. Tammann. Published by the University of Chicago Press (Stars and Stellar Systems. Volume 9), Chicago, IL USA., p.309
- Roberts, M.S. & Haynes, M.P. 1994, *ARA&A*, 32, 115
- Roussel H., Sauvage, M., Vigroux, L. & Bosma, A. 2001, *A&A* 372, 427
- Rubin, V. C., Ford, W. K., Jr., & Whitmore, B. C. 1984, *ApJ*, 281, L21
- Salim S., et al. 2007, *ApJS*, 173, 267
- Salpeter, E.E. & Hoffman, G.L. 1996, *ApJ*, 465, 595
- Salzer, J. J., Rosenberg, J. L., Weissstein, E. W., Mazzarella, J. M. & Bothun, G. D. 2002, *AJ*, 124, 191
- Salzer, J. J., Lee, J. C., Melbourne, J., Hinz, J. L., Alonso-Herrero, A. & Jangren, A. 2005, *ApJ*, 624, 661
- Sanders, D. B. 1997, *RMxAC*, 6, 42
- Sanders, D.B. & Mirabel, I.F. 1996, *ARA&A*, 34, 749
- Sargent, W.L.W. & Searle, L. 1970, *ApJ*, 162, L155
- Schaerer, D. & Vacca, W.D. 1998, *ApJ*, 497, 618 (SV98)
- Schaerer, D., Contini, T. & Pindao, M. 1999, *A&AS* 136, 35
- Schmidt, M. 1959, *ApJ*, 129, 243
- Schmidt, M. 1963, *ApJ*, 137, 758
- Searle, L. & Sargent, W.L.W. 1972, *ApJ*, 173, 25
- Silich, S.A. & Tenorio-Tagle, G. 1998, *MNRAS*, 299, 249
- Skillman, E.D., Kennicutt, R.C. & Hodge, P.W. 1989, *ApJ*, 347, 875
- Skillman, E.D., Côté, S. & Miller, B.W. 2003, *AJ* 125, 593
- Solomon, P. M. & Sage L. J., 1988, *ApJ*, 334, 613
- Somerville, R.S. & Primack, J.R. 1999, *MNRAS*, 310, 1087
- Schneider, S.E. 1989, *ApJ*, 343, 94
- Springel, V. & Hernquist, L. 2003, *MNRAS*, 339, 312
- Springel, V., White, S. et al. 2005, *Nature*, 435, 629
- Stasińska, G. 2002, *RMxAC*, 12, 62
- Stasińska, G. 2005, *A&A*, 434, 507
- Stasińska, G. 2006, *A&A*, 454, 127
- Stasińska, G. 2009, proceedings of IAU symposium 262, *Stellar Populations - planning for the next decade*, eds Bruzual & Charlot, astro-ph:0910.0175
- Stasińska, G., Schaerer, D. & Leitherer, C. 2001, *A&A*, 370, 1
- Steidel C. C., Shapley A. E., Pettini M., Adelberger K. L., Erb D. K., Reddy N. A. & Hunt M. P., 2004, *ApJ*, 604, 534
- Stevens, I.R. & Strickland, D. K. 1998a, *MNRAS*, 294, 523
- Stevens, I.R. & Strickland, D. K. 1998b, *MNRAS*, 301, 215
- Storchi-Bergmann, T., Calzetti, D. & Kinney, A.L. 1994, *ApJ*, 429, 572
- Sutherland, R.S. & Dopita, M.A. 1993, *ApJS*, 88, 253
- Taylor, C. L., Brinks, E. & Skillman, E. D., 1993, *AJ*, 105, 128
- Taylor, C., Brinks, E., Grashuis, R. M. & Skillman, E. D., 1995, *ApJS*, 99, 427
- Taylor, C., Thomas, D., Brinks, E., & Skillman, E. D., 1996, *ApJS*, 107, 143
- Taylor, C.L., Kobulnicky, H.A. & Skillman, E.D. 1998, *AJ*, 116, 2746
- Telles, E. & Terlevich, R.J. 1995, *MNRAS* 275, 1
- Telles, E., & Maddox, S. 2000, *MNRAS*, 311, 307
- Temporin, S., Weinberg, R., Galaz, G. & Kerber, F. 2003, *ApJ*, 587, 660
- Temporin, S., Staveley-Smith, L. & Florian, C. 2005, *MNRAS*, 356, 343
- Tenorio-Tagle, G., Muñoz-Tuñón, C., Pérez, E. Silich, S. & Telles, E. 2006, *ApJ*, 643, 186
- Teplitz, H.I., Malkan, M.A., Steidel, C.C., McLean, I.S., Becklin, E.E., Figer, D.F., Gilbert, A.M., Graham, J.R., Larkin, J.E., Levenson, N.A. & Wilcox, M.K. 2000, *ApJ*, 542, 18
- Thilker, D.A., et al. 2005, *ApJ*, 619, L79
- Thilker, D.A. et al. 2007, *ApJS*, 173, 538
- Thuan, T.X. 1991, in *Massive stars in starbursts*, C. Leitherer, N.R. Walborn, T.M. Heckman & C.A. Norman (eds), Cambridge University Press, Cambridge, p.183
- Thuan, T.X., Lipovetski, V.A., Martin, J.-M. & Pustilnik, S.A. 1999, *A&ASS*, 139, 1
- Tissera, P.B., De Rossi, M.E., & Scannapieco, C. 2005, *MNRAS*, 364, L38
- Torres-Peimbert, S., Peimbert, M. & Fierro, J. 1989, *ApJ*, 345, 186

- Tremonti, C.A., et al. 2004, *ApJ*, 613, 898
- van Eymeren, J., Bomans, D.J., Weis, K. & Dettmar, R.-J. 2007, *A&A*, 474, 67
- van Eymeren, J., Marcelin, M., Koribalski, B.S., Dettmar, R.-J., Bomans, D.J., Gach, J.-L. & Balard, P. 2009, *A&A*, 505, 105
- van Eymeren, J., Koribalski, B.S., López-Sánchez, A.R., Dettmar, R.-J. & Bomans, D.J. 2010, submitted to *A&A*
- van Zee, L., Salzer, J.J. & Haynes, M.P. 1998, *ApJ*, 497, 1
- van Zee, L., Salzer, J.J. & Skillman, E.D. 2001, *AJ*, 122, 121
- van Zee, L. & Haynes, M.P. 2006, *ApJ*, 636, 214
- Vázquez, G.A. & Leitherer, C. 2005, *ApJ*, 621, 695
- Verma, A., Lutz, D., Sturm, E., Sternberg, A., Genzel, R. & Vacca, W. 2003, *A&A*, 403, 829
- Verdes-Montenegro, L., Yun, M.S., Williams, B.A., Huchtmeier, W.K., del Olmo, A. & Perea, J. 2001, *A&A*, 377, 812
- Verdes-Montenegro, L., del Olmo, A., Iglesias-Páramo, J. I., Perea, J., Vílchez, J.M., Yun, M.S. & Huchtmeier, W.K. 2002, *A&A*, 396, 815
- Verdes-Montenegro, L., del Olmo, A., Yun, M.S. & Perea, J. 2005, *A&A*, 430, 443
- Vila-Costas, M. B. & Edmunds, M. G. 1993, *MNRAS*, 259, 121
- Vila-Costas, M. B. & Edmunds, M. G. 1993, *MNRAS*, 265, 199
- Vílchez, J.M., & Esteban, C. 1996, *MNRAS*, 280, 720
- Walter, F., Brinks, E., de Blok, W.J.G., Bigiel, F., Kennicutt, R.C., Thornley, M.D. & Leroy, A. 2008, *AJ*, 136, 2563
- Warren, B.E., Jerjen, H. & Koribalski, B.S. 2004, *AJ*, 128, 1152
- Warren, B.E., Jerjen, H. & Koribalski, B.S. 2006, *AJ*, 131, 2056
- Warren, B.E., Jerjen, H. & Koribalski, B.S. 2007, *AJ*, 134, 1849
- Weilbacher, P.M., Duc, P.A. & Fritze-von Alvensleben, U. 2003, *A&A*, 397, 545
- Werk, J.K., Jangren, A. & Salzer, J.J. 2004, *ApJ* 617, 1004
- Westmeier, T., Braun, R. & Koribalski, B.S. 2010, *MNRAS*, submitted
- White, S.D.M. & Frenk, C.S. 1991, *ApJ*, 379, 52
- Wilcots, E. M., Lehman, C., & Miller, B. 1996, *AJ*, 111, 1575
- Wilson, C.D. 1995, *ApJ*, 448, 97
- Woosley S. E. & Weaver, T.A. 1995, *ApJS*, 101, 181
- Wyse, R.F.G. & Silk, J. 1985, *ApJ*, 296, L1
- Yin, S.Y., Liang, Y.C., Hammer, F., Brinchmann, J., Zhang, B., Deng, L.C. & Flores, H., 2007, *A&A*, 462, 535
- Yun, M.S., Ho, P.T.P. & Lo, K.Y. 1994, *Nature*, 372, 530
- Yun, M.S., Reddy, N.A. & Condon, J.J. 2001, *ApJ* 554, 803
- York, D.G. et al. 2000, *AJ*, 120, 1579
- Zaritsky, D., Kennicutt, R. C. Jr. & Huchra, J.P. 1994, *ApJ* 420, 87
- Zasov, A. V., Kniazev, A. Y., Pustilnik, S. A., Pramsky, A. G., Burenkov, A. N., Ugryumov, A. V. & Martin, J.-M. 2000, *A&AS*, 144, 429

Appendix A: Final summary of individual galaxies

In this Appendix we compile the main results found in our multiwavelength analysis of each individual system within our sample of Wolf-Rayet galaxies. In Papers I and II we described the optical/*NIR* broad-band and $H\alpha$ photometry, and the intermediate-resolution optical spectroscopy analysis, respectively, of 16 up to 20 galaxies studied in this work. The analysis of the additional 4 systems were presented in previous papers: NGC 1741 (member AC within the HCG 31 group) in López-Sánchez et al. (2004a), Mkn 1087 and their surrounding galaxies in López-Sánchez et al. (2004b), the luminous blue compact galaxy IRAS 08339+6517 in López-Sánchez, Esteban & García-Rojas (2006), and NGC 5253 in López-Sánchez et al. (2007). Paper III compiled the localization of the WR-rich star clusters within the galaxies and the analysis of their massive stellar populations. Paper IV compiles the global analysis of colours, and the physical properties and chemical abundances of the ionized gas. This paper, the last of the series, completes our analysis via a multi-wavelength analysis involving X-ray, *UV*, *FIR*, and radio data in both the 21-cm $H\text{I}$ line and the 1.4 GHz radio-continuum.

- **NGC 1741** hosts a very strong star-formation event, that is very probably a consequence of the merging of two spiral galaxies. NGC 1741 is the main member (AC) of the galaxy group HCG 31, and it is interacting with other galaxies in the group, including Mkn 1090 (HCG 31 G). We detect both the blue and red WR bumps in its brightest region, as well as the nebular $\text{He II } \lambda 4686$ line. HCG 31 AC seems to have a slightly higher N/O ratio. Some dwarf objects (members E, F1, F2 and H) are tidal dwarf galaxy (TDG) candidates. See López-Sánchez et al. (2004a) for details.
- **Mkn 1087** is a Luminous Compact Blue Galaxy (LCBG) in interaction with the nearby galaxy KPG 103a and with a dwarf surrounding galaxy (N companion). Deep optical images show long stellar tails connecting the main body of the galaxy with diffuse objects, some of them hosting star-formation activity, and several TDG candidates. Although WR features were previously reported by other authors, we do not detect any. See López-Sánchez et al. (2004b) for details.
- **Haro 15** probably is a medium-size Sc spiral in interaction with two nearby dwarf objects. Knot A shows a very high star-formation activity and WR features; its disturbed kinematics suggests that it is experiencing a minor merger with Haro 15. Knot B is an independent object because of its morphology, decoupled kinematics and chemical abundances.
- **Mkn 1199** is a system composed by a Sb-Sc spiral and a dwarf galaxy, both in clear interaction, as they may be at the first stages of a minor merger. The interaction has triggered the star formation activity in some areas of the main galaxy. Both the blue and red WR bumps are detected in the central region of Mkn 1199, that has solar metallicity. It seems that a substantial fraction of the $H\text{I}$ gas has been expelled to the intergalactic medium because of its low $M_{H\text{I}}/L_B$ ratio.
- **Mkn 5** is a BCDG with a strong star-forming burst located in the external part of the galaxy. The blue WR bump is detected in this starbursting region, that also possesses an important underlying old stellar component. We do not find any evidence of interaction, but the amount of $H\text{I}$ gas of the galaxy is very low compared with that expected for a BCDG. Furthermore, its dynamical mass is higher than that expected for a dwarf galaxy with similar properties. Both results suggest that Mkn 5 has lost its neutral gas in some moment of its past and still has a disturbed $H\text{I}$ kinematics.
- **IRAS 08208+2816** is a Luminous Infrared Galaxy (LIRG) showing two long tails with a very high star-formation activity. The kinematics of the ionized gas clearly indicate merger features and the existence of two long tidal tails with TDG candidates. The chemical abundances of the brightest knots also seem to be different. We detect both the blue and red WR bumps in the central region, that possesses a high N/O ratio.
- **IRAS 08339+6517** is a luminous infrared galaxy (LIRG) and a luminous blue compact galaxy (LCBG) in clear interaction with a nearby dwarf galaxy. The majority of the $H\text{I}$ gas of the system has been expelled to the intergalactic medium because of this interaction (Cannon et al. 2004). Our deep optical images reveal a faint stellar plume coincident with the $H\text{I}$ tail, and a disturbed morphology in the outskirts of the galaxy. A particular bright knot may be a TDG candidate of the remnant of a previous minor merger. We detect weak WR features in its central burst and quantified the star formation history of the galaxy (López-Sánchez, Esteban & García-Rojas 2006).
- **POX 4** is a morphology-disturbed low-metallicity BCDG showing strong star-forming bursts throughout all the galaxy. It seems to be in interaction with a nearby dwarf object that may have passed through the main body of the galaxy, being the origin of its ring-like morphology (Méndez & Esteban 1997) and kinematics. However, this objects may also be a TDG candidate originated by the interaction with a nearby and diffuse $H\text{I}$ cloud (López-Sánchez et al. 2010b). The $\text{He II } \lambda 4686$ emission line is clearly detected in its brightest region, as well as both the blue and the red WR bumps.
- **UM 420:** is a blue compact galaxy, but not a dwarf object, hosting intense star-formation activity. Besides it is located at 237 Mpc, we observe a central region and two kind of bright $H\alpha$ tails pointing towards different directions. Its kinematics is also perturbed. It has a very low metallicity for an object with its absolute optical/*NIR* luminosities, suggesting that it is a merging of two independent galaxies. We detect the $\text{He II } \lambda 4686$ emission line but no the blue WR bump in its brightest region. We found a probable N/O enrichment in the central region. Its colors and properties are somewhat contaminated by the spiral disk of the foreground galaxy UGC 1809, located at 97 Mpc.
- **SBS 0926+606:** is a galaxy pair with high star formation activity. Member A is a BCDG that shows a double nucleus; both its morphology and kinematics strongly suggests that it is a galaxy merger. We do not detect WR features in this galaxy but only the $\text{He II } \lambda 4686$ emission line. On the other hand, member B (another BCDG) hosts less star-formation activity, but it also shows hints of interactions, remarkably a long diffuse optical tail that shows a TDG candidate. SBS 0926+606 B has a huge emission in *UV*; the SFR derived from the *FUV* luminosity is more than one order of magnitude

- higher than the $H\alpha$ -based SFR. The system still hosts a huge amount of neutral gas.
- **SBS 0948+532**: is a very compact and blue object that hosts a very high star formation activity. Its M_{HII}/L_B ratio is very high in comparison with objects with similar properties. Although usually classified as BCDGs, its total B -luminosity indicates that it is not a dwarf object. We detect a faint optical tail mainly composed by old stars and with a slightly disturbed kinematics. We observe the nebular and broad He II $\lambda 4686$ lines.
 - **SBS 1054+365**: is a very nearby BCDG showing several star-forming regions embedded in a elliptical envelope composed by old stars. The kinematics of the ionized gas seems to be slightly disturbed. The main starbursting region shows the nebular and broad He II $\lambda 4686$ lines. Although we do not detect any clear interaction feature, its dynamical mass is too high in comparison with that observed in similar objects, and its metallicity is too high for a dwarf object. Further studies are needed to clarify its nature.
 - **SBS 1211+540**: is a very low-metallicity BCDG. It is composed by two bright $H\alpha$ regions surrounded by a relatively old stellar component. This BCDG seems to show a higher metallicity than expected for a dwarf object with its same properties. The detection of two faint optical tails and its disturbed kinematics suggest that this galaxy is experiencing its first stages of a merger process. Although reported previously, we do not detect any WR features.
 - **SBS 1319+579**: is a cometary-like BCDG showing two chains of intense star-forming regions over an underlying low-luminosity component dominated by old stars. We detect a very faint blue WR feature in the brightest knot. The analysis of the kinematics of the ionized gas strongly suggests that it is composed by two objects in interaction, that it is happening edge-on. Although there is plenty of neutral gas, the star formation is not very efficient, showing very low M_{HII}/L_B and M_*/L_B ratios in comparison with similar objects. Furthermore, it does not satisfy the Schmidt-Kennicutt law of star formation and the H I dynamics seem to be perturbed. We consider that the neutral gas has been expelled from the galaxy, but interferometric observations are needed to probe it.
 - **SBS 1415+437**: is a very low-metallicity BCDG that hosts a very strong star-forming region in which the nebular He II $\lambda 4686$ emission line is observed. It possesses an important old stellar population underlying the starburst. We do not detect any optical nearby companions and it does not show any evidence of interactions.
 - **III Zw 107**: is a BCDG showing two strong star-forming bursts embedded in an irregular envelope. A diffuse prominent tail is detected in this object. The broad He II $\lambda 4686$ line is found in the brightest knot, that shows a slightly higher N/O ratio. The neutral gas may have been expelled and/or dispersed. This galaxy is likely composed by two dwarf objects in process of interaction or merging.
 - **Tol 9**: is a BCG that belongs to the Klemola 13 galaxy group. It is a elliptical-shaped galaxy with intense nebular emission and chemically evolved. We have detected morphological and kinematical pattern that suggest interaction features. Our deep $H\alpha$ image reveals an extended filamentary structure with two main features that are located almost perpendicular to the main optical axis of the galaxy. The probable origin of this structure is a galactic wind. We detect both the blue and red WR bumps in the central region. The H I morphology and kinematics is quite intriguing, because this galaxy and two surrounding dwarf objects are embedded in the same H I cloud (LS08b,LS+10b).
 - **Tol 1457-262**: is a system composed by two bright objects and two dwarf galaxies, all showing nebular emission. We detect the nebular He II line in the brightest knots of the main object. The regions within this system show chemical differences and peculiar kinematics. The neutral gas content seems to be very high, and its dynamics highly perturbed, although detailed H I map should be required to quantify this. We consider that this system is a galaxy group in which its members are in interaction.
 - **Arp 252**: is a galaxy pair composed by two spiral galaxies, ESO 566-8 (A) and ESO 566-7 (B), in the first stages of a major merger. This object shows two long tails mainly composed by old stars but hosting some star-forming regions and TDG candidates. ESO 566-8 shows the broad and nebular He II $\lambda 4686$ emission line and the red WR bump. Its N/O is quite high for a galaxy with its oxygen abundance. ESO 566-8 has a strong star-formation and may host some kind of nuclear activity, because the *FIR*/radio relation is not satisfied in it. Although it was previously observed by other authors, we do not observe any WR feature in ESO 566-7.
 - **NGC 5253**: is a very nearby BCDG showing many peculiarities with respect to objects of similar characteristics. We detect clear broad WR features in the central regions, indicating the presence of both WNL and WCE stars. We confirmed the presence of a localized N enrichment in certain zones of the center of the galaxy and suggested a possible slight He overabundance in the same areas. We demonstrated that the enrichment pattern agrees with that expected for the pollution by the ejecta of WR stars. The amount of enriched material needed to produce the observed overabundance is consistent with the mass lost by the number of WR stars estimated in the starbursts (see López-Sánchez et al. 2007 for details). Although the kinematics of the ionized gas is somewhat peculiar, stellar kinematics seem to be consequence of rotation. Our optical study has not reveal any disturbed feature of a recent interaction process. However, its H I morphology is disturbed and its kinematics is quite intriguing, because it does not show any sign of regular rotation. The origin of this anomaly is most likely the disruption/accretion of a dwarf gas-rich companion or the interaction with another galaxy in the M 83 subgroup (Kobulnicky & Skillman 2008; López-Sánchez et al. 2008a, 2010a). Furthermore, its M_{HI}/L_B and M_{dust}/L_B ratios are very low and it does not satisfy the Schmidt-Kennicutt law of star formation.

